
UNIVERSITÀ
DEGLI STUDI
DI BRESCIA

DOTTORATO DI RICERCA IN INGEGNERIA MECCANICA E INDUSTRIALE

ING-IND/06 FLUIDODINAMICA

XXXIII CICLO

# Methodologies for the design and the accurate performance prediction of centrifugal pumps

Relatore:
Prof. Antonio Ghidoni

Dottoranda:
Alessia Fracassi

Anno Accademico 2019/2020

*"Lo studio e la ricerca della verità e della bellezza rappresentano una sfera di attività in cui è permesso di rimanere bambini per tutta la vita."*

— Albert Einstein

# Sintesi della tesi in italiano

Le pompe centrifughe sono ampiamente diffuse in campo industriale e sono caratterizzate da richieste molto diverse in termini di salto di pressione e portata da elaborare. Questo ampio range di applicazioni rende il design di una pompa complicato, per l'assenza di geometrie standard tra cui scegliere, ma allo stesso tempo di grande importanza e utilità. Di fatto, le prestazioni di una pompa sono influenzate da molti parametri geometrici, e ciò rende la fase di design molto complessa e dispendiosa. E' necessaria, quindi, una procedura di design cha sia solida, automatica, analizzi i vari parametri in modo esaustivo e che sia efficace nell'ottimizzazione delle performance. Inoltre, il campo di moto interno ad una pompa è spesso caratterizzato da alta instazionarietà e flusso distaccato. Ciò rende complessa anche la fase di valutazione delle performance tramite simulazioni CFD. In particolare, approcci tradizionali come le equazioni RANS, non sono adatti a predirre correttamente le prestazioni in condizioni di forte off-design in cui spesso una pompa è chiamata a lavorare. Approcci LES invece garantiscono accuratezza a discapito di tempi computazionali non compatibili con ambiti industriali.

Per affrontare la tematica in modo esaustivo la tesi è divisa in due parti:

- nella prima parte viene presentato un tool di ottimizzazione per il design automatico delle pale di girante e diffusore di una pompa centrifuga 2D, con l'obiettivo di massimizzarne il rendimento. La parametrizzazione delle pale comprende la linea mediana e la funzione spessore (solitamente non trattata) per un totale di 18 variabili di design. Infine, viene presentato uno studio di propagazione dell'incertezza, finora mai applicato all'ottimizzazione di pompe, per valutare la robustezza delle prestazioni del design ottimizzato;

- nella seconda parte viene presentato, validato ad applicato ad una pompa centrifuga un nuovo modello ibrido RANS-LES per la predizione accurata di flussi fortemente distaccati con tempi computazionali industrialmente accettabili.

La prima parte è suddivisa come segue:

- **Capitolo 1**: vengono illustrate le più comuni strategie di ottimizzazione in ambito turbomacchinistico. In particolare vengono descritte strategie di ottimizzazione con surrogato, il modello di surrogato kriging e gli algoritmi genetici, utilizzati nel tool di ottimizzazione presentato in questa tesi.

- **Capitolo 2**: viene presentata la strategia di ottimizzazione adottata e viene effettuato un confronto tra l'ottimizzazione dell'efficienza con genetico e con approccio *Efficient Global Optimizaion* (EGO). Viene mostrata la sua applicazione ad una pompa centrifuga 2D, di cui viene ottimizzata la forma delle pale di girante e diffusore.

- **Capitolo 3**: viene condotto uno studio di propagazione dell'incertezza per valutare la robustezza delle prestazioni del design originale e di quello ottimizzato. Come sorgenti di incertezza vengono considerate le incertezze sulle condizioni al contorno dovute al banco prova (velocità di rotazione e portata) e le incertezze sulle grandezze turbolente usate nelle simulazioni CFD. Lo studio conferma la validità dell'ottimizzazione deterministica.

La seconda parte affronta i seguenti capitoli:

- **Capitolo 4**: vengono illustrate le formulazioni DNS, LES e RANS, l'unione di questi due ultimi approcci nei modelli ibridi RANS-LES e i vantaggi di questi ultimi.

- **Capitolo 5**: viene esposta la formulazione del nuovo modello ibrido implementato, il Delayed X-LES (DX-LES), che unisce la formulazione X-LES con un ben definito modello di sottogriglia al vantaggio dei modelli *delayed* che superano il problema della riduzione degli sforzi modellati e garantiscono una migliore risoluzione del campo di moto a parete.

- **Capitolo 6**: il modello proposto viene valutato su tre casi test (il canale turbolento a Re = 2000, il *backward facing step* e il flusso attorno a un cilindro circolare a Re = 3900 e Re = 140 000. Tutti i casi confermano che il modello DX-LES evita la riduzione degli sforzi modellati e ha un comportamento a parete migliore rispetto al modello X-LES.

- **Capitolo 7**: il modello DX-LES viene applicato allo studio del flusso in una pompa centrifuga in condizioni di design e off-design. Esso mostra un buon accordo con i risultati LES, a differenza dei modelli RANS che in condizioni di off-design non sono in grado di predirre il

complesso fenomeno di vortici che si instaura nella pompa, con uno sforzo computazionale moderato.

# Abstract

Centrifugal pumps are widely used in many industrial fields, such as agriculture, automotive, chemical, power generation and bio-engineering and are characterized by considerable differences in the requested pressure ratio and flow rate. Thus, the design and the accurate performance prediction of a centrifugal pump is a challenging issue. In facts, the pump performance is affected by a lot of free geometric parameters and consequently the design phase can be very complex and time-consuming. Secondly, pumps often show highly detached flows, which make the traditional CFD approach, based on RANS equations, unsuitable to properly simulate their flow field. The thesis is divided in two parts: in the first part, an advanced optimization technique to design impeller and diffuser blades, in order to maximize the efficiency of the pump, is presented; in the second part, a new implemented hybrid RANS-LES model for the accurate prediction of highly detached flows is presented, validated and finally applied to a centrifugal pump.

# Contents

# Introduction

Centrifugal pumps are widely used in many industrial fields, such as agriculture, automotive, chemical, power generation and bio-engineering. The design of a centrifugal pump can be very complex and time-consuming, because centrifugal pumps are characterized by considerable differences in the requested pressure ratio and flow rate, and because the pump performance is affected by a lot of free geometric parameters. For these reasons, a reliable and automatic procedure is necessary for an efficient design strategy.

Moreover, pumps often show highly detached flows. In particular, this phenomenon occurs as a result of two different circumstances: (*i*) the absence of a design process aimed at maximizing the pump efficiency and, thus, at minimizing flow detachment; (*ii*) the working condition far from the design point considered in the optimization mentioned in point *i*, that can lead up to rotating stall. Anyway, in these situations, the traditional CFD approach, based on RANS equations, are unsuitable to properly simulate their flow field. In fact, RANS simulation is not accurate in cases where the flow is dominated by internal instabilities, as the flow field in a pump at strongly off design conditions. Large Eddy Simulation (LES) approach, instead, is accurate in most applications, but is rarely used in industry, due to the high computational cost. There is therefore a need of an accurate but cost-effective alternative.

To tackle the matter of the design and the accurate prediction of centrifugal pump flow field in a comprehensive way the thesis is divided in two parts. The first part is devoted to present an advanced optimization technique to design impeller and diffuser blades in order to maximize the efficiency of the pump. It involves surrogate-based optimization algorithms coupled with CFD simulation. It allows a fast and effective design procedure avoiding numerical or trial and error approaches, that can't guarantee the better pump performance. In literature, previous works have faced the shape optimization of a centrifugal pump [1, 2, 3, 4, 5, 6, 7, 8, 9]. They focus mainly on a single component, *i.e.* impeller or diffuser or volute, without considering the effect of the coupling on the optimization, the geometric parameterization

is always quite simple, and the thickness distribution is not considered. In this thesis, an existing optimization approach is applied to a full centrifugal pump with impeller and vaned diffuser and both the camber line and the thickness function are parameterized.

Furthermore, geometries provided by deterministic optimization approaches could show discrepancies between predicted and real performance, as they can be very sensitive to uncertainties related to operating conditions or the geometry. Thus, the robustness assessment of the baseline and the optimal design through an uncertainty propagation study is presented. In fact, uncertainties are present in most engineering applications such as turbomachines, but an uncertainty quantification study has never been applied to assess the suitability of optimization for pump automated design. In this perspective a robust design optimization would be of interest if the level of variability is judged too large. As a consequence, in this work an assessment of how uncertainties on the pump test influence the variability of pump performance is addressed, particularly in relation to the improvement of the performance obtained with the optimization. This study confirmed the validity of the deterministic optimization, without the necessity to conduct a robust optimization.

The second part of this thesis provides a possible solution to the prediction of pump performance in off design conditions. During the last twenty years, several simulation approaches have been tested to predict the pump flow fields in presence of large flow separations. Different studies showed as RANS methods performs well only nearby the design condition, while at off design conditions this methodology is unsuitable due to the highly unsteady nature of the flow. Barrio et.al. [10, 11] applied 3D URANS with $k-\epsilon$ turbulence model to study the flow in the near-tongue region of a centrifugal pump, showing significant differences with experimental data at very low and high flow rates, with respect to the nominal one. Braun [12] showed as the $k-\omega$ SST turbulence model fails to predict the rotating stall in a pump-turbine. Byskov [13] in 2003 stated the necessity of an eddy resolving techniques to correctly predict the internal flow field of a centrifugal pump at off design conditions. Wang and Wang [14] compared the predicted fluctuations of the static pressure rise in a low specific speed centrifugal pump with LES and RNG $k-\epsilon$ turbulence model. The results are comparable at design condition, while at off design conditions LES predicts the unsteady characteristics of the flow more accurately. Kato et. al. [15] used LES to study the inner flow of a high specific speed mixed-flow pump at low flow rate conditions, where stall takes place. LES shows a good agreement with measurements. Posa et. al. [16, 17] applied LES approach to study strong secondary flows at reduced loads with good agreement with PIV measurements. However,

LES methods are not often manageable due to the high computational cost. Hybrid models can be an effective alternative. Feng et. al. [18] applied the detached-eddy simulation to investigate the flow in a centrifugal pump, showing good agreement with the experiments on both velocity and turbulent fields in predicting rotating vortex and back flow at reduced rate. Lucius and Brenner [19, 20] used the scale adaptive simulation to predict the stall phenomenon in a centrifugal pump.

The aim of the second part of this thesis is to implement a hybrid RANS-LES method, that combines the SGS formulation of the X-LES model, rewritten on the $k-\omega$ SST turbulent model of Menter, with the advantages of a delayed-DES version, which overcomes the modelled stress depletion and allows to better solve the near wall region. This new model, denoted as delayed X-LES (DX-LES), is implemented in the open-source software OpenFOAM v.1812 and is tested on three different test-cases, commonly used to assess turbulent models: the turbulent channel flow at $\mathrm{Re}_\tau = 2\,000$, the backward facing step at $\mathrm{Re} = 28\,000$ and the circular cylinder at $\mathrm{Re} = 3\,900$ and $\mathrm{Re} = 140\,000$. Finally, DX-LES has been applied to the computation of the flow through a centrifugal pump impeller [21] and results have been compared with experimental results and LES and RANS simulations from the literature. The DX-LES model shows a good agreement with the LES results both in design and off design condition, where RANS methods are not able to predict the complex turbulent flow inside the pump, and the required computational effort is moderate.

# Part I

# Automated design of centrifugal pumps

# Chapter 1

# Deterministic shape optimization overview

In this Chapter, the most common strategies for the optimization of turbomachines and pump performance are presented and, in this context, the optimization methods used in this thesis are introduced.

## 1.1 Design techniques

Many free geometric parameters can influence the performance of a centrifugal pump, making the design phase very complex and time-consuming. Traditional approaches are based on the experience of the engineer and requires a continuous refinement of geometry components. An experimental approach, where prototypes and previous models are modified with a trial-and-error method, is a first strategy. Zhao et al. [22] modified a pipeline pump through a manual adjustment. Shiyang et al. [23] proposed an investigation of the effect of the thickness distribution on the performances of a centrifugal pump testing different geometries. The study highlights a dependency of the efficiency from the blade thickness, but the method cannot provide a correlation between the two variables. In general, this design process can be too expensive and the result depends on the ability of the user. Empirical formula can be applied to improve the procedure. Wenguang [24] proposed an optimization of the required net positive suction head (NPHSr) using an experimental database for the impeller diameter, the radial equilibrium equation and the 2D vortex element method for the blade. Kim et al. [25] applied the velocity diagrams for a first design of the impeller blade and the Stepanoff theory for the base volute. Then, the effects of the cross-section distribution for the volute have been investigated on random geometries and

an improvement of the impeller performance is achieved through a response surface method (RSM) analysis. Anyway, the empirical correlations cannot address exhaustively the design of a complex turbomachinary and allow only the study of some spotted design, while a better solution can be ignored.

In the last years the exponential growth of the available computational resources has paved the way to the automation of conventional design processes by coupling CFD solvers and optimization algorithms. The idea is to parameterize the geometry through some design variables and modify this parameters according to an optimization algorithm able to find the best combination in order to maximize or minimize some objectives. This methodology results in a systematic design process, which allows to reduce time and costs and ensures the best solution in the studied geometry range. In 2004 Burguburu et al. [26] optimized transonic compressor blades with a gradient based optimization strategy. The algorithm achieved a raising of efficiency but it can remain trapped in a local optimum. To avoid this risk a global optimization technique is usually preferred. Oyama et al. [27] improved the NASA 67-blade rotor by using a genetic algorithm. The procedure requires huge computational resources. For this reason genetic algorithms are often coupled with a surrogate model that approximates the correlation between the geometries and the performances and drastically reduces the computational effort.

A surrogate-based optimization is employed by Pei et al. [28] to enhance the efficiency of an impeller modifying the meridian channel. Wang et al. [29] and Siddique et al. [30] optimized respectively a 2D and a 3D impeller blade with a fixed thickness function. De Donno et al. [31] improved the efficiency of a full centrifugal pump (impeller and vaned diffuser) applying a genetic algorithm on a kriging surrogate. Derekhshan et al. [2] optimized the performances of a 3D impeller with the artificial bee colony algorithm. Zhao et al. [32] proposed a 2D optimization of a centrifugal pump with splitter-blades parametrerizing the pressure side of the main blades. These works are mostly based on a simple parameterization of a single component, without considering the effect of their coupling, and they do not include the parametrization of the thickness distribution. In this thesis a surrogate-based optimization of a 2D pump with impeller and vaned diffuser is presented and the performance improvement is achieved by modifying both the camber line and the thickness distribution of the blades.

The organization of this chapter is as follows. Sections 1.2 and 1.3 present an insight respectively into the optimization algorithms and the surrogate models mainly applied in literature for the optimization of the pump performance, while Section 1.4 is focused on the generation of dataset.

## 1.2 Optimization algorithms

An optimization problem, with a single objective and generally constrained can be expressed as follows:

$$\begin{aligned} \text{minimize:} \quad & f(\boldsymbol{x}), \\ \text{subject to:} \quad & g_L \leq g(\boldsymbol{x}) \leq g_U, \\ & h(\boldsymbol{x}) = h_t, \\ & \boldsymbol{x}_L \leq \boldsymbol{x} \leq \boldsymbol{x}_U, \end{aligned} \tag{1.1}$$

where $\boldsymbol{x}$ is an N-dimensional vector and represents the design variables or input variables. The N-dimensional vectors $\boldsymbol{x}_L$ and $\boldsymbol{x}_U$ are the lower and upper bounds on $\boldsymbol{x}$ and define the design space. The scalar function $f(\boldsymbol{x})$ is the objective function and the goal of the optimization is to minimize (or maximize) it while satisfying the nonlinear inequality constraint on $g(\boldsymbol{x})$ and the nonlinear equality constraint on $h(\boldsymbol{x})$, if they are present. The objective functions can be more than one, such as the constraints.

Different algorithms have been developed to solve an optimization problem. They can be classified in two main categories: the gradient-based methods and the stochastic methods. The gradient-based algorithms need an initial design, from which the searching direction is defined by the local gradient of the objective functions with respect to the design variables. The derivative can be calculated with a finite difference approximation, and in this case the time cost is proportional to the number of design variables. In alternative, the adjoint method analyses the influence of the input variables on the flow field, which in turn affects the objective functions. Thus, the calculation of the gradients is independent from the number of design variables, but it requires complex adjoint equations. Adjoint method has been employed in different works [33, 34]. Even if the gradient-based methods are efficient, they are suitable for a local optimization, being the result depending on the initial design and failing to ensure to find the global optimum.

In contrast, the stochastic methods search the optimum globally in the defined design space. Often these algorithms are inspired on some natural process or event. For example the Particle Swarm Optimization simulates the animal behaviour of moving swarm like the bird flocking: it starts from a population of design and it moves them in the search-space based on a velocity that is a measure of the design fitness. This method is efficient but it risks to trap into a local optimum. The Simulated Annealing refers to the process of heating and slow cooling of metals. The algorithm decides between accepting a new design or keeping the current one according to a probability depending on the design fitness. It suits very complex optimization problems

to achieve an approximate global optimum in limited time. A third method commonly used in turbomachinery are the genetic algorithms (GA), applied in this thesis.

GAs are based on the mechanism of natural selection and Darwin's survival of the fittest concept. A starting population of a fixed number of individuals evolves by selection, crossover and mutation until a final individual. The process is shown in Fig. 1.1. Each individual is characterized by a vector of the settled input variable, that represents a chromosome. Selection is based on an individual's fitness, evaluated on the related objective function value. The best individuals are more probably selected to be copied in the new generation. Starting from these selected individuals other two mechanisms allow to evolve from the previous population to the offspring. First the crossover obtains new individuals exchanging portions of chromosomes of two parents. After, the mutation alters randomly part of the chromosomes of some individuals. This avoids the algorithm to remain trapped in a local optimum. Finally, if the offspring do not include the best individual of the parents' population, this best individual replaces one of the new generation randomly. These steps are iterated until all the individuals of subsequent populations converge to an optimum. The user has to select the crossover and mutation rate, which determine the number of respective operations that take place. If the crossover rate is set too low or too high the search becomes very time consuming because the convergence is too slow or the search-space too broad, respectively. If the mutation rate is too low the process can lead to a local optimum, while for too high values the inheritance of the parents is lost. The GAs are simple and robust optimization tools. Genetic algorithms are widely used for the design of turbines [35, 36], compressors [37, 38, 39] and pumps [32, 28, 29, 31], and have been used also in this thesis.

## 1.3 Surrogate models

As seen in the previous paragraph, the global optimization algorithms require the evaluation of a huge quantity of design. Even if the computational capacity has grown rapidly in the last years, the computational cost of running that number of CFD simulations is impractical. Replace the expansive simulations by computing surrogate models is a widespread strategy to overcame this issue. Surrogate models, also called metamodels, approximate the truth model (CFD simulation) providing a more affordable function. They exploit different principles, but the most common kind of surrogate is the data fit type, that is based on the interpolation or regression of a dataset obtained running the truth model.

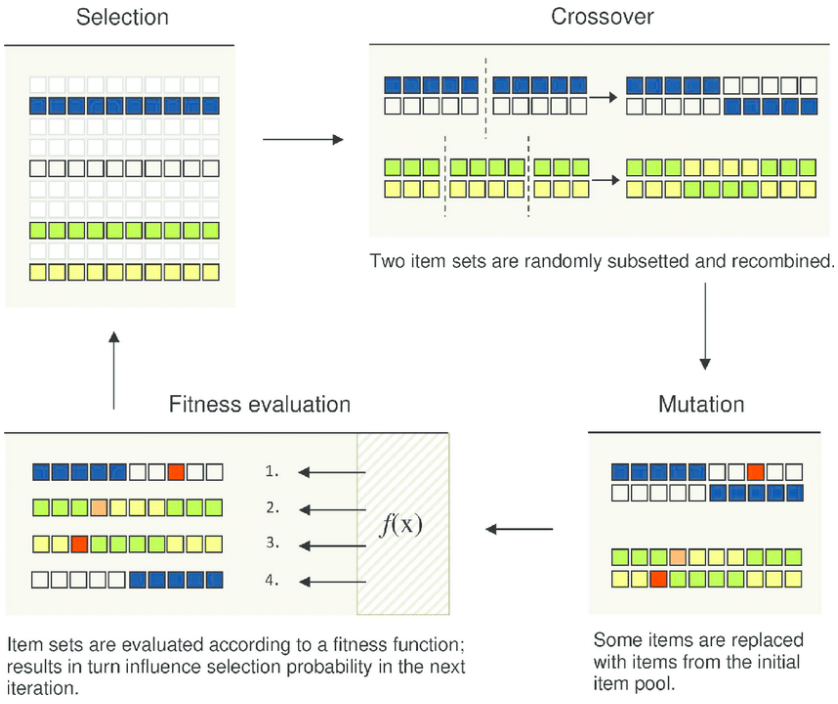


Figure 1.1: Flow chart of a single iteration for a genetic algorithm [40]

A surrogate-based optimization (SBO) problem can be formulated as follows. In general, it decomposes the main problem in a series of subproblems solved in a constrained region $\Delta^k$. However, the objective function and the constraints can be managed in different ways. A merit function can be defined to combine the original objectives and the constraints:

$$\begin{aligned} \text{minimize:} \quad & \hat{\Phi}^k(\boldsymbol{x}), \\ \text{subject to:} \quad & \| \boldsymbol{x} - \boldsymbol{x}_c^k \| \leq \Delta^k. \end{aligned} \tag{1.2}$$

Otherwise, the approximate objective function is directly optimized and the constraints are explicit:

$$\begin{aligned} \text{minimize:} \quad & \hat{f}^k(\boldsymbol{x}), \\ \text{subject to:} \quad & g_L \leq \hat{g}^k(\boldsymbol{x}) \leq g_U, \\ & \hat{h}^k(\boldsymbol{x}) = h_t, \\ & \| \boldsymbol{x} - \boldsymbol{x}_c^k \| \leq \Delta^k. \end{aligned} \tag{1.3}$$

Different surrogate models are used in optimization problems. The Polynomial response surface method (RSM) uses low-order polynomial approxi-

mation. The second order is commonly used and it can be written as follows:

$$y = \beta_0 + \sum_{i=1}^{N} \beta_i x_i + \sum_{i=1}^{N} \beta_{ii} x_i^2 + \sum \sum_{i!=j}^{N} \beta_{ij} x_i x_j, \tag{1.4}$$

where $y$ is the predicted function and $\beta$ are the regression coefficients.

The artificial neural network (ANN) model is inspired by the biological neurons process in the animal brain. The ANN is based on neurons or nodes arranged in layers. An input layer and an output layer are connected by one or more hidden layers (see Fig. 1.2). The input layer receives the input variables and transfers their value to the first hidden layer. Then this value are weighted, combined and processed through a transfer function. For the $i^{th}$ node of the first layer these operations are summarized in the following function:

$$a_1(i) = FT_i\Big(\sum_{j=1}^{N}(W_1(i,j)x_j) + b_1(i)\Big), \tag{1.5}$$

where $FT$ is the transfer function and $W$ the connection weight. The results of the first hidden layer are the inputs for the second one, and the process continues layer by layer, until the output.

The kriging (KRG) model uses a Gaussian process to approximate the function:

$$y = \sum_{i=1}^{m} \beta_i F_i(\boldsymbol{x}) + Z(\boldsymbol{x}). \tag{1.6}$$

The predicted function is computed as the sum of trend basis functions (often polynomials) that fit the dataset and a stochastic function $Z(x)$ with mean zero that fixes the function to interpolate the experiments. $F(\boldsymbol{x})$ is the vector of the basis functions and $\boldsymbol{\beta}$ is the vector of the generalized least squares estimates of the basis function coefficients. $Z(\boldsymbol{x})$ is a realization of a stochastic process with mean zero, a process variance $\sigma$ and a spatial correlation function:

$$cov[Z(x_i), Z(x_j)] = \sigma^2 \mathrm{R}(x_i, x_j), \tag{1.7}$$

where R is the correlation.

There is no one metamodel superior to the others in absolute. Some studies show as a model performs better than an other one for a particular application. Jin et al. [42] illustrate as the success of a surrogate model depends on multiple factors: on the non-linearity of the problem and the dimension of the dataset. In this study, they show that the RSM is to prefer for low-order non-linear problems and small scale dataset, the KRG

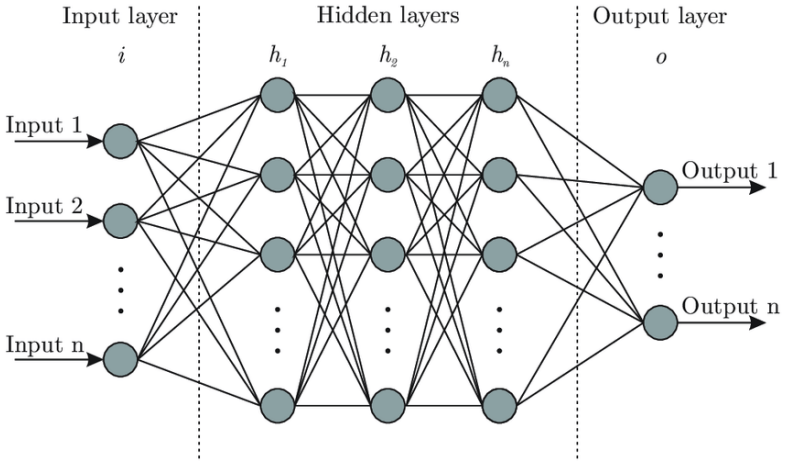


Figure 1.2: Artificial neural network scheme [41]

for low-order non-linear problems and high scale dataset, while the ANN for high-order non-linear problems. Bellary et al. [43] and Samad et al. [44] applied multiple surrogates on the same dataset to ensure the fidelity of the surrogate. The question is also what better means for a surrogate model in an optimization process: of course the accuracy is the main parameter, but the challenge is to provide the highest accuracy using the smallest possible dataset. De Donno et al. [31] presented a comparison between the kriging and the artificial neural network for a shape optimization of an impeller pump. In this work the surrogate model approximates the dependency of the efficiency and the total pressure head on 16 parameters defining the geometry. From this analysis the error between the real and the predicted functions is lower with the KRG, at least until 300 training points in the dataset. Being the application of this thesis very similar, the KRG model is used in the following.

## 1.4 Filling dataset

The metamodel construction needs a dataset meaningful of the whole design space. The Design of Experiments (DoE) refers to the systematic procedure that aims to test and discover an unknown effect of introducing a change in the preconditions. The challenge of a DoE is to provide the maximum information with the minimum number of design experiments (also called training points).

One of the most common algorithm to generate a DoE is the Latin Hypercube Sampling (LHS) [45]. It is suitable for computer experiments, which are mainly characterized by system errors rather then random errors, since

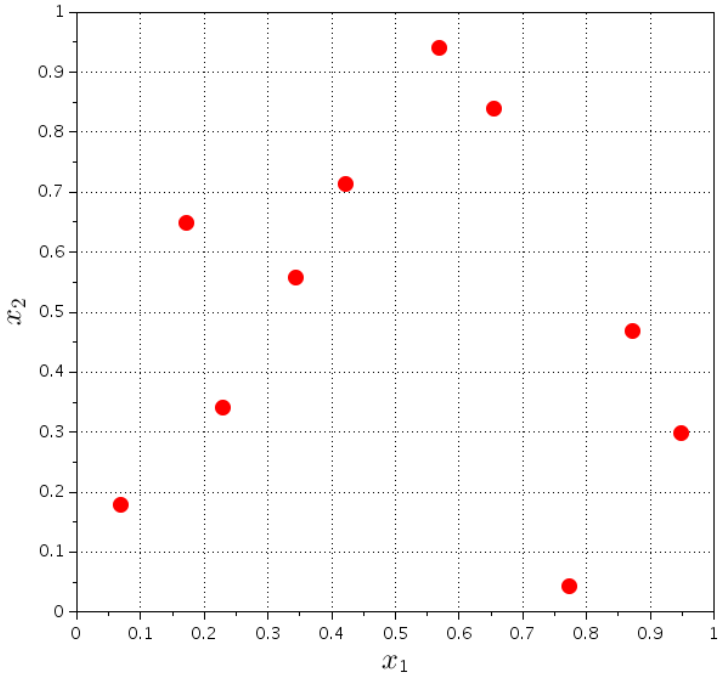


Figure 1.3: Example of the Latin Hypercube Sampling method in a 2D design space for a dataset with 10 training points

the algorithm tends to fill the design space instead of focus on the boundary. Requiring $n$ training points, the LHS algorithm divides the range of each design variables in $n$ intervals and ensures that each variable is represented in each interval. An example is shown in Fig. 1.3.

There is not a fixed rule to determine the minimum number of the training points to use. It depends on the surrogate model, on the non-linearity of the functions and on the desired accuracy. For example a second order polynomial model requires to set $k = \frac{(N+1)(N+2)}{2}$ coefficients, with $N$ the number of input variables. Kaufman:1996 et al. [46] suggested to use from $1.5k$ to $4.5k$ training points to obtain reasonable second order results, while Jin et al. [42] proposed a dataset with $10N$ training points.

# Chapter 2

# Surrogate based optimization tool

The objective of this Chapter is to present a framework for a single objective optimization to enhance the performance of a centrifugal pump. A surrogate-based optimization algorithm based on the kriging model is shown and two different strategies to find the optimum are compared.

## 2.1 The ERCOFTAC centrifugal pump

The tool is applied to the ERCOFTAC pump, taken as reference design to optimize. The ERCOFTAC pump is the simplified model of a centrifugal pump presented by Combès [47] in 1999. The geometry of the pump is depicted in Fig. 2.1, while Tab. 2.1 reports the main geometric parameters and operative conditions. Experimental [48] and numerical [49] data are available in literature.

The optimization objective is represented by the hydraulic efficiency

$$\eta = Q\Delta p_t / W, \tag{2.1}$$

while an inequality constraint is applied to the total pressure rise coefficient

$$\psi = 2\Delta p_t / \rho U_2^2, \tag{2.2}$$

where $Q$ $[m^3/s]$ is the volumetric flow rate, $\Delta p_t$ $[Pa]$ the total pressure rise across the pump, $W$ $[W]$ the power at the impeller, $\rho$ $[kg/m^3]$ the density, and $U_2$ $[m/s]$ the peripheral velocity at the impeller outlet. In particular, the optimization algorithm maximizes $\eta$, while keeping $\psi$ constrained to the considered operating conditions. Usually, the pressure head is constrained, to

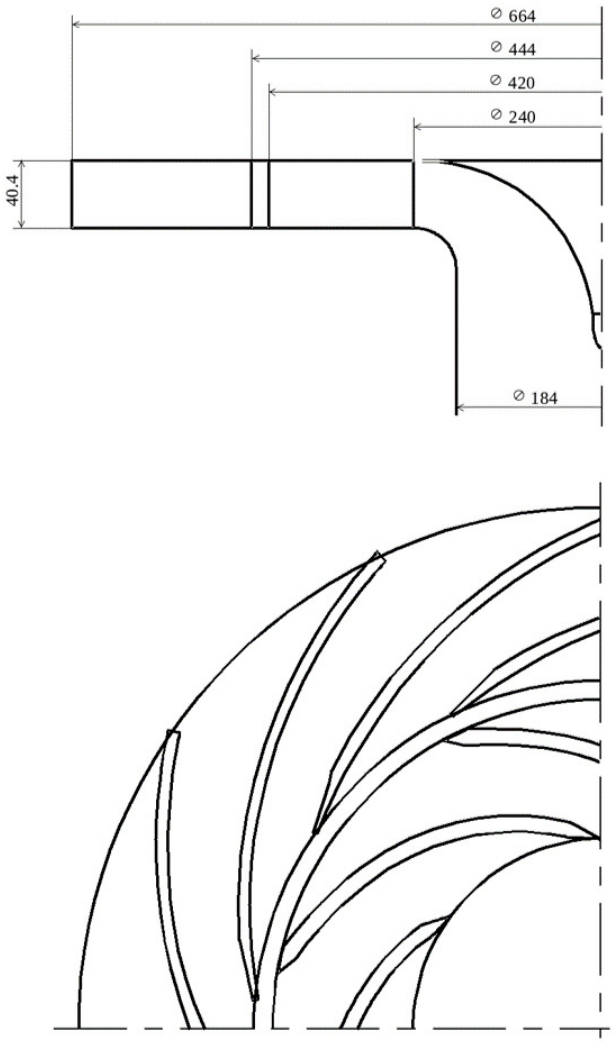


Figure 2.1: ERCOFTAC centrifugal pump geometry

Table 2.1: Main geometric parameters and operative condition of the ER-COFTAC centrifugal pump

| | | |
|---|---|---|
| **Impeller** | | |
| inlet blade diameter | $D_1$ | = 240 mm |
| outlet diameter | $D_2$ | = 420 mm |
| blade span | $b$ | = 40 mm |
| number of blades | $z_i$ | = 7 |
| **Diffuser** | | |
| inlet vane diameter | $D_3$ | = 444 mm |
| outlet vane diameter | $D_4$ | = 664 mm |
| vane span | $b$ | = 40 mm |
| number of vanes | $z_d$ | = 12 |
| **Operative conditions** | | |
| rotational speed | $n$ | = 2000 rpm |
| flow rate coefficient | $\phi$ | = 0.048 |
| total pressure rise coefficient | $\psi$ | = 0.65 |
| Reynolds number | $Re$ | = 6.5 $10^5$ |
| **Inlet air reference conditions** | | |
| temperature | $T$ | = 298 K |
| air density | $\rho$ | = 1.2 kg/m$^3$ |

keep fixed the working condition for the baseline and optimized geometry. A tolerance is added to the equality constraint to not discard potential optimum and to make the process more robust. A preliminary numerical investigation has shown that the maximum efficiency in this problem is reached for the upper limit of the constraint. For this reason, the constraint for $\psi$ is set between $-5\%$ and $0\%$. The design variables that affect $\psi$ and $\eta$ are the parameters that define the pump geometry.

In the following, Sec. 2.2 is devoted to the description of the geometric parameterization algorithm, while Sec. 2.3 describes the CFD solver. Sections 2.4 and 2.5 present the deterministic optimization framework and the respective results.

## 2.2 Geometric parameterization

The geometric parameterization is the first and fundamental step of the optimization process. The main requirements of a parameterization are:

1. minimize the number of design variable,
2. widen the design space, to include also non-conventional design,
3. prevent the occurrence of unfeasible geometries.

In this work, the shape of the impeller and diffuser blades and the outlet diameter of the diffuser are parameterized. A total of 18 design variables (DV) are used. They are reported in Tab. 2.2. The letter $c$ is the chord length, the subscripts $i$ and $d$ refer to the impeller and the diffuser, respectively, and $LE$ and $TE$ to leading and trailing edge.

The generation of the design from the design variables is often controlled by the use of Non-Uniform Rational Basis Spline (NURBS) [50], that offer flexibility and precision. A subclass of NURBS are the Bézier curves, which are parametric curves or surfaces based on the Bernstein polynomials. A $n$th-degree Bézier curve is defined as

$$\mathbf{C}(\mathbf{u}) = \sum_{i=0}^{n} B_{i,n}(u)\mathbf{P_i}\ , \quad u \in [0,1], \tag{2.3}$$

where $\mathbf{C}(\mathbf{u})$ is the Bézier curve of independent variable $u$, $\mathbf{P_i}$ are the control points and $B_{i,n}(u)$ are the $n$th-degree Bernstein polynomials given by

$$B_{i,n}(u) = \frac{n!}{i!(n-i)!} u^i (1-u)^{n-i}. \tag{2.4}$$

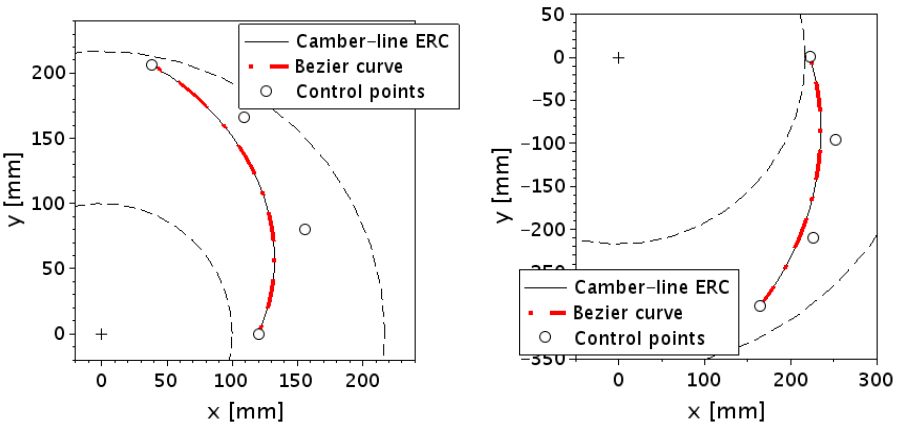


(a) Impeller (b) Vaned diffuser

Figure 2.2: Control points of the parameterized ERCOFTAC camber-lines

The blade geometry of the impeller and the vaned diffuser is defined by the sum of the camber-line and the thickness distribution, which are both generated through Bézier curves. The choice of the design variables is driven by the criteria listed above but also by the need to reproduce the baseline with the same parameterization in a sufficiently accurate way. Figures 2.2 and 2.3 show the layout of the camber lines and thickness function design variables and how the ERCOFTAC camber line can be reproduced.

The main dimensions of the pump are fixed, *i.e.* inlet and outlet diameters of the impeller and the vaned diffuser. As a consequence, also the vaneless radial gap between impeller and diffuser is fixed. However, the diameter of the diffuser blades trailing edge can be reduced. In facts, an analysis of the effect of the absence of this parameter in the design space is carried out in Sec. 2.5, where the need of the design variable $D_4$ is stated.

The paramaterization is managed with the software Scilab [51].

### 2.2.1 Camber-line

The camber-lines of the impeller and the diffuser are described through a Bézier curve. To define the most suitable number of control points associated with the order of the Bézier curve, curves of different orders ($3^{rd}, 4^{th}$ and $5^{th}$) are considered. The objectives are i) to minimize the number of input variables, ii) find a parameterization able to reproduce faithfully the camber-line of the ERCOFTAC pump blades (impeller and diffuser) and iii) include some common blades profiles used to manufacture pump blades, *i.e.* the NACA 6-series, the double circular arc (DCA) and the C4 airfoil. The

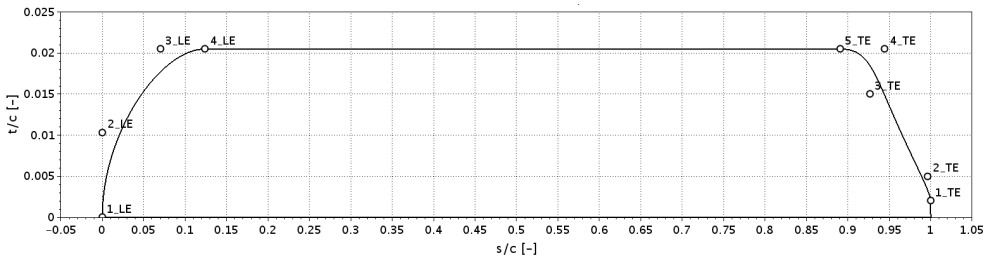


(a) *Impeller*

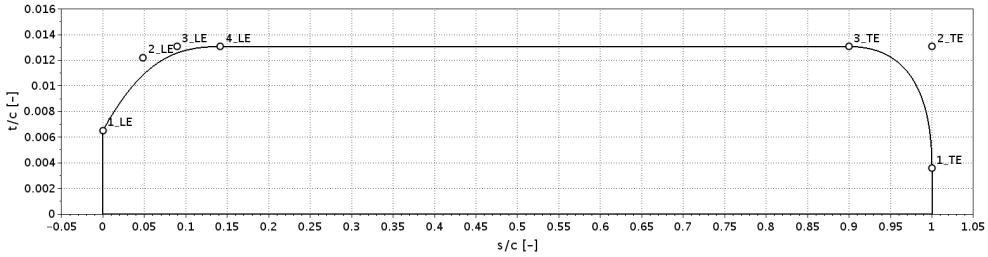


(b) *Vaned diffuser*

Figure 2.3: Control points for the thickness function parametrization

Table 2.2: List of the design variables with the description, the baseline value, and the minimum/maximum value during the optimization

| Variable | Description | Baseline | Min value | Max value |
|---|---|---|---|---|
| $\gamma_{imp}$ | Stagger angle of the impeller [°] | -111.5 | 120 | -90 |
| $\beta_1$ | Inlet angle of the impeller [°] | -66.0 | -76 | -56 |
| $\beta_2$ | Outlet angle of the impeller [°] | -70.9 | -75 | -60 |
| $\gamma_{dif}$ | Stagger angle of the diffuser [°] | 101.4 | 90 | 105 |
| $\alpha_3$ | Inlet angle of the diffuser [°] | 72.8 | 65 | 85 |
| $\alpha_4$ | Outlet angle of the diffuser [°] | 67.8 | 60 | 75 |
| $x_{t\_LEi}$ | Position along the chord of point of maximum thickness at leading edge of impeller [-] | 0.1330 | 0.1 | 0.3 |
| $dr_{LE,i}$ | Difference between $x_{t\_LEi}$ and the radius at leading edge of the impeller [-] | 0.06323 | 0.010 | 0.064 |
| $k_{t,i}$ | Curvature at the point of maximum thickness at leading edge of the impeller [-] | -3.2591 | -3.26 | -1.00 |
| $x_{t\_TE,i}$ | Position along the chord of the point of maximum thickness at trailing edge of the impeller [-] | 0.9146 | 0.80 | 0.95 |
| $x_{3\_TE,i}$ | Position along the chord of the third control point at trailing edge of the impeller [-] | 0.9323 | 0.92 | 1.00 |
| $\alpha_{TE,i}$ | Slope at trailing edge of the impeller | -0.9556 | -1.2 | -0.5 |
| $x_{t\_LE,d}$ | Position along the chord of the point of maximum thickness at leading edge of the diffuser [-] | 0.1424 | 0.1 | 0.3 |
| $dr_{LE,d}$ | Difference between $x_{t\_LEd}$ and the radius at leading edge of the diffuser [-] | 0.01008 | 0.005 | 0.100 |
| $y_{1\_LE,d}$ | Thickness at leading edge of the diffuser [-] | 4.0129 | 2.0 | 5.0 |
| $\alpha_{LE,d}$ | Slope at leading edge of the diffuser [-] | 0.004266 | 0.003 | 0.075 |
| $x_{t\_TE,d}$ | Position along the chord of the point of maximum thickness at trailing edge of the diffuser [-] | 0.999 | 0.700 | 0.999 |
| $D_4$ | Outlet diameter of the diffuser blade [mm] | 664.0 | 554.0 | 664.0 |

Table 2.3: Approximation error [%] for different reference camber-lines and order of the Bezier curves

| | $3^{rd}$ | $4^{th}$ | $5^{th}$ |
|---|---|---|---|
| Impeller ERC | 0.518 | 0.156 | 0.0650 |
| Vaned diffuser ERC | 0.210 | 0.0558 | 0.0457 |
| NACA 63 | 0.853 | 0.266 | 0.105 |
| NACA 64 | 0.440 | 0.0946 | 0.0640 |
| NACA 65 | 0.127 | 0.0131 | 0.000993 |
| DCA | 0.182 | 0.0474 | 0.0104 |
| C4 | 0.0115 | 0.00108 | 1.71E-05 |

camber-line is built leaving two degrees of freedom for each control point inside the curve. The approximation error has been measured by evaluating the distance (root mean square distance normalized with the chord length) between the real and parameterized profiles, and is reported in Tab. 2.3 for each considered reference camber-line.

A fourth-order Bézier curve has been chosen for the parameterization, but with a number of degrees of freedom (DoF) equal to a third-order curve. The DoF reduction is obtained by fixing the distance (equal to the corresponding distance for the ERCOFTAC geometry) of the two internal control points from the leading and trailing edge, while inlet and outlet angles of the blade are free to change. This choice allows for a better approximation of the ERCOFTAC camber-lines and higher geometrical flexibility than a standard third-order curve, even if sharing the same number of variables. The approximation error is comparable to a third-order curve and is at least $< 0.9\%$ for every reference profile. In addition to inlet and outlet angles, the parameterization algorithm can also vary the stagger angles.

### 2.2.2 Thickness function

The thickness function is parameterized in a different way for the impeller and the diffuser. The objective is to find a parameterization able to reproduce the thickness distributions of the ERCOFTAC blades. For this reason the number of control points differs from the impeller to the diffuser. In both cases, the leading (LE) and the trailing edge (TE) are described through a Bézier curve, and they are joined with a constant thickness line (see Fig. 2.3). The parameterization of the leading and the trailing edge is based on the Bézier-PARSEC method [52], which exploits PARSEC variables, i.e. leading edge radius, curvature, upper and lower crest location, etc., as parameters for the Bézier curve.

Both the leading edge are parameterized with third degree polynomials. The diffuser has a positive thickness at the starting of the LE to fit the ERCFTAC profile. The TE of the impeller is a polynomial with degree forth, while in the diffuser TE only three control points are used to allow a rounded profile. The control points are set according to Eqs. 2.5, 2.6, 2.7 and 2.8. The hat symbol defines a fixed value. In particular, $\hat{y}_t$ is the maximum thickness of the blade, which is set equal to the thickness of the ERCOFTAC blade to compare different profiles and to avoid the computation of too thin blades.

$$\begin{aligned} s_{1\_LE} &= 0 & t_{1\_LE} &= 0 \\ s_{2\_LE} &= 0 & t_{2\_LE} &= 3k_{t,i}\frac{dr_{LE,i}^2}{2} + \hat{y}_{t,i} \\ s_{3\_LE} &= x_{t\_LE,i} - dr_{LE,i} & t_{3\_LE} &= \hat{y}_{t,i} \\ s_{4\_LE} &= x_{t\_LE,i} & t_{4\_LE} &= \hat{y}_{t,i} \end{aligned} \tag{2.5}$$

Equation 2.5: Impeller leading edge

$$\begin{aligned} s_{1\_TE} &= c_i & t_{1\_TE} &= \hat{y}_{TE,i} \\ s_{2\_TE} &= c_i + \frac{\hat{y}_{2\_TE,i} - \hat{y}_{TE,i}}{\tan(\alpha_{TE,i})} & t_{2\_TE} &= \hat{y}_{2\_TE,i} \\ s_{3\_TE} &= x_{3\_TE,i} & t_{3\_TE} &= \hat{y}_{3\_TE,i} \\ s_{4\_TE} &= x_{t\_TE,i} + dr_{LE,i} & t_{4\_TE} &= \hat{y}_{t,i} \\ s_{5\_TE} &= x_{t\_TE,i} & t_{5\_TE} &= \hat{y}_{t,i} \end{aligned} \tag{2.6}$$

Equation 2.6: Impeller trailing edge

### 2.2.3 Range of the input variables

The baseline values of the DVs shown in Tab. 2.2 correspond to the ERCOFTAC geometry that is considered as the baseline configuration. The values are computed optimizing the position of the control points to minimize the approximation error (root mean square distance between corresponding points of the real and parameterized geometry). Figure 2.4 shows how the ERCOFTAC thickness function of the impeller and diffuser are reproduced.

$$
\begin{aligned}
s_{1\_LE} &= 0 & t_{1\_LE} &= y_{1\_LE,d} \\
s_{2\_LE} &= x_{2\_\hat{LE},d} & t_{2\_LE} &= \frac{\hat{x}_{2\_LE,d}}{\tan(\alpha_{LE,d})} + y_{1\_LE,d} \\
s_{3\_LE} &= x_{t\_LE,d} - dr_{LE,d} & t_{3\_LE} &= \hat{y}_{t,d} \\
s_{4\_LE} &= x_{t\_LE,d} & t_{4\_LE} &= \hat{y}_{t,d}
\end{aligned}
\tag{2.7}
$$

Equation 2.7: Vaned diffuser leading edge

$$
\begin{aligned}
s_{1\_TE} &= c_d & t_{1\_TE} &= \hat{y}_{1\_TE,d} \\
s_{2\_TE} &= c_d & t_{2\_TE} &= \hat{y}_{t,d} \\
s_{3\_TE} &= x_{t\_TE,d} & t_{3\_TE} &= \hat{y}_{t,d}
\end{aligned}
\tag{2.8}
$$

Equation 2.8: Vaned diffuser trailing edge

Two constraints are satisfied for the definition of the input variables range (see Tab. 2.2): *i*) baseline geometry is included, and *ii*) only feasible geometries can be generated. A design is considered feasible if the thickness is non-negative and is greater than a threshold value at the diffuser leading edge.

The impeller inlet angle range has the baseline value as the midpoint, while the range for the impeller outlet angle has been chosen according to the literature. The range of the diffuser inlet angle is computed from the impeller outlet angle, applying velocity diagrams, while the range for diffuser outlet angle is calculated starting from the volute outlet velocity with the free-vortex theory. The volute outlet velocity is estimated with the Stepanoff theory [53].

## 2.3 CFD set-up and baseline design analysis

In this section, the set-up adopted for all simulations is presented, both in terms of mesh and CFD solver. Moreover, the effect of the parameterization algorithm on the pump flow field is investigated, comparing the performance of the actual and modelled geometry predicted by the CFD analysis.

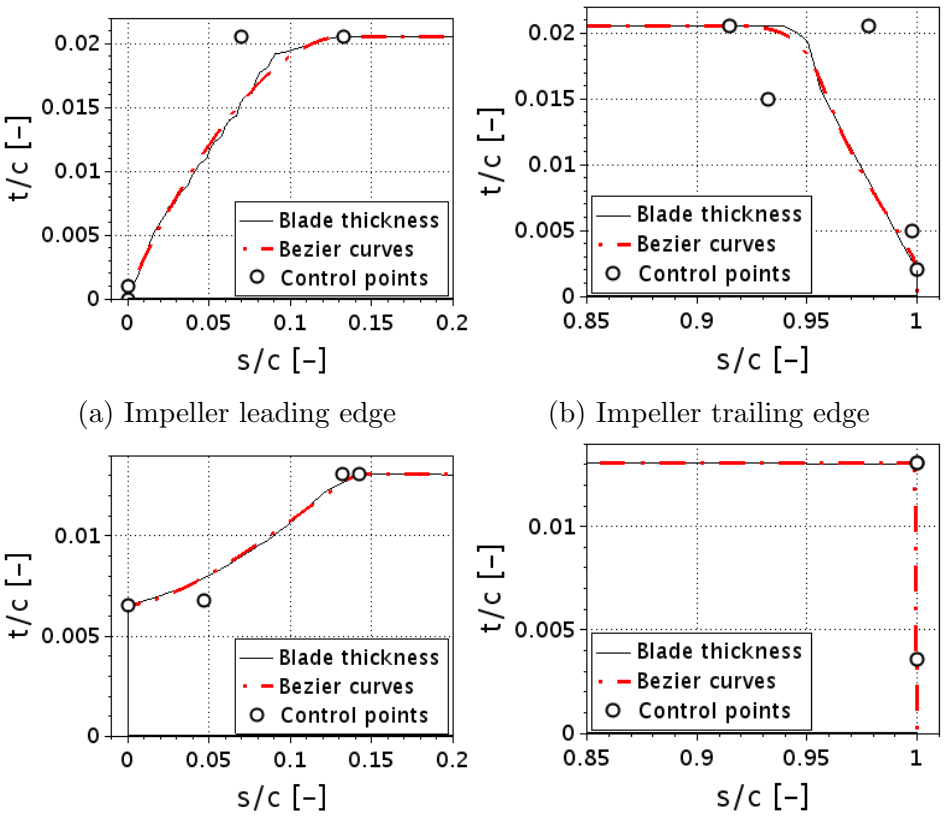


(a) Impeller leading edge

(b) Impeller trailing edge

(c) Vaned diffuser leading edge

(d) Vaned diffuser trailing edge

Figure 2.4: Control points of the parameterized ERCOFTAC thickness function

Table 2.4: Boundary conditions for the numerical simulation

| **Boundary Conditions** | |
|---|---|
| inlet velocity $V_1$ | 11.64 m/s |
| inlet turbulent kinetic energy $k_1$ | 0.496 $m^2/s^2$ |
| inlet specific dissipation rate $\omega_1$ | 4962.2 $s^{-1}$ |
| outlet static pressure $p_4$ | 0 Pa (average on area) |
| relative velocity at walls | 0 m/s |
| turbulent kinetic energy at walls | 0 $m^2/s^2$ |

### 2.3.1 CFD set-up

The 2D hybrid meshes of the geometries created during the optimization process are generated with an in-house mesh generator [54]. Only one blade passage is considered for the impeller and diffuser. The size of the elements adjacent to the solid walls is equal to a non-dimensional distance $y^+ \approx 1$, to compute the boundary layer accurately up to the wall.

The open-source CFD software OpenFOAM [55] is used to compute the flow field through the pump. The incompressible Reynolds Averaged Navier-Stokes (RANS) equations coupled with $k$-$\omega$ SST turbulence model [56] are solved. The choice of the turbulence model is dictated by the SST capability to predict correctly flow-fields characterized by the adverse pressure gradient and detachment, *i.e.* the expected flow-field of a pump.

Based on previous studies [57, 58], which demonstrate the capability of 2D simulations to predict reasonably well the ERCOFTAC pump flow-field, 2D simulations have also been chosen for this work to reduce the computational effort.

The operating conditions are summarized in Tab. 2.1. At the domain inlet the velocity $V_1$ (computed from $\phi$), the turbulence intensity $Tu_1 = 4\%$ and the specific dissipation rate $\omega_1$ are prescribed, while at the outflow a static pressure is set. Adiabatic wall boundary conditions are applied to all blades. Details of the boundary conditions are listed in Tab. 2.4.

A steady-state formulation with the Multiple Reference Frame (MRF) approach is used; the impeller and diffuser are fixed with respect to each other, but the momentum equation for the impeller domain is solved in the rotating reference frame. The impeller outflow and the diffuser inflow are coupled with a mixing-plane interface. This approach, unlike the frozen rotor interface, avoids the convection through the pump of non-physical wakes created by the impeller blades. The use of the mixing plane interface allows reducing the computational cost significantly, as the simulation of a single blade passage for both impeller and vaned diffuser regardless of their blades number

Table 2.5: Predicted efficiency, $\eta$, and total pressure coefficient, $\psi$, of the 3D ERCOFTAC pump with different approaches (RANS+Mixing plane, RANS+Frozen rotor, URANS). $Err_\eta$ and $Err_\psi$ represent the deviation in the prediction of $\eta$ and $\psi$ for Mixing plane and Frozen rotor approaches with respect to the URANS values that are taken as reference

| CFD approach | $\psi$ [-] | $\eta$ [%] | $Err_\eta$ | $Err_\psi$ |
|---|---|---|---|---|
| URANS | 0.748 | 87.3 | - | - |
| RANS + Frozen rotor | 0.730 | 84.4 | $-2.41\%$ | $-3.32\%$ |
| RANS + Mixing plane | 0.764 | 87.0 | $+2.13\%$ | $-0.34\%$ |

is performed. Predicted $\psi$ and $\eta$ with mixing plane and frozen rotor interfaces have been compared with a URANS simulation for the 3D ERCOFTAC pump. Table 2.5 summarizes the results and shows a good agreement between the mixing-plane and unsteady simulations, both in terms of efficiency and total pressure coefficient.

The second-order upwind discretization scheme is applied to the divergence of the velocity, while the first-order upwind scheme is applied to the turbulent quantities. The Laplacian terms are evaluated using a linear second-order bounded central scheme, while a central differencing method approximates the gradient term.

### 2.3.2 Performance of the original and parameterized ERCOFTAC pump

The effect of the geometric parameterization in the prediction of the ERCOFTAC pump performance is investigated. Specifically, both the original and modelled geometries are simulated and the predicted $\eta$ and $\psi$ are compared. A mesh convergence study has been performed for both geometries, using three grids with the number of elements ranging from 25000 to 55000. Finer meshes have been obtained refining uniformly the coarser mesh. The grid convergence study (see Fig. 2.5) shows some differences in the predicted results. As suggested by the convergence study, the grid with 37000 elements ensures a good compromise between computing time and accuracy of the results, and, therefore, it is chosen for the optimization.

The discrepancy in the predicted performance of the two geometries can be explained with an in-depth comparison. In particular, Fig. 2.6 shows the velocity and pressure contours for the real (left column) and the parameterized (right column) geometries. The main differences are gathered near the trailing edge of the impeller blade and the leading edge of the diffuser

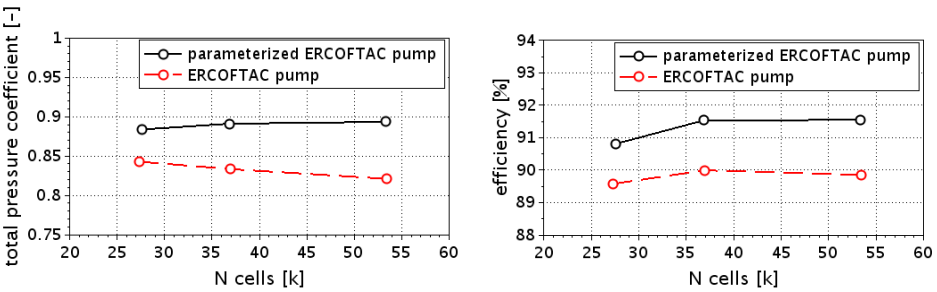


Figure 2.5: Grid convergence study for the original and modelled ERCOFTAC pump geometry

blade, where the parameterization smooths the edges of the original geometry. In fact, near the trailing edge of the parameterized impeller, the wake is smaller. Moreover, at the leading edge of the real diffuser, flow separation can be observed, which is almost absent in the parameterized geometry. These differences in the flow field of the parameterized geometry entail a reduction of the losses, and, as a consequence, higher efficiency and total pressure coefficient.

## 2.4 Deterministic optimization strategy

Global optimization methods require a high number of evaluations, especially with a large number of input variables. To reduce the computational cost, a Surrogate Based Optimization (SBO) [59] is employed. The values of the cost function are analytically computed using the surrogate model at a negligible cost with respect to a CFD simulation (truth model). A kriging model is used. The initial DoE is generated through an LHS method, and each design is evaluated performing a CFD simulation.

In this work, two different strategies to compute the optimum of the surrogates are compared: the Single Objective Genetic Algorithm (SOGA) and the Efficient Global Optimization (EGO) [60]. The methods available in the software Dakota [61] have been used.

The optimization strategy is summarized in Fig. 2.7 and the details of the applied methods are illustrated in Chapter 1.

### 2.4.1 SOGA

Different types of surrogate, available in literature, can be used with SOGA. Here the Gaussian process or kriging (KRG) model [62] is adopted for the following reasons: *i*) it is suitable for both linear and non-linear objective

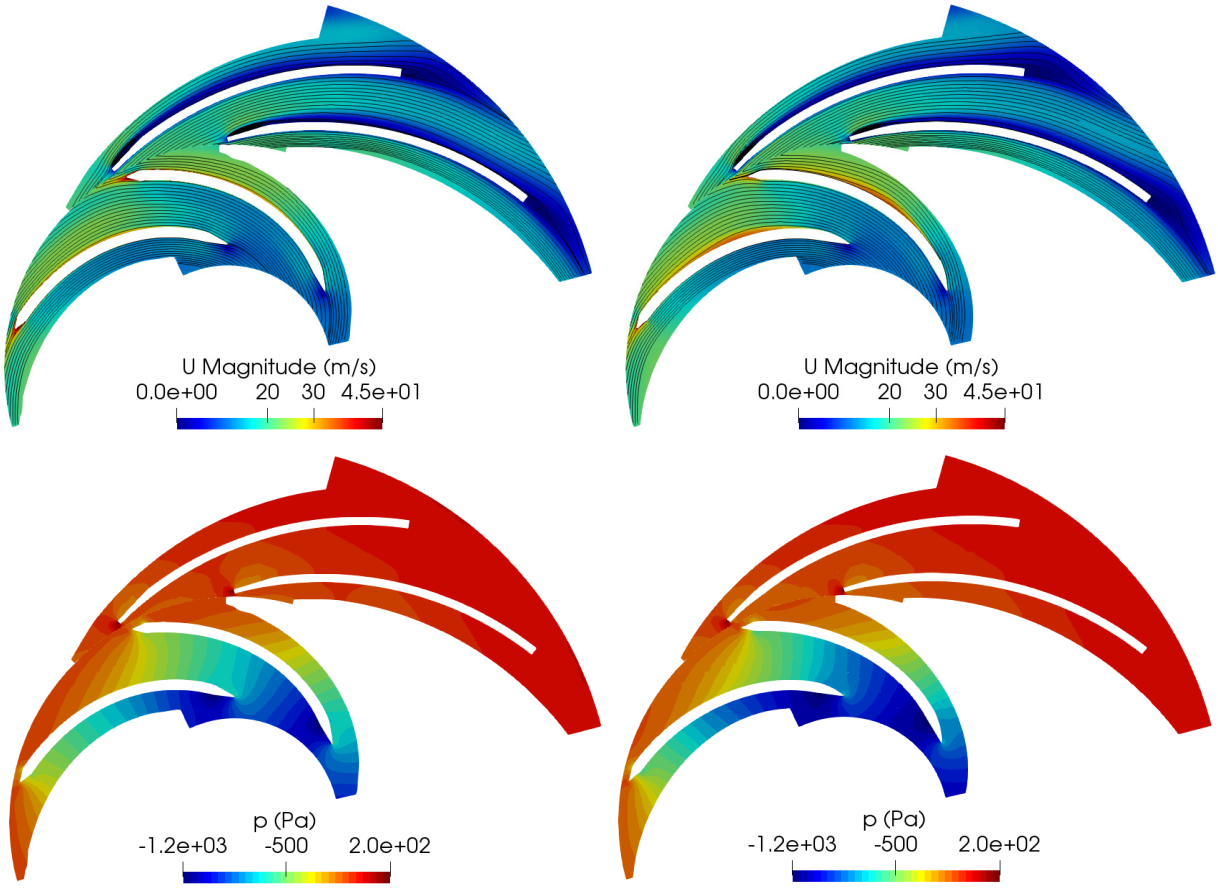


(a) Real geometry (b) Parametrized geometry

Figure 2.6: Comparison between the velocity (top) and pressure (bottom) contours for the real (left column) and parametrized (right column) ERCOFTAC pump geometry

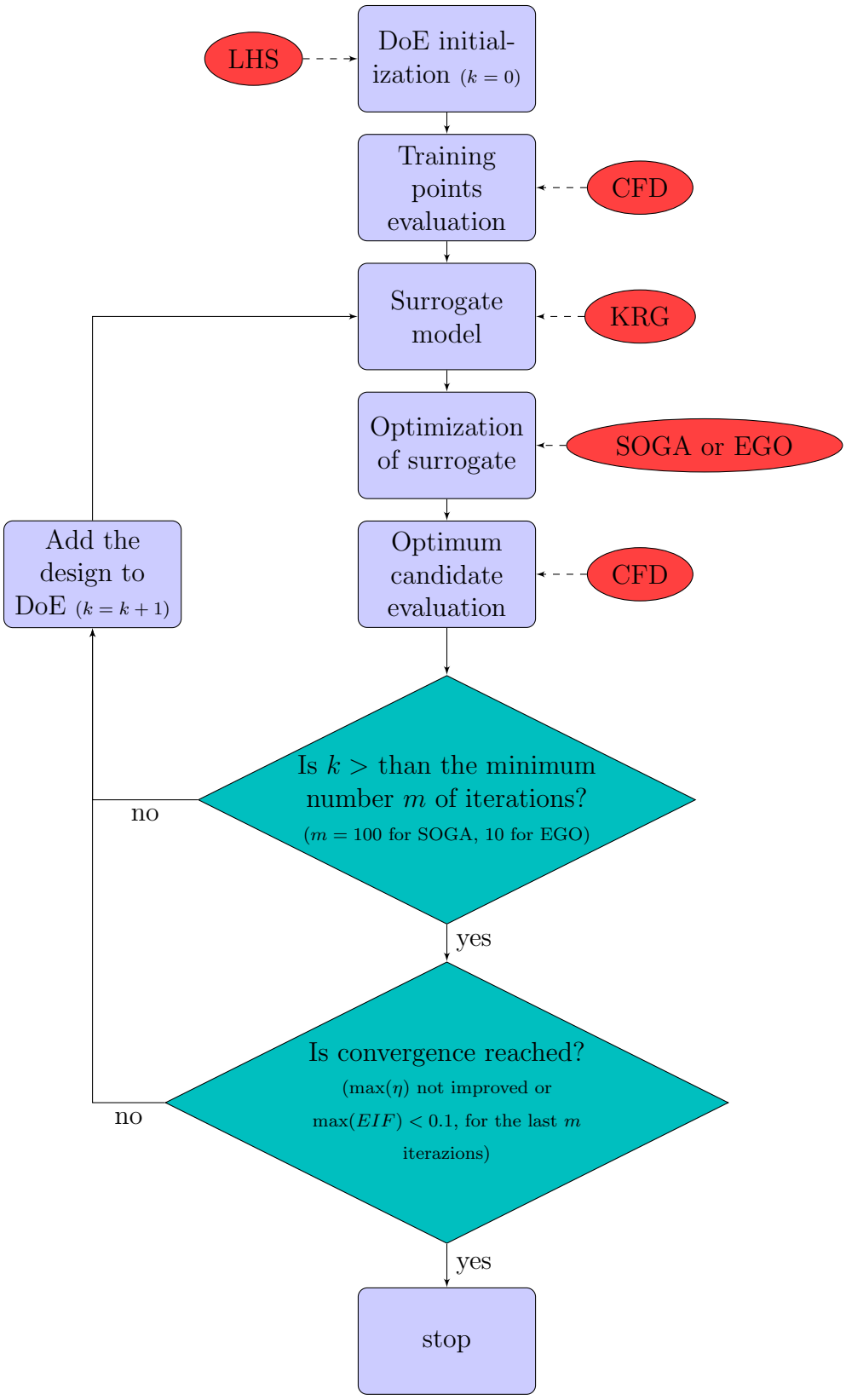


Figure 2.7: Optimization strategy

function, *ii*) it reduces the number of model parameters if the data-set is small [63], and *iii*) it is often adopted for turbomachinery optimization.

A genetic algorithm (GA) is chosen as a global optimization algorithm for its flexibility and robustness. It has a low probability to remain trapped in a local minimum, and it is often used in turbomachinery shape optimization. The crossover rate used in this work is 0.8 and the mutation rate is 0.1. The convergence is assumed to be reached when the objective function is not improved after 100 loops of the strategy depicted in Fig. 2.7.

### 2.4.2 EGO

EGO algorithm exploits KRG to evaluate the error in the prediction of the objective function. In particular, EGO exploits this feature to search the optimum through the maximization of the Expected Improvement Function (EIF), defined as follows:

$$E[I(\underline{x})] = (\hat{y} - f_{max})\Phi(\frac{\hat{y} - f_{max}}{s}) + s\,\omega(\frac{\hat{y} - f_{max}}{s}),$$

where $\hat{y}$ is the predicted function and $s$ its standard error, $\Phi(\cdot)$ and $\omega(\cdot)$ are the standard normal density and distribution function, respectively.

The EGO algorithm allows combining exploitation and exploration, so that both zones of design space with good solutions and with lack of information are tested. This feature could be advantageous in search of the global optimum with respect to SBO with SOGA. In fact, the latter approach focuses the research only in the zone of good solution, depending on the initial distribution of the data set, and can lead to a local optimum. This limitation can be particularly dangerous when the accuracy of the response surface can be limited for the considerable number of design variables. On the other hand, the EGO algorithm finds the optimum of a more complex function.

For this algorithm, a different convergence criterion has been selected. In particular, the convergence is assumed to be reached when the maximum EIF value is lower than 0.1 throughout ten iterations.

## 2.5 Results

Initially, the outlet diameter of the diffuser blade $D_4$ is not considered in the parameterization, and the effects on the optimized geometry are investigated. In the second part of the discussion, the result of the optimization process performed including $D_4$ is presented.

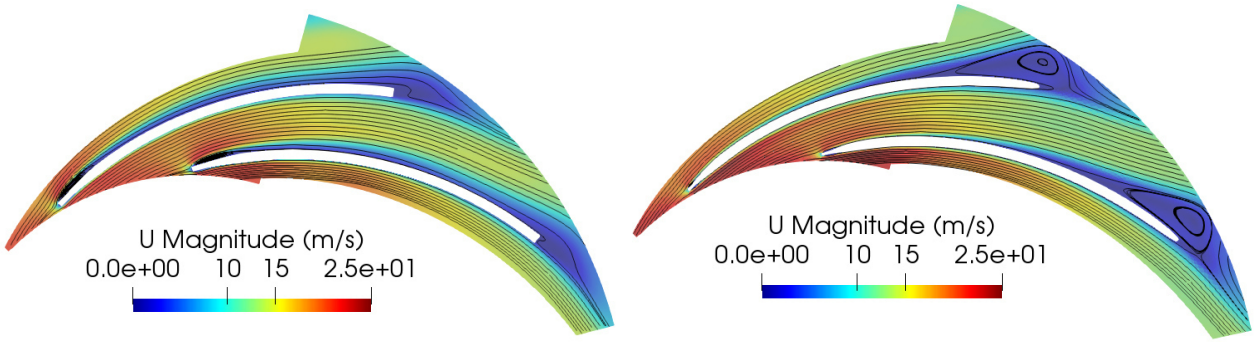


Figure 2.8: Velocity contour and streamlines in the diffuser for the baseline (left) and a random design of the DoE (right)

### 2.5.1 Influence of the diffuser outlet diameter

In this section a study is carried out with a fixed outlet diameter of the diffuser blade. The DoE is created with 340 design (20 times the number of design variables) obtained with a LHS technique. Each design is analyzed with a CFD simulation and it is excluded from the DoE if the CFD calculation does not converge. Surprisingly, it has been seen that all the design in the DoE presented a vortex along the suction side of the diffuser blade: at the leading edge like the baseline or at the trailing edge (see Fig. 2.8).

Generally, the vanishing of the vortex is expected with the increasing of the efficiency, but this is not the correct interpretation. For a better understanding, the phenomenon is deepened in the following.

The efficiency of the whole machine (see Eq. 2.1) can be splitted as

$$\eta = \frac{\Delta p_{t,imp}}{W} - \left|\frac{\Delta p_{t,diff}}{W}\right| = \eta_{imp} - \left|\frac{\Delta p_{t,diff}}{W}\right|. \tag{2.9}$$

To maximize the efficiency it is possible to increase the efficiency of the impeller or to decrease the total pressure losses in the diffuser. The impeller efficiency is maximized by minimizing the power at the impeller $W$. The decreasing of the diffuser losses, as the $\Delta p_t$ is fixed with a tolerance, is accompanied by an unloading of the impeller blade: a decreasing of $W$ is followed by a proportional decreasing of $\Delta p_{t,imp}$ and a decreasing of the total pressure losses in the diffuser ($-\Delta p_{t,dif}$). In Fig. 2.9 the first possibility is represented by design (that respect the constraint) on a vertical line in the graph, while the second one, by design, which are horizontally aligned.

However, improving the performance of the diffuser the vortex is not removed. The issue concerns the role of the diffuser. It has the task of conveying the flow to the outlet of the machine and transforming the kinetic

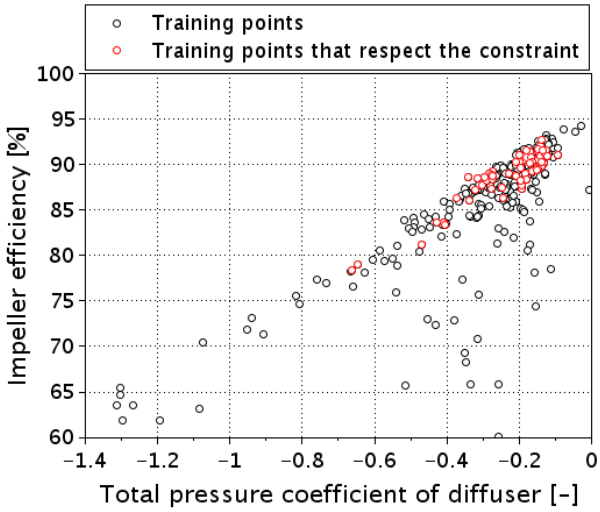


Figure 2.9: Correlation of $\Delta p_{t,diff}$ and $\eta_{imp}$ for the design in the DoE

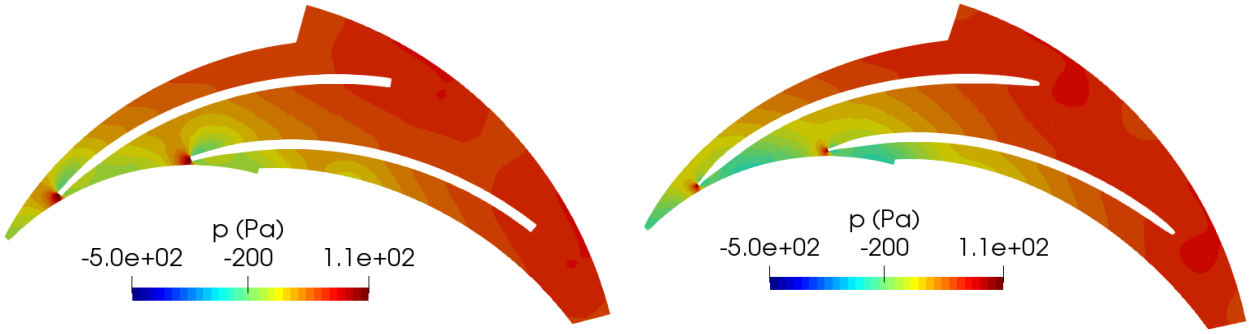


Figure 2.10: Static pressure contour in the diffuser for the baseline (left) and a random design of the DoE (right)

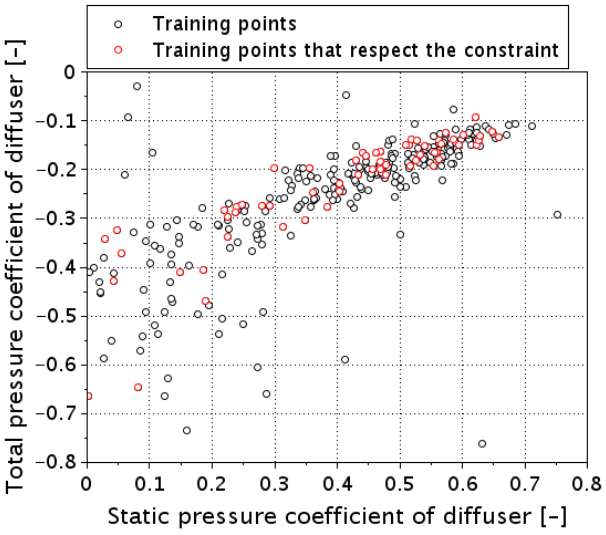


Figure 2.11: Correlation of $\Delta p_{diff}$ and $\Delta p_{t,diff}$ for the design in the DoE

energy of the fluid at the impeller discharge into static pressure. The diffuser pressure field for the baseline and a second design of the DoE is shown in Figure 2.10. The relation between the static and the total pressure rise in the diffuser for the design that respect the total pressure rise constraint is almost linear (see Fig. 2.11), and can be expressed as follows:

$$\Delta p_{t,diff} = \Delta p_{diff} + \frac{1}{2}\rho U_4^2 - \frac{1}{2}\rho U_3^2, \tag{2.10}$$

where $U_3$ and $U_4$ are the absolute values of the velocity at the inlet and the outlet of the diffuser. As shown in Fig. 2.11, decreasing the losses in the diffuser leads to an increase of the static pressure at the outflow and, thus, to an increase of adverse pressure gradient, that promotes the detachment of the flow near the blade trailing edge.

Therefore, during the optimization, design with large detachments in the rear part of the diffuser blade and a high efficiency can be found. However, design without the presence of vortex are preferable, even if only for the well-known limitations of RANS approaches in computing detached flows. This results in the necessity to penalize the efficiency of these configurations during the optimization process.

From this analysis, it is clear as the design space used in the DoE leads to an excessive diffusion process in the diffuser. In the following, to overcome the oversizing of the diffuser the diffuser outlet can be moved according to the range of the diffuser outlet diameter $D_4$ (see Tab. 2.2).

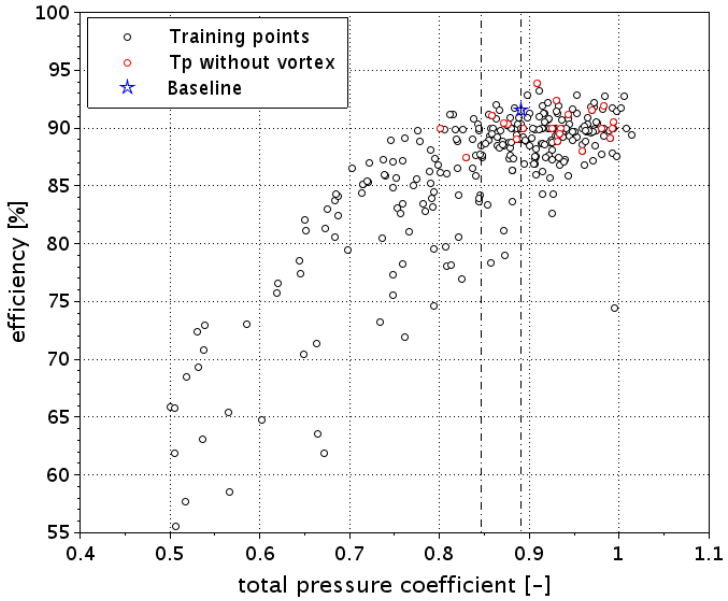


Figure 2.12: Design of Experiment: $\Delta p_t$ and $\eta$

### 2.5.2 Deterministic optimization

The DoE consists of 340 designs, distributed over the whole domain, and each design is analysed with a CFD simulation. A design is excluded from the DoE if the CFD calculation does not converge, or the solution is considered not satisfactory (i.e. $\eta < 70\%$). After this screening, only 298 feasible designs are retained for the DoE. Fig. 2.12 shows the values of the objective function and constraint for the design in the DoE. The design without a vortex along the blade are highlighted. It can be seen as this new design space allows the generation of geometries without vortex along the blade.

The surrogate built on the DoE brings to have a discrepancy between the expected and the computed efficiency of the design from the first SOGA iteration of 9.8% and a maximum expected improvement at the first EGO iteration of 5.4%. The discrepancy between the total pressure coefficient predicted by the kriging and the value computed by CFD is about the 5% of the target value. SBO with a SOGA algorithm and EGO are applied to the surrogate generated on this initial population to optimize the pump efficiency. During the optimization process, the convergence can be affected by the presence of designs with an not converged CFD solution. This issue is addressed in a different manner for the two strategies. In the SOGA optimization a dummy output is returned, characterized by $\eta = 70\%$ and $\psi = 0.7$. The efficiency value must be lower than the optimum; this value must be

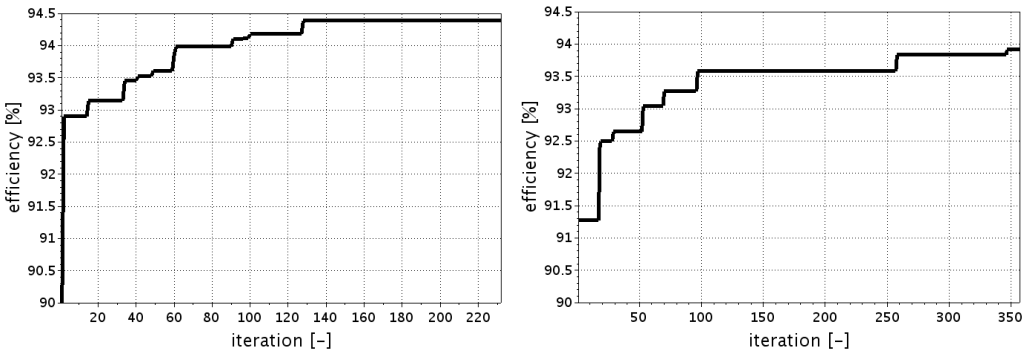


Figure 2.13: Convergence history for SBO with SOGA (left) and EGO (right)

chosen carefully because too small values can deteriorate the accuracy of the surrogate model. The value of the pressure coefficient is selected just outside the constraint. After a set of iterations, the designs that are unfeasible are removed, and the process is reinitialized. For the EGO approach a dummy output can not be used, as it always create instability issues. In this case when an unfeasible design is encountered, it is replaced with a feasible one, which is typically found in the neighbourhood, and then the optimization process continues.

During the optimization, designs with detachments near the trailing edge of the diffuser must be hindered, as explained in the previous paragraph. To penalize these configurations and move the algorithm away from this area, the efficiency of these design is limited to a maximum of $\eta = 90\%$.

Figure 2.13 shows the convergence history for the SOGA and the EGO strategy, and the maximum efficiency found by the algorithms at each iteration is plotted. The SOGA approach is stopped after about 200 iterations because the convergence is reached. Besides, the EGO strategy is ended after about 350 iterations, even if the convergence is not yet reached. The SOGA optimization converges in about 130 iterations and five reinitializations, with maximum efficiency, $\eta_{S,max} = 94.4\%$, and a $\psi_S = 0.891$. The EGO reaches, in about 350 iterations, a pseudo-optimal point featuring $\eta_{E,max} = 93.9\%$, and a $\psi_E = 0.883$. Both strategies provide a performance improvement with respect to the baseline ($\eta_B = 91.5\%$ and $\psi_B = 0.891$). In Fig. 2.14 the design evaluated by the two strategies are depicted on the chart $\psi - \eta$, while in Fig. 2.15 the same evaluations are represented in the input space. Notice that the EGO algorithm scouts a larger space than the SOGA.

Figure 2.16 shows a comparison between the baseline and blades optimized geometries for the impeller (left) and diffuser (right). In particular, the SOGA optimal geometry features a lower wrap angle, a lower chord

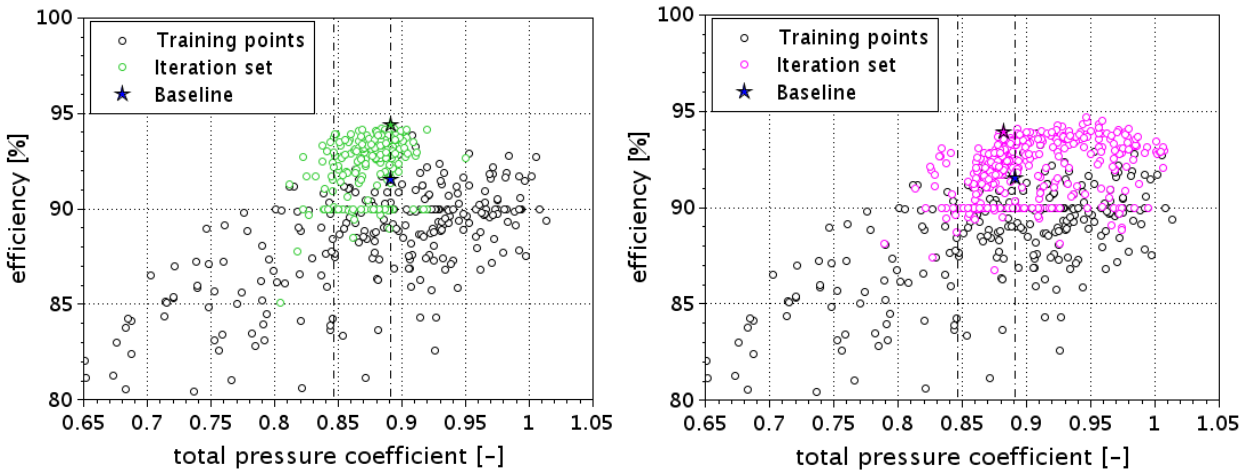


(a) *SBO with SOGA* (b) *EGO*

Figure 2.14: New designs during the optimization processes. The stars show the position of the baseline and the optimum for the two strategies (green star: SOGA, pink star: EGO)

Table 2.6: Values of the design variables for the two optima

| Variable | SBO with SOGA | EGO |
|---|---|---|
| $\gamma_{imp}$ | -110.2 | -105.0 |
| $\beta_1$ | -68.6 | -61.6 |
| $\beta_2$ | -72.3 | -74.2 |
| $\gamma_{dif}$ | 90.9 | 92.5 |
| $\alpha_3$ | 71.0 | 68.3 |
| $\alpha_4$ | 64.6 | 62.5 |
| $x_{t\_LEi}$ | 0.2497 | 0.1333 |
| $dr_{LE,i}$ | 0.06399 | 0.01900 |
| $k_{t,i}$ | -1.4515 | -1.8789 |
| $x_{t\_TE,i}$ | 0.8402 | 0.8250 |
| $x_{3\_TE,i}$ | 0.9201 | 0.9244 |
| $\alpha_{TE,i}$ | -1.0884 | -0.6945 |
| $x_{t\_LE,d}$ | 0.2319 | 0.1111 |
| $dr_{LE,d}$ | 0.09570 | 0.07361 |
| $y_{1\_LE,d}$ | 2.0014 | 2.1667 |
| $\alpha_{LE,d}$ | 0.02251 | 0.01500 |
| $x_{t\_TE,d}$ | 0.9406 | 0.9824 |
| $D_4$ | 593.9 | 584.6 |

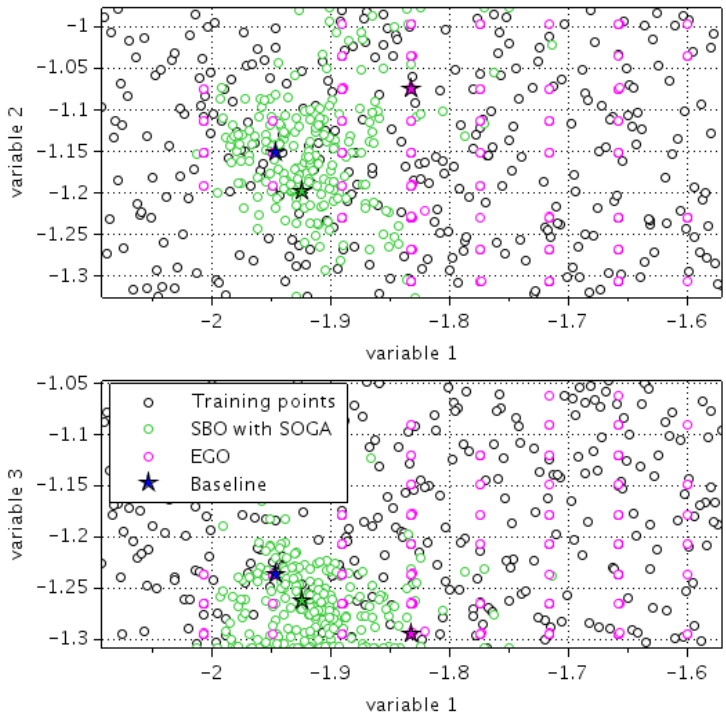


Figure 2.15: Position of the new designs during the optimization processes. Variable 1 is the stagger angle, Variable 2 is the inlet angle, Variables 3 is the outlet angle, of the impeller blades. The stars show the position of the baseline and the optimum for the two strategies (green star: SOGA, pink star: EGO)

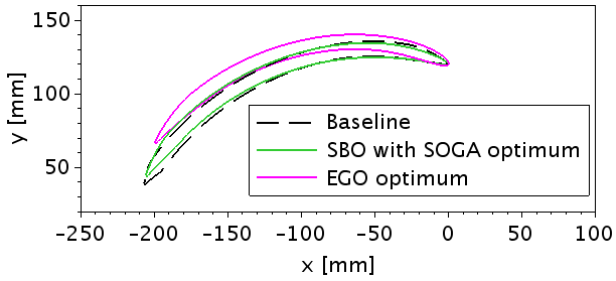


(a) *Impeller*

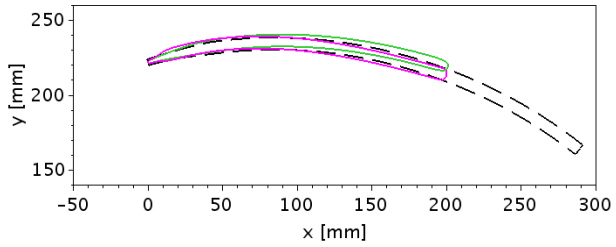


(b) *Vaned diffuser*

Figure 2.16: Comparison between the baseline and the optimized geometry

length and rounded leading and trailing edges for the impeller blade. The diffuser has a lower chord length, a smaller and rounded leading edge, and a lower diffuser angle. The EGO optimum is characterized by the lowest wrap angle and chord length and rounded leading and trailing edges. The diffuser has a lower chord length, a smaller and rounded leading edge, similar to the SOGA profile. Table 2.6 compares the design variables of the two optima.

The optimized geometries modifications described above allow a global reduction of the losses through the pump. Figure 2.17 shows the velocity (left column) and the pressure (right column) contours for the base-line (top), SOGA optimum (middle) and EGO optimum (bottom). The flow velocity for the impeller near the trailing edge is lower for both optima, while a lower velocity field on the pressure side is evident for the EGO optimum, as a consequence of the greater reduction of the wrap angle. The trailing edge of both optima is rounded and smaller to decrease the wake dimension and the corresponding losses. The pressure field for the impeller has a smoother increment inside the impeller channel, and the low-pressure zones near the end of the blade are removed. The velocity field of the diffuser blade features the absence of the recirculation zone for both optima, which allows a smoother recover of the static pressure and, as a consequence, a reduction of the chord length.

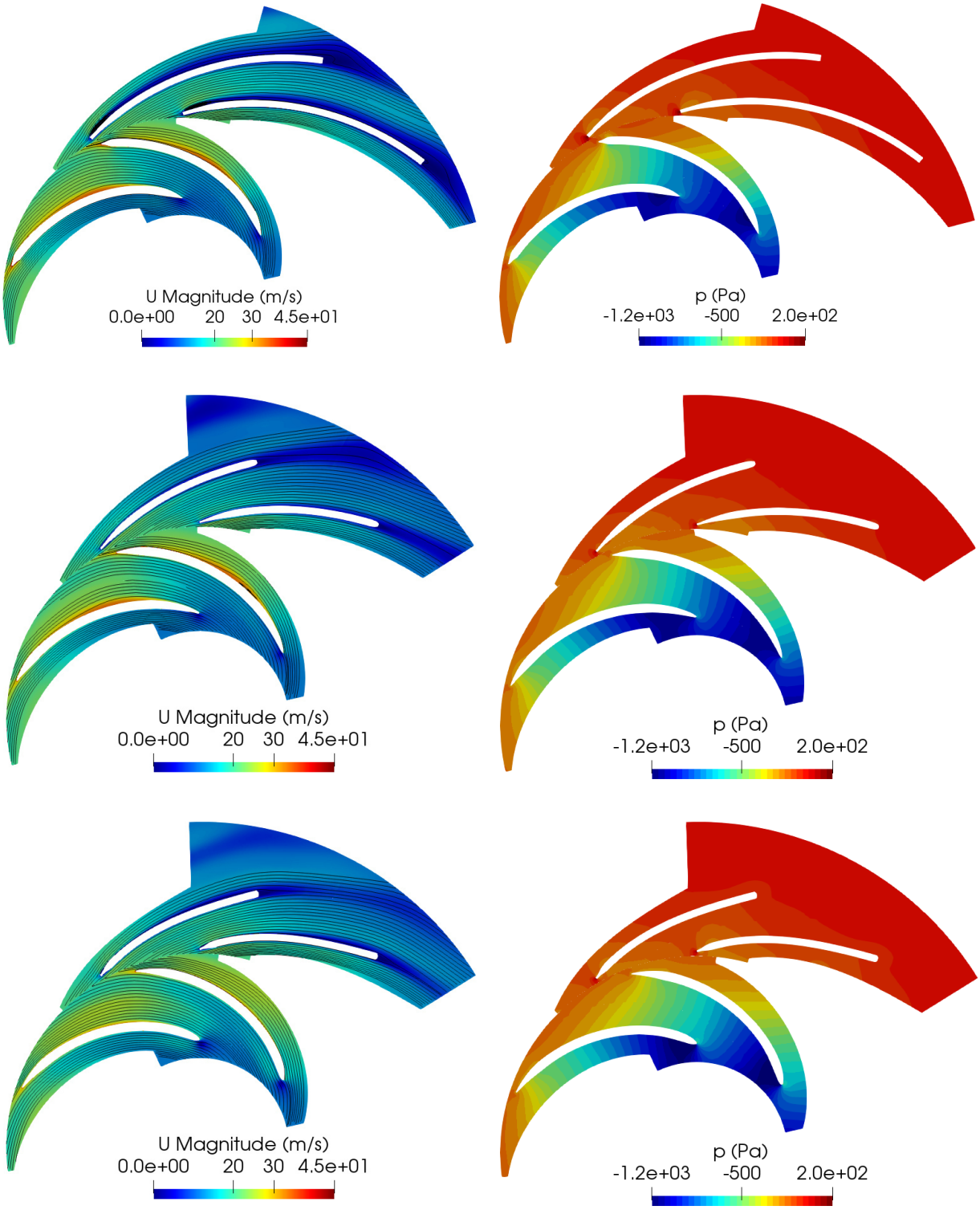


Figure 2.17: Velocity (left column) and pressure (right column) contours for the baseline (top), SOGA (middle) and EGO (bottom) geometry

# Chapter 3

# Uncertainty quantification assessment of the optimized geometry

In this Chapter the robustness assessment of the baseline and the optimal design through an uncertainty propagation study is presented. Two sources of uncertainty are considered: i) equipment uncertainties, i.e. the rotational speed of the pump shaft and the hydraulic system resistance, and ii) uncertainties of the inlet turbulent quantities in the CFD simulations (turbulence intensity and viscosity ratio).

## 3.1 Robust optimization and uncertainty quantification overview

Geometries provided by deterministic optimization approaches could show discrepancies between predicted and real performance, as they can be very sensitive to uncertainties related to operating conditions or the geometry. In facts, uncertainties are present in every engineering applications, such as turbomachines, and their influence on performance should be assessed. In Fig. 3.1 the possible effect of the uncertainty is shown. A deterministic optimization finds the configuration with the maximum value of the objective function. However, a small variation in some operational condition or geometric quantity can bring the performance down under an acceptable value. Instead, it can be preferred a second configuration, with a lower deterministic objective function, but more robust under a variation of uncertainty conditions.

In an uncertainty environment, the objective function and the constraint

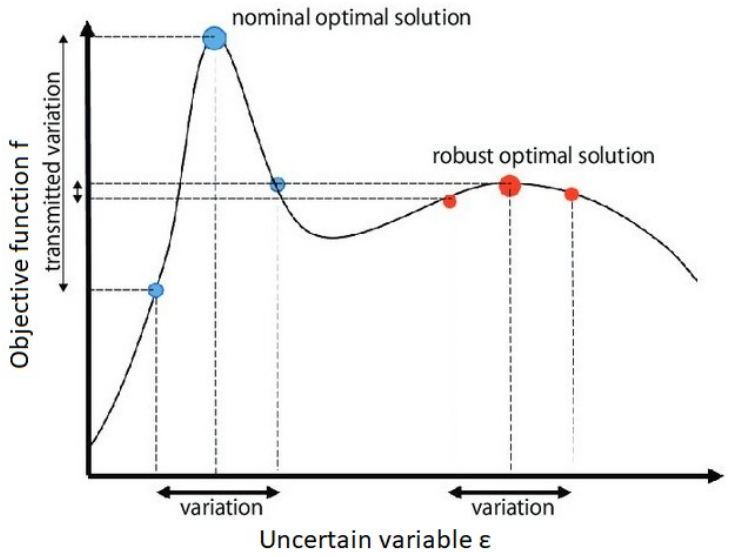


Figure 3.1: Comparison between deterministic and robust optima. Fig. adapted from [64]

depend not only on the design variables $\boldsymbol{x}$, as shown in Eq. 1.2, but also on a vector $\boldsymbol{\varepsilon}$ of the uncertainties. These uncertain variables are of two types: i) aleatory or statistical uncertainties if they are random unknowns that differ every time the experiment takes place and cannot be reduced, such as randomness in physical properties; ii) epistemic uncertainties if they are systematic and, in principle, due to the lack of knowledge, such as the inaccuracy of measurements or models.

In this context the formulation for a deterministic optimization, with a single objective function and no constraints, is the following:

$$\begin{aligned} \text{minimize:} \quad & f(\boldsymbol{x}, \boldsymbol{\varepsilon}), \\ \text{subject to:} \quad & \boldsymbol{x} \in \Delta. \end{aligned} \tag{3.1}$$

These approaches could provide geometries that are very sensitive to uncertainties related to operating conditions or the geometry [65]. To overcome this limitation, strategies to treat the uncertain variables $\boldsymbol{\varepsilon}$ during the optimization process have been developed in the last twenty years. Stochastic optimization (SO) refers to the optimization under uncertainty when the probability distribution $P$ of the uncertain variables is known. The objective is to minimize the expected value of the random objective function:

$$\begin{aligned} \text{minimize:} \quad & \mathbb{E}_P \left[ f(\boldsymbol{x}, \boldsymbol{\varepsilon}) \right], \\ \text{subject to:} \quad & \boldsymbol{x} \in \Delta. \end{aligned} \tag{3.2}$$

If the probability distribution $P$ is not known, the optimization is called Robust optimization (RO). This method can minimize the worst expectation of the objective function under all the possible distributions $P$ and can be expressed as

$$\begin{aligned} \text{minimize:} \quad & \max_{P} \left[ f(\boldsymbol{x}, \boldsymbol{\varepsilon}) \right], \\ \text{subject to:} \quad & \boldsymbol{x} \in \Delta, \\ & \boldsymbol{\varepsilon} \in U. \end{aligned} \tag{3.3}$$

In both RO and SO the expected value can be substituted with other statistics, such as the third quartile or the $90^{th}$ percentile, which are more meaningful in several applications.

RO or SO allow to optimize the mean performance, while minimizing the variation of performance caused by various uncertainties. However, the computation of the output probability distribution $P$ for every evaluation of the optimization process can be onerous. Less expensive study can be based on a deterministic optimization and a post-processing uncertainty propagation analysis [66]. The uncertainty quantification refers to the assessment of the impact of the input uncertainties $\boldsymbol{\varepsilon}$ on the objective function and constraint. Given $\boldsymbol{\varepsilon}$, these uncertainties are propagated through a computational model and statistical assessments are evaluated on the resulting responses. If the deterministic solution is robust enough, based on desired parameters, it is accepted as optimum, otherwise a robust optimisation is necessary.

Despite the abundant literature in the field of uncertainty quantification and robust optimization for wind or gas turbines and airfoils, the robust design, at least to the author's knowledge, was never applied to pump shape optimization. In contrast, only Salehi et al. [67] applied the uncertainty (geometrical and operational) propagation study to an existent centrifugal pump. This analysis shows as the variation of performances, such as the efficiency and the total pressure coefficient, of the proposed configuration, due to the uncertainties in the operating conditions, e.g. the rotational speed, and the geometry, e.g. manufacturing uncertainties, are negligible.

The objectives of the following section is to assess the robustness of the optimal design presented in Section 2.5. In fact, after a preliminary design, the pump is manufactured and tested in a test rig to verify the total pressure head and the efficiency, but the boundary conditions applied to the pump are subject to uncertainty. As a consequence, the effect of uncertainties on the pump performance should be assessed.

Table 3.1: Uncertain variables

| Uncertain variable | Deterministic value | Uncertainty range |
|---|---|---|
| Rotational speed $N$ | $2000rpm$ | $\pm 5rpm$ |
| System resistance $a$ | $1.21 \cdot 10^5 Pa \cdot s/m^3$ | $\pm 5\%$ |
| Turbulent intensity $I$ | $5\%$ | $0.1 - 10\%$ |
| Viscosity ratio $\frac{\mu_T}{\mu}$ | 10 | $0.1 - 50$ |

## 3.2 Uncertainty characterization

After the deterministic optimization of the ERCOFTAC pump (see Chapter 2), the robustness of the optimal profiles is assessed through an uncertainty quantification study. The considered uncertainties are related to the boundary condition of the test rig set-up that cannot be experimentally controlled and measured. The pump rotates at the operating rotational speed and is plugged in a hydraulic system, whose resistance is chosen to provide the operating mass flow rate. Two primary sources of uncertainty are considered: i) equipment uncertainties, i.e. the rotational speed of the pump shaft that also affects the flow rate, and ii) uncertainties of the inlet turbulent quantities in the CFD simulations.

In this work, the range for the turbulence parameters is set according to the literature best practice, while the range for the rotational speed and the system resistance are set based on standard use of the test equipment. Table 3.1 summarizes the range of uncertainty for the four uncertain variables. A uniform Probability Density Function (PDF) is defined for each uncertainty. Both optimal design found with SOGA and EGO are considered for the robustness assessment.

The implementation of the CFD solver requires the boundary conditions to be expressed in terms of rotational speed and flow rate. The flow rate is derived by intersecting the pump and test-rig curves for a fixed rotational speed and hydraulic resistance, respectively. The pump curves for the baseline and the two optima are computed using CFD (see Fig. 3.2 for the baseline geometry), while the system curve is estimated as $\Delta p_t = a \cdot Q^2$, *i.e.* a parabola passing through the working point, where the parameter $a$ is proportional to the system resistance. This formulation allows to apply uncertainty to the system resistance varying the parameter $a$. The intersection of the pump and test-rig curves defines the minimum and the maximum value of the flow rate given by the uncertainties of the rotational speed and the system resistance. A uniform PDF is assumed for the flow rate, even if this is equivalent to consider a broader uncertainty on the resistance (see Fig. 3.2). In fact, the grey area corresponds to the uncertainty for the rotational speed and system resis-

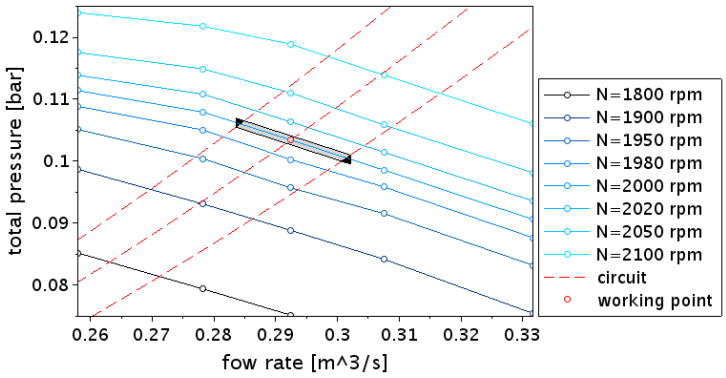


Figure 3.2: Pump curves of the baseline geometry for different rotational speeds, system curves and area of uncertainty. Grey area: uncertainty given by the rotational speed and the system resistance. Black area: uncertainty for considering the flow rate instead of the system resistance

tance, while the black area corresponds to the uncertainty added considering the flow rate instead of the system resistance. This assumption is acceptable because *i*) it ensures higher safety, and *ii*) the error of the uncertainty is small.

To assess the robustness of the optimal designs and the baseline, a Polynomial Chaos Expansion (PCE) ([68]), which is a well-known technique for propagating uncertainties at low computational cost, is employed. It is based on a multidimensional orthogonal polynomial approximation in terms of standardized random variables. A one-to-one correspondence exists between the choice of the stochastic variable and the polynomials. For instance, if a normal/uniform variable is considered, the corresponding polynomials are Hermite/Legendre polynomials. The random output $R$ is given by a finite-dimensional series expansion:

$$R(\xi) = \sum_{i=0}^{P} \alpha_i \Psi_i(\xi), \tag{3.4}$$

where $\Psi_i$ are the multidimensional orthogonal polynomials. They are derived from the family of hyper-geometric orthogonal polynomials or Askey scheme [69]. The $\alpha_i$ are deterministic coefficients of the expansion, computed through a multidimensional integration. A tensor product of a Gaussian quadrature rule of fourth order is employed to obtain the expansion coefficients and 625 evaluations are performed.

Statistics as mean and standard deviation can be computed analytically from the expansion. The PDF of the output is evaluated with a Monte

Table 3.2: Mean and standard deviation of the performance PDF for the baseline and the optimal geometries

| Geometry | $\mu_\psi$ [-] | $\sigma_\psi$ [-] | $\mu_\eta$ [%] | $\sigma_\eta$ [%] |
|---|---|---|---|---|
| Baseline | 0.889 | 0.016 | 91.3 | 0.25 |
| SBO with SOGA optimum | 0.891 | 0.013 | 94.1 | 0.37 |
| EGO optimum | 0.883 | 0.011 | 93.8 | 0.25 |

Carlo sampling performed directly on the polynomial approximation, which is a surrogate model of the function of interest with respect to the input parameters.

## 3.3 Results

A PCE-based Uncertainty Quantification study is performed for three design, *i.e.* the baseline and the two optima coming from the deterministic optimization. The mean, $\mu$, and the standard deviation, $\sigma$, of the total pressure coefficient and the efficiency are calculated (see Tab. 3.2). Notice that the mean efficiencies are slightly lower than the corresponding deterministic values; the two optima efficiency means appear to be close each other, even if the standard deviation of the SOGA optimum is greater ($\sim 50\%$). These values show a robust improvement of the optimum under uncertain operating conditions since the EGO-based optimal design features high efficiency with the same standard deviation of the baseline. This behaviour clearly shows that a deterministic optimization enhances the performances, while the sensitivity to some uncertain parameters remains the same as the baseline. Notice that the coefficient of variation for the optimal performance (computed as the standard deviation to mean ratio) is around 0.26%. In this perspective, a robust design optimization would be of interest only if the level of variability is judged too large.

The standard deviation of the pressure coefficient for the optima decreases with respect to the baseline. Moreover, the baseline standard deviation of the pressure coefficient is equal to 1.8% of the mean and cannot be ignored when the working point is constrained.

The PDF, which are estimated through a Monte Carlo sampling on the polynomial expansion and a Kernel Density Estimation (KDE), are also plotted in Fig. 3.3. The remarks based on the previous statistical moments are confirmed: *i*) the optimum distributions of the total pressure coefficient are tighter than the baseline PDF, and *ii*) the efficiency of optimal designs is always higher than the baseline efficiency, even if the SOGA optimum has a

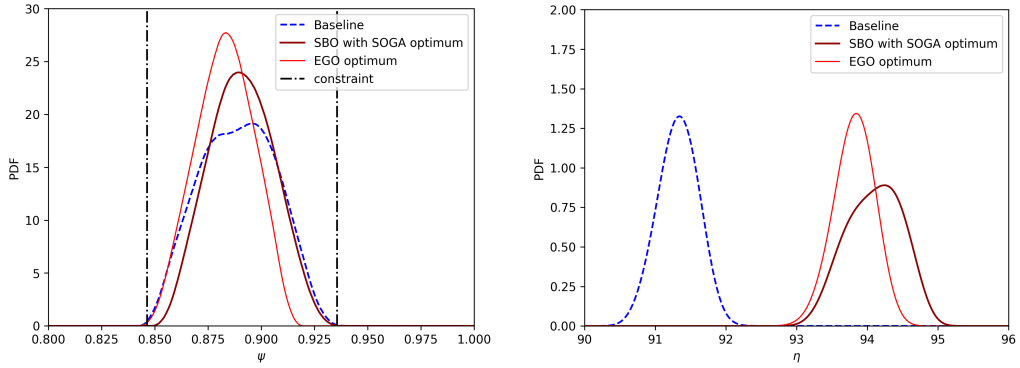


Figure 3.3: Comparison of the total pressure coefficient (left) and the efficiency (right) PDF for the baseline and the optimal geometries

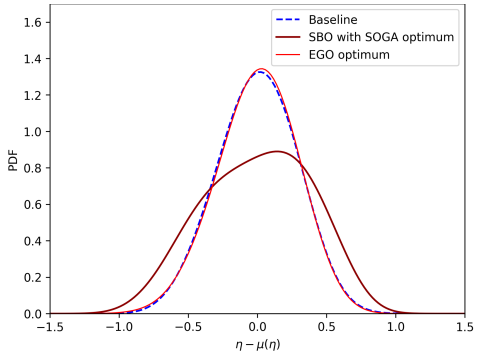


Figure 3.4: Comparison of the PDF shape for the baseline and the optimal geometries

wider distribution. For the sake of clarity, the shape of the efficiency PDF for the optimal and the baseline geometries are compared in Fig. 3.4, where all the distributions have the mean values centred in zero. The baseline and the EGO optimum show nearly the same distribution, while the SOGA optimum has a greater variability. However, the latter features potential efficiencies higher than 94.7%, which are very unlikely with the EGO design (see Fig. 3.3). The change in the total pressure coefficient, even if not negligible, does not break the constraint for all designs.

The influence of the four uncertain variables (rotational speed, test-rig resistance, turbulent intensity and viscosity ratio) on the total pressure coefficient and the efficiency uncertainties are investigated by computing Sobol indices, and the results are summarized in Tab. 3.3. The variability of the total pressure coefficient is mainly affected by the system resistance for all designs. The variance of the efficiency is explained primarily by the uncertainty on the test rig set-up for the baseline geometry, while for the two

Table 3.3: Total Sobol' index

| Uncertain variable | $\psi$ total Sobol' index | | | $\eta$ total Sobol' index | | |
|---|---|---|---|---|---|---|
| | Baseline | SOGA optimum | EGO optimum | Baseline | SOGA optimum | EGO optimum |
| Rotational speed $N$ | $5.86e-02$ | $7.37e-02$ | $8.93e-02$ | $3.69e-01$ | $1.19e-01$ | $2.71e-01$ |
| System resistance $a$ | $9.37e-01$ | $8.95e-01$ | $9.07e-01$ | $4.68e-01$ | $6.62e-02$ | $1.29e-01$ |
| Turbulent intensity $Tu$ | $4.51e-03$ | $2.06e-02$ | $2.99e-03$ | $1.26e-01$ | $4.41e-01$ | $3.12e-01$ |
| Viscosity ratio $\frac{\mu_T}{\mu}$ | $1.09e-03$ | $1.48e-02$ | $3.53e-03$ | $8.67e-02$ | $4.90e-01$ | $4.13e-01$ |

optima it is mainly influenced by the turbulent conditions, especially the SOGA optimum geometry.

# Part II

# Implementation, validation and application of the new DX-LES hybrid model

# Chapter 4

# Hybrid RANS-LES methods

First, the general formulation of DNS, LES and RANS is described. Then, their coupling in hybrid RANS-LES methods is shown and some specific hybrid models are presented.

## 4.1 Advantages of Hybrid RANS-LES methods

Direct Numerical Simulation (DNS), numerically solving the Navier-Stokes equations, is the most accurate tool to predict turbulent flows, but it is out of reach for industrial applications. Reynolds Averaged Navier-Stokes (RANS) models are widely used in industry, because they provide mean results, with engineering accuracy and reasonable cost, for several applications. However, a RANS simulation is not accurate in cases where the flow is dominated by internal instabilities (for example a flow around a bluff body or strong adverse pressure gradient). This is the case of the flow field in a pump at off-design conditions. On the other hand, Large Eddy Simulation (LES) solves the larger scale eddies and is accurate in most applications. However, LES is rarely used in industry, due to the computational cost: it requires 10 or 100 times the computational resources of a RANS model.

Hybrid RANS-LES methods couple RANS and LES approaches in order to exploit the advantages of both: on the one hand the affordability of the RANS and on the other hand the accuracy of LES. The idea of hybrid methods is to resolve RANS equation in the boundary layer, where LES requires a higher computational effort, and LES outside or where high detachment show up, to avoid RANS inaccuracy. Good results are shown in literature using this approach.

In the following, DNS, LES, RANS and hybrid RANS-LES approaches are presented more in detail.

## 4.2 Direct Numerical Simulation

In a turbulent flow, big eddies are generated by the interaction with walls and by flow separations. They contain the majority of the kinetic energy and transfer it to smaller scale by giving rise to gradually smaller and smaller fluctuations. The kinetic energy is dissipated as heat by friction through the smallest eddies. This process, called the *energy cascade* [70], is displayed in Fig. 4.1, where the energy spectrum of turbulence $E$ depending on the wavenumber $\kappa$ is shown. The dimension of the energetic big eddies can be expressed as

$$L_t = \frac{k^{3/2}}{\epsilon}, \tag{4.1}$$

where $k$ is the turbulent kinetic energy and $\varepsilon$ the dissipation rate. It is comparable to the characteristic length $L$ of the considered domain. The smallest eddies can be compared to the Kolmogorov scale:

$$\eta_k = \left(\frac{\nu^3}{\epsilon}\right)^{1/4}, \tag{4.2}$$

where $\nu$ is the kinematic viscosity.

A direct numerical simulation (DNS) [71] solves numerically the Navier-Stokes equations, so that all the turbulence scales, down to the size of the Kolmogorov scale, are resolved. The computational grid must have a number of cells at least equals to

$$N_c = C\frac{L^3}{\eta_k^3}, \tag{4.3}$$

where C is a constant greater than 1. Defining the turbulence Reynolds number $Re_t = L_t\sqrt{k}/\nu$ and by substituting Eqs. 4.1 and 4.2 in Eq. 4.3 the following relation is obtained [72]:

$$N_c = R_t^{9/4}. \tag{4.4}$$

The time step $\Delta t$ of the simulation has to be less than $\eta_k/U$, where U is a characteristic velocity. The total time to simulate is of the order $L/U$. Hence, an estimation of the number of time step can be obtained as

$$N_t = R_t^{3/4}. \tag{4.5}$$

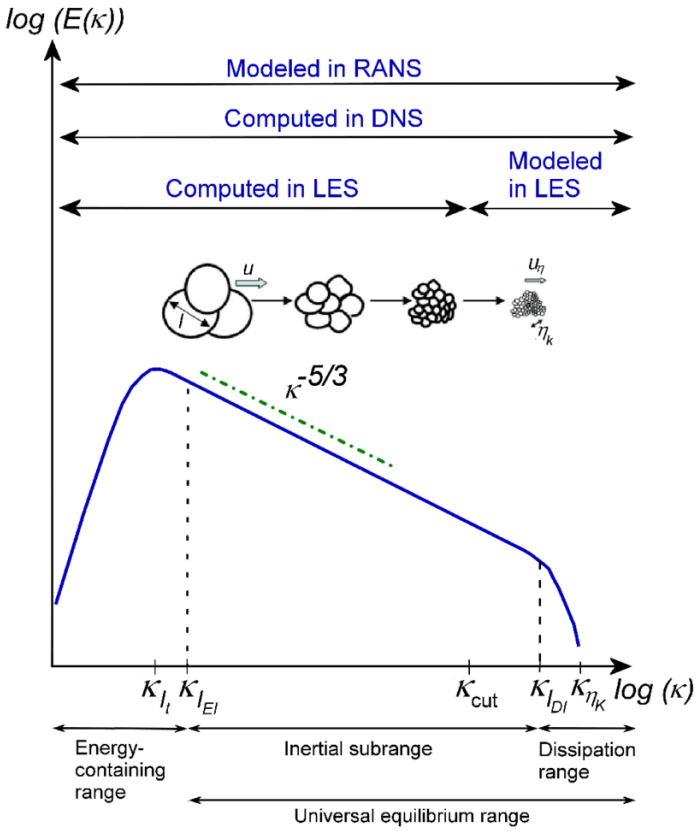


Figure 4.1: Production, energy cascade and dissipation in the energy spectrum of turbulence and modeled and resolved scales for the DNS, LES and RANS approach [73]

It is assumed that the turbulent Reynolds number is proportional to the Reynolds number Re through a constant close to 1/10. The total number of unknowns to be computed in a simulation is as follows:

$$N = N_c * N_t = \mathrm{Re}^3. \tag{4.6}$$

In practise DNS requires a too huge computational time, still beyond the today available computing power, even for low Re flow problems.

## 4.3 Large Eddy Simulation

To overcome the practical difficulties related to the DNS the Large Eddy Simulation (LES) [71, 74] was introduced. LES solves filtered Navier-Stokes equations, resolves the larger energetic eddies and models the smallest and

isotropic eddies. It is based on the idea of splitting the spectrum of turbulent energy in correspondence of a cutoff wavenumber $\kappa_{cut}$ placed in the inertial subrange (see Fig. 4.1) in order to decompose any generic variable $\phi$ as the sum of a resolved part and a modelled part associated to the largest wavenumber:

$$\phi = \bar{\phi} + \phi^{>}. \tag{4.7}$$

The filter operator is defined as the convolution on a variable $\phi$ and a filter $G$ in physical space [72]:

$$\bar{\phi} = G * \phi. \tag{4.8}$$

In practice the filter width $\Delta$ is often related to the grid cell size and typical expressions are the following:

$$\Delta_{cubeRoot} = (\Delta_x \Delta_y \Delta_z)^{1/3} \tag{4.9}$$

or

$$\Delta_{max} = \max(\Delta_x, \Delta_y, \Delta_z), \tag{4.10}$$

where $\Delta_x, \Delta_y, \Delta_z$ are the cell sizes in the three directions. The former is the cubic root of the cell volume, but it gives very low value in case of strong anisotropy of the cell. The latter corresponds to the maximum edge size and it is widely used. By applying the filter operator to Navier-Stokes equations and assuming negligible the commutation terms, LES equations can be written as

$$\frac{\partial \bar{u}_j}{\partial x_j} = 0, \tag{4.11}$$

$$\frac{\partial \bar{u}_i}{\partial t} + \frac{\partial}{\partial x_j}(\bar{u}_i \bar{u}_j) = -\frac{1}{\rho}\frac{\partial \bar{p}}{\partial x_i} + \nu \frac{\partial^2 \bar{u}_i}{\partial x_j \partial x_j} - \frac{\partial \tau_{SGS}(u_i, u_j)}{\partial x_j}, \tag{4.12}$$

where the subgrid scale (SGS) stress tensor $\tau(u_i, u_j)_{SGS}$ is equal to

$$\tau(u_i, u_j)_{SGS} = \overline{u_i u_j} - \bar{u}_i \bar{u}_j, \tag{4.13}$$

and represents the effect of the turbulent scale smaller than $L_{cut}$ on the resolved field. A set of equations in the filtered variables is achieved, but a model for the subgrid scale stress is needed to close the problem. As recommended by Pope [74], at least the 80% of the turbulent kinetic energy has to be resolved to retain sufficient accuracy of the method.

LES is less demanding than DNS, but in the boundary layer still requires a high number of cells, since $N_c$ has to be proportional to $\mathrm{Re}^{1.8}$, instead of $\mathrm{Re}^{2.25}$ of a DNS [75, 76]. This constraint restricts the application of LES in industrial applications.

## 4.4 Reynolds Averaged Navier-Stokes equations

The Reynolds Averaged Navier-Stokes equations are the averaged equations in the statistical sense of the NS equations. They are based on the hypothesis that any variable $\phi(x,t)$ can be decomposed into two components, i.e. a Reynolds-average part $\langle\phi\rangle$ and a fluctuation part $\phi'$:

$$\phi = \langle\phi\rangle + \phi', \tag{4.14}$$

under the following hypothesis: $\langle\langle\phi\rangle\rangle = \langle\phi\rangle$ and $\langle\phi'\rangle = 0$. The average operator should involve the ensemble average, but in practise it is defined as the average on a time sufficiently large with respect to the characteristic turbulent time-scale $\tau$ and sufficiently small with respect to the changing of the boundary conditions [72]:

$$\langle\phi(x,t)\rangle = \frac{1}{T}\int_0^T \phi(x,t,\tau)d\tau. \tag{4.15}$$

The time-scale separation of $t$ and $\tau$ is necessary for this average to be sensible. This is obviously true for statistically steady flows, where $\phi$ depends only on $x$ and $\tau$. It is true also for unsteady flows where the boundary conditions vary much slower than the characteristic time of turbulent fluctuation, so that the two time-scales are basically independent. When the flow is dominated by internal instabilities (for example a flow around a bluff body) and the boundary conditions changes in time, instead, the turbulent fluctuations and the mean flow have comparable time-scale and the hypothesis at the basis of RANS approach is not occurred [77]. However, under time-scale separation assumption the Reynolds average operator can be applied to the instantaneous Navier-Stokes equations, resulting in the following [72]:

$$\frac{\partial\langle u_j\rangle}{\partial x_j} = 0, \tag{4.16}$$

$$\frac{\partial\langle u_i\rangle}{\partial t} + \frac{\partial}{\partial x_j}(\langle u_i\rangle\langle u_j\rangle) = -\frac{1}{\rho}\frac{\partial\langle p\rangle}{\partial x_i} + \nu\frac{\partial^2\langle u_i\rangle}{\partial x_j\partial x_j} - \frac{\partial\tau_R(u_i,u_j)}{\partial x_j}, \tag{4.17}$$

and $\tau(u_i,u_j)_R$ is the Reynolds stress tensor defined as

$$\tau(u_i,u_j)_R = \langle u_iu_j\rangle - \langle u_i\rangle\langle u_j\rangle = \langle u_i\rangle\langle u_j\rangle + \langle u_i'u_j'\rangle. \tag{4.18}$$

It results from the average of the convection non-linear term and it is caused by the influence of the fluctuation on the mean flow. Additional equations

are necessary to model the $\langle u_i' u_j' \rangle$ term. The most widespread turbulence models are based on the Boussinesq hypothesis:

$$\tau(u_i, u_j)_R = -2\nu_t \langle S_{ij} \rangle + \frac{2}{3} k \delta_{ij}, \tag{4.19}$$

where $S_{ij}$ is the strain deformation tensor

$$S_{ij} = \frac{1}{2} \left( \frac{\partial u_i}{\partial x_j} + \frac{\partial u_j}{\partial x_i} \right), \tag{4.20}$$

and $\nu_t$ is the turbulent viscosity. It requires a model, usually one or two transport equation, to be computed.

The RANS approach is less demanding with respect to the LES: in particular RANS requires far fewer cells, as $N_c$ is proportional to $Re^{0.4}$. However, a RANS simulation is not accurate in cases where the mean flow is strongly affected by large scales, for example bluff bodies with highly detached flows or strong adverse pressure gradient. Furthermore, RANS approach provides averages properties of the flow, whereas information about the fluctuation are completely lost.

## 4.5 Hybrid RANS-LES approach

Even if LES and RANS equations are based on completely different foundations, they appear in a very similar set of equations. In addition, it is possible to find a physical relation between the filtering approach of LES and the statistical average of RANS, by splitting the variable $\phi$ in three different components:

$$\phi = \langle \phi \rangle + \phi^{<} + \phi^{>}. \tag{4.21}$$

In LES approach the mean field and the eddies till the cut-off wavenumber are resolved and correspond to the filtered field $\bar{\phi} = \langle \phi \rangle + \phi^{<}$, while the effect of the smallest eddies $\phi^{>}$ is modelled. In the RANS approach, the mean field $\langle \phi \rangle$ is resolved, while the effect of fluctuations $\phi' = \phi^{<} + \phi^{>}$ is modelled.

Starting from this similarity the two approaches can be coupled in order to exploit the advantages of both: on the one hand the affordability of the RANS and on the other hand the accuracy of LES.

Lots of hybrid methods have been developed in the last decades. Based on their characteristics, hybrid methods are classified in two main categories, even if different classification have been proposed by various authors. The standard classification distinguishes between *zonal* and *non-zonal* methods. According to Hanjalic [78], *zonal* methods applies RANS and LES models

in different domains divided by a sharp or a dynamic interface, whereas *non-zonal* or *global* methods exploits a set of equations that gradually goes from a RANS to a LES approach, based on some computed criteria. But this classification is ambiguous since in both cases different models are used in different zones. Some researchers use the term *zonal* referred only to model in which the interface is fixed in time or is predefined by the user.

A second and arguably more appropriate classification is proposed by Fröhlic [77], who divides between *unified* and *segregated* methods. *Unified* models use a unique momentum equation, with a unique $\tau_{model}$, which allows to switch between RANS and LES resolving the velocity field continuously. In *unified* models, *blending* and *interfacing* models can be distinguished, on the base of the formulation of $\tau_{model}$. The former use a blending function

$$\tau_{model} = f_{RANS}\tau_{RANS} + f_{LES}\tau_{LES}, \tag{4.22}$$

whereas in the latter $\tau_{model}$ allows to switch from a pure RANS to a pure LES and an interface is generated. This kind of models result from the similarities on the formulation of RANS and LES approach. The *segregated* models, instead, present two different domains and the variables are not continuous at the interface. In this case difficulties come from the boundary conditions that are to impose at the interface.

In this thesis the focus is on the *unified* models, and in particular on the Detached Eddy Simulation (DES) and derived models.

### 4.5.1 Detached Eddy Simulation

The first DES model was proposed by Spalart in 1997 [79]. It is based on the Spalart-Allmaras (SA) turbulent model [80, 81], in which the $\nu_t$ is expressed as a function of the effective turbulent viscosity $\tilde{\nu}$ and the following transport equation is resolved:

$$\begin{aligned}\frac{\partial\tilde{\nu}}{\partial t} + \frac{\partial}{\partial x_j}\left(\tilde{\nu}\langle u_j\rangle\right) = C_{b1}\tilde{\nu}\tilde{S} + \\ \frac{1}{\sigma}\left[\frac{\partial}{\partial x_j}\left((\nu+\tilde{\nu})\frac{\partial\tilde{\nu}}{\partial x_j}\right) + C_{b2}\frac{\partial\tilde{\nu}}{\partial x_j}\frac{\partial\tilde{\nu}}{\partial x_j}\right] - C_{w1}f_w\frac{\tilde{\nu}^2}{d_w^2}.\end{aligned} \tag{4.23}$$

$\tilde{S}$ is the vorticity magnitude and $d_w$ is the wall distance. The three terms on the right hand side of this equation correspond to production, diffusion and dissipation. A modification at the last term allows to cast the RANS model in a hybrid model. By replacing $d_w$ with the following function

$$\tilde{d} = min(d_w, C_{DES}\Delta), \tag{4.24}$$

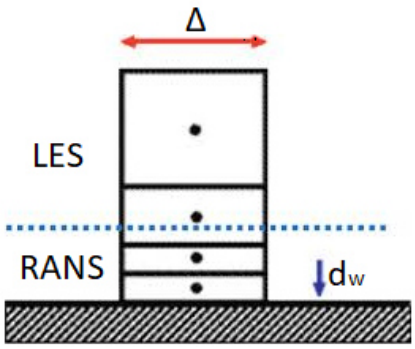


Figure 4.2: Interface between RANS and LES approach for the Spalart-Allmaras DES model, with $\Delta$ equal to the maximum edge size [77]

the equation switches from the original RANS model to a LES model, depending on the filter width $\Delta$. In facts, this formulation provides the spectral filtering of the turbulent equation that defines a LES approach. $C_{DES}$ is a constant equal to 0.65. Near the wall the distance $d_w$ is lower than the filter $C_{DES}\Delta$, depending on the grid size, and the RANS model is applied, while far from the wall it turns to be $d_w > C_{DES}\Delta$ and the LES is computed, as shown in Fig. 4.2.

Similarly, other DES model have been developed based on other RANS models. One of the most common version [82] derives from the shear stress transport ($k-\omega$ SST) model of Menter [83, 84]. The eddy viscosity is a function of the turbulent kinetic energy $k$ and dissipation rate $\omega$:

$$\nu_t = \frac{\mu_t}{\rho} = \frac{a_1 k}{max(a_1\omega, F_2 S)}, \tag{4.25}$$

where $S$ is the magnitude of the strain rate tensor. The $k$ and $\omega$ are computed with the following transport equations:

$$\frac{\partial(\rho k)}{\partial t} + \frac{\partial(\rho\langle u_j\rangle k)}{\partial x_j} = P_k - D_k + \frac{\partial}{\partial x_j}\left[(\mu + \sigma_k\mu_t)\frac{\partial k}{\partial x_j}\right], \tag{4.26}$$

$$\begin{aligned}\frac{\partial(\rho\omega)}{\partial t} + \frac{\partial(\rho\langle u_j\rangle\omega)}{\partial x_j} = \frac{\alpha\omega}{k}P_k - D_\omega + \\ \frac{\partial}{\partial x_j}\left[(\mu + \sigma_\omega\mu_t)\frac{\partial\omega}{\partial x_j}\right] + 2(1-F_1)\rho\frac{\sigma_{\omega 2}}{\omega}\frac{\partial k}{\partial x_j}\frac{\partial\omega}{\partial x_j}.\end{aligned} \tag{4.27}$$

The production term $P_k$ [85, 86] and the dissipation terms $D_k$ and $D_\omega$ are defined as

$$P_k = \min\left(\mu_t S^2, 10C_\mu k\omega\right), \tag{4.28}$$

$$D_k = \rho\beta_k \frac{k^{3/2}}{l}, \tag{4.29}$$

$$D_\omega = \rho\beta\omega^2. \tag{4.30}$$

$l$ is the turbulent length scale equal to

$$l = \frac{\sqrt{k}}{\omega}. \tag{4.31}$$

$F_1$ and $F_2$ are the SST blending functions. $F_1$ is defined as:

$$F_1 = \tanh\left(arg_1^4\right), \tag{4.32}$$

where

$$arg_1 = \min\left(\max\left(\frac{\sqrt{k}}{C_\mu\omega d_w}, \frac{500\nu}{d_w^2\omega}\right), \frac{4\rho\sigma_{\omega 2}k}{CD_{k\omega}d_w^2}\right),$$

$$CD_{k\omega} = \max\left(2\sigma_{\omega 2}\frac{1}{\omega}\frac{\partial k}{\partial x_j}\frac{\partial \omega}{\partial x_j}, 10^{-20}\right).$$

$F_2$ is defined as:

$$F_2 = \tanh\left(arg_2^2\right), \tag{4.33}$$

where

$$arg_2 = \max\left(\frac{\sqrt{k}}{C_\mu\omega d_w}, \frac{500\nu}{d_w^2\omega}\right),$$

and $d_w$ is the distance from the wall.

The generic model constant $\Psi$ without subscript 1 (inner state corresponding to $k-\omega$ formulation) or 2 (outer state corresponding to the $k-\epsilon$ formulation) is obtained as a blend, *i.e.* $\Psi = \Psi_1 F_1 + \Psi_2\left(1 - F_1\right)$. Model constants are summarized in Tab. 4.1.

Table 4.1: Model constants [85]

| | | | |
|---|---|---|---|
| $C_\mu = 0.09$ | $a_1 = 0.31$ | | |
| $\alpha_1 = 5/9$ | $\beta_1 = 0.075$ | $\sigma_{k1} = 0.85$ | $\sigma_{\omega 1} = 0.5$ |
| $\alpha_2 = 0.44$ | $\beta_2 = 0.0828$ | $\sigma_{k2} = 1$ | $\sigma_{\omega 2} = 0.856$ |

Starting from the $k-\omega$ SST turbulence model the hybrid model is defined by substituting the length scale $l$ with a composite length scale $\tilde{l}$

$$\tilde{l} = min(l, C_{DES}\Delta). \tag{4.34}$$

The $k-\omega$ SST DES model allows to switch from a RANS to an LES approach depending on the the length scale $l$ and the grid density. If $l < C_{DES}\Delta$ the Eqs. 4.26 and 4.27 are solved in the original RANS approach, while where $l > C_{DES}\Delta$ the model behaves like a LES model. In this model the switch is independent from the wall distance, but it depends on a physical quantity, which is a local characteristic of the flow.

Kok et. al. in 2004 [87] proposed a new hybrid model, called eXtra Large Eddy Simulation (X-LES), based on the $k-\omega$ TNT [88] turbulence model. In this thesis the same model is implemented based on the $k-\omega$ SST. The main difference with the $k-\omega$ SST DES model is in LES formulation, which is based on a well defined SGS model: the $k$-equation SGS model. In facts, the LES model of the $k-\omega$ SST DES model does not correspond to any SGS model. The X-LES model is obtained by replacing both the length scales in the dissipation term and the eddy viscosity (see Eqs. 4.26 and 4.5.1) by a composite function $\tilde{f}$, defined as

$$\tilde{f} = min(f, f_{LES}), \tag{4.35}$$

where $\tilde{f}$ can be either the length scale $\tilde{l}$ or the eddy viscosity $\tilde{\mu_t}$. In RANS and LES models, these quantities are defined as

$$l = \frac{\sqrt{k}}{\omega},$$

$$\mu_t = \rho \frac{a_1 k}{max(a_1\omega, F_2 S)},$$

$$l_{LES} = C_{DES}\Delta,$$

$$\mu_{t,LES} = C_{DES}\Delta\sqrt{k}.$$

### 4.5.2 Delayed DES

DES models present the so called *grey zone* at the interface. Spalart et al. [89] showed an unphysical behaviour of the original DES model in attached boundary layer, when the spacing parallel to the wall was refined lower than the boundary layer thickness $\delta$. In general, at the switch the LES model cannot start immediately to fully resolve the turbulence, due to the insufficient flow instabilities from RANS. The Modeled Stress Depletion

(MSD) refers to the reduction of eddy-viscosity switching from RANS to LES without a corresponding increasing of resolved turbulent content. MSD results in lower Reynolds stress levels compared to those provided by the RANS model. In addition, the depleted stresses decrease the skin friction coefficient and can lead to Grid-Induced Separation (GIS). Since this phenomenon has a major impact if the interface is in the boundary layer and since the grid affects the position of the switch, a refinement under critical values of $\Delta$ brings up the MSD.

Different way to overcome this issue as been proposed. A possible solution is to add a stochastic forcing to the momentum equations at the interface in LES region to accelerate the development of resolved turbulence [90]. Spalart et al. [89], instead, proposed a Delayed DES (DDES) version to avoid the MSD phenomenon. A shielding function $f_d$ is introduced to delayed the LES approach outside the boundary layer independently from the grid resolution. The function $\tilde{d}$ is redefined as follows:

$$\tilde{d} = d - f_d \max\left(0, d - C_{DES}\Delta\right) \tag{4.36}$$

and

$$f_d = 1 - \tanh\left[(8r_d)^3\right], \tag{4.37}$$

$$r_d = \frac{\tilde{\nu}}{\kappa^2 d_w^2 S}, \tag{4.38}$$

where $\kappa = 0.41$ the Von Karman constant. The model has been tested with satisfactory results, so that the Delayed version has been implemented in a similar manner also for the $k-\omega$ SST DES model by Gritskevich et al. [91].

# Chapter 5

# A New Model: the Delayed X-LES (DX-LES)

In this Chapter, the formulation of the delayed X-LES (DX-LES) model, implemented in the open-source software OpenFOAM v.1812, is presented.

## 5.1 Theoretical formulation

Among the different interfacing hybrid approaches proposed in literature the X-LES composite RANS-LES model of Kok et al. [87] has an attractive feature, i.e. a clearly defined subgrid-scale (SGS) model (the $k$-equation SGS model) for the LES formulation. The set of governing equations formally solved for X-LES consists in RANS equations closed by the $k-\omega$ TNT, where the $k$-equation dynamically reduces to the $k$-equation of the RANS turbulence model or to a LES subgrid-scale (SGS) model. However, X-LES and, in general, all DES models introduce the so called *grey area*, where the solution is neither pure RANS nor pure LES, since the switch from RANS to LES does not imply an instantaneous change of the resolution level. In this zone, where the model needs to convert from fully modelled turbulence (attached boundary layer) to mostly resolved turbulence (massive separation), the so called Modeled Stress Depletion (MSD) can appear. An ambiguous definition of the mesh in the boundary layer zone could prevent the correct behaviour, inducing the switch to the LES model in the boundary layer where RANS should be used (see paragraph 4.5.2).

The aim of this work is to revisit the X-LES approach, substituting its standard turbulence model with the SST and shielding the RANS from the DES formulation with the function proposed by Spalart [89] and adapted by Gritskevich [91].

The function $\tilde{f}$ is redefined as

$$\tilde{f} = f - f_d \max\left(0, f - f_{LES}\right), \tag{5.1}$$

where $\tilde{f}$ can be the turbulent length scale $l$ or the eddy viscosity $\mu_t$. The shielding function is defined as

$$f_d = 1 - \tanh\left[\left(C_{d1} r_d\right)^{Cd_2}\right], \tag{5.2}$$

and

$$r_d = \frac{\nu + \nu_t}{\kappa^2 d_w^2 \sqrt{0.5(S^2 + \Omega^2)}}, \tag{5.3}$$

where $\Omega$ is the magnitude of the vorticity tensor. Notice that $\nu_t$ in Eq. 5.3 corresponds only to the RANS definition (see Eq. 4.25). Similarly to SA-DDES [89], the X-LES model is preserved if in LES zone the shielding function $f_d$ is 1, indicating that the region is well outside the boundary layer or that a massive separation occurs. Otherwise, $f_d$ tends to zero and LES mode is delayed.

## 5.2 Calibration of the model

The values of $C_{d1}$ and $C_{d2}$ constants have to be chosen empirically so that MSD is avoided but the switch from RANS to LES is not excessively delayed. Changing the RANS turbulence model, the $r_d$ profile varies according to the turbulent eddy viscosity. Therefore, to balance this change, different values for $C_{d1}$ are set in SA-DDES and SST-DDES. At first the values of $C_{d1}$ and $C_{d2}$ in the DX-LES model are chosen equal to the values of the SST-DDES implementation of Gritskevich et al. [91], sharing the same RANS turbulence model.

To validate the performance of DX-LES model with respect to the MSD, a zero-pressure gradient boundary layer flow is investigated. The flow is assumed to be incompressible. The turbulent flat plate case with a unit Reynolds number $\mathrm{Re}_x = 5 \times 10^6$ is computed with different grid resolution. The maximum grid spacing at the wall changes abruptly from $\delta$ to a fraction $r$ of $\delta$ at $\mathrm{Re}_x = 5.2 \times 10^6$, with $\delta$ the boundary layer thickness at $\mathrm{Re}_x = 10^7$, similarly to Gritskevich [91]. Four grids, with different grid resolution, are tested (see Fig. 5.1). For all the grids, in wall normal direction 80 cells are used to cover the domain with a length of 1 and the height of the first cell near the wall guarantees $y^+$ a slightly less than 1. The domain is two-dimensional with a single cell in spanwise direction and $\Delta_x = \Delta_z$. The flow is computed in RANS mode with the DDES option activated.

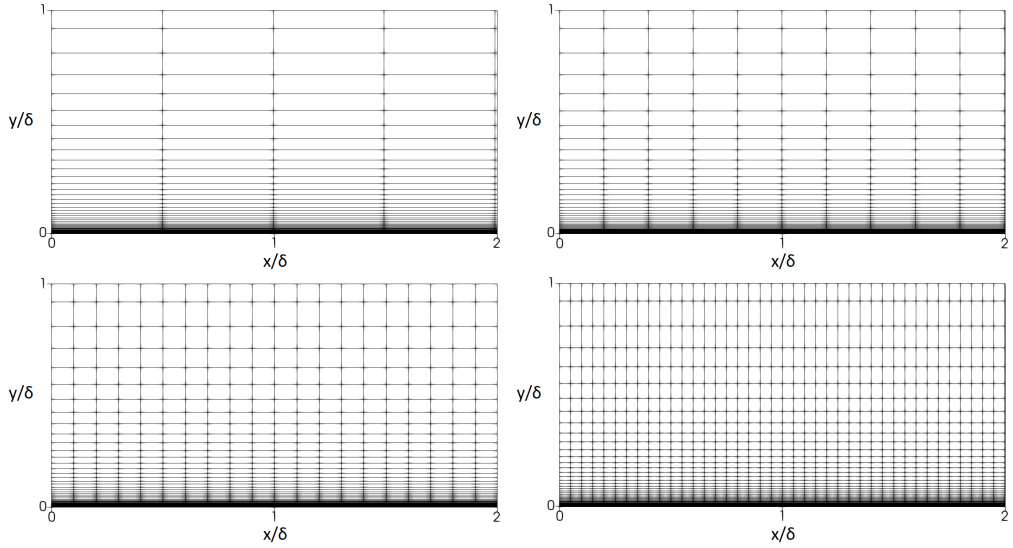


Figure 5.1: Turbulent flat plane. Computational grids with different $r$ value: 0.5 (top-left), 0.2 (top-right), 0.1 (bottom-left) and 0.05 (bottom-right)

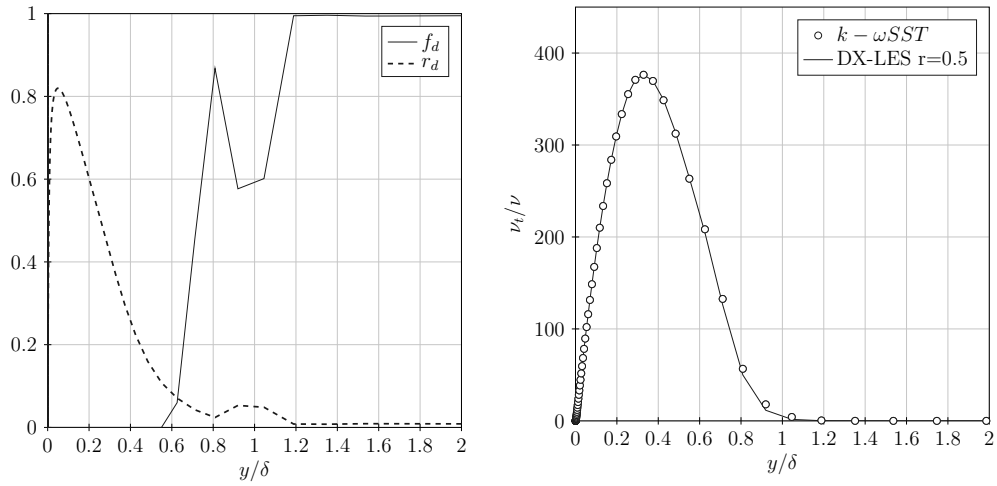


Figure 5.2: Turbulent Flat Plate. $r = 0.5$: $f_d$ and $r_d$ functions (left) and turbulent eddy viscosity $\nu_t/\nu$ (right)

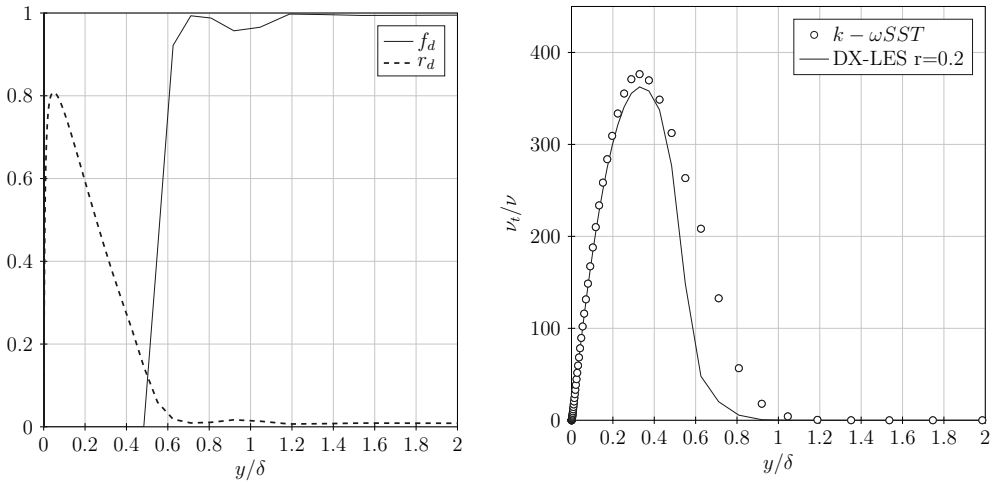


Figure 5.3: Turbulent Flat Plate. $r = 0.2$: $f_d$ and $r_d$ functions (left) and turbulent eddy viscosity $\nu_t/\nu$ (right)

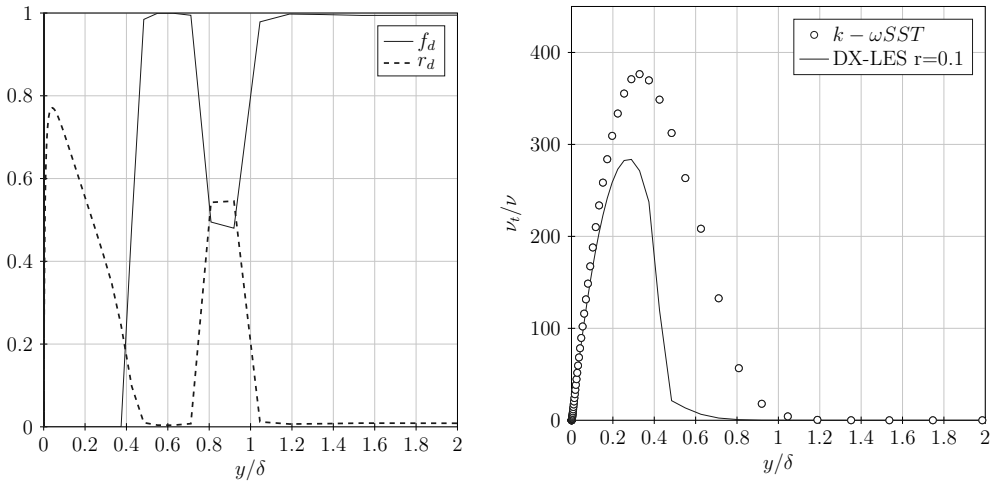


Figure 5.4: Turbulent Flat Plate. $r = 0.1$: $f_d$ and $r_d$ functions (left) and turbulent eddy viscosity $\nu_t/\nu$ (right)

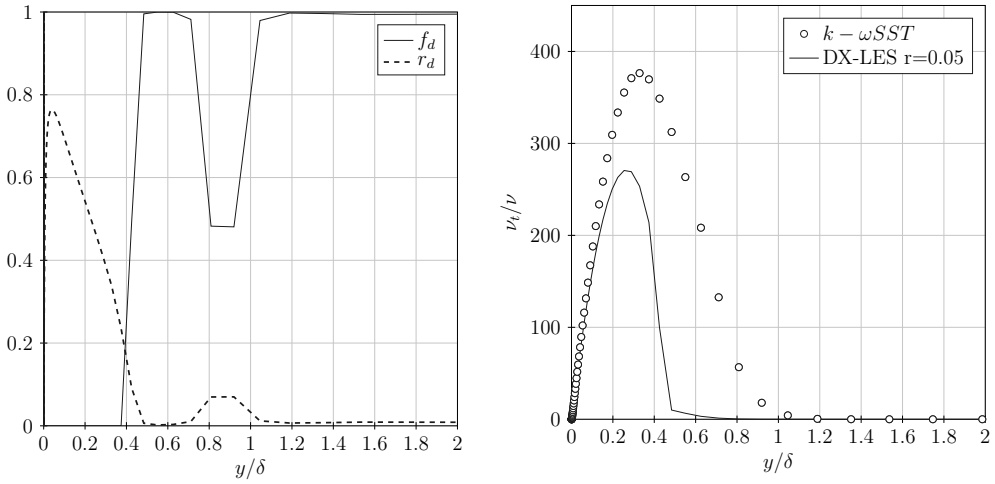


Figure 5.5: Turbulent Flat Plate. $r = 0.05$: $f_d$ and $r_d$ functions (left) and turbulent eddy viscosity $\nu_t/\nu$ (right)

Spalart [89] and Zhou [92] show how SA-DES and SST-DES models are strongly sensitive to the grid spacing, while the delayed models are not affected by this issue, at least till a certain refinement. To test the grid sensitivity of the DX-LES, the factor $r$ is set equal to 0.5, 0.2, 0.1 and 0.05 in the four grid. All the results are shown at $\mathrm{Re}_x = 10^7$.

In Fig. 5.2 the functions $r_d$ and $f_d$ are shown for the grid with $r = 0.5$, together with the computed turbulent eddy viscosity. The $f_d$ function starts to rise at $y/\delta = 0.5$. A decrease is clearly visible around $y/\delta = 1$ for low values of strain rate magnitude. Anyway the shielding function reaches the 1 just outside the boundary layer at $y/\delta = 1.2$, as expected. The turbulent eddy viscosity in the boundary layer correctly fits the RANS profile. In Fig. 5.3 the results are shown for the grid with $r = 0.2$. This condition corresponds to an *ambiguous grid*, which causes a drop in the turbulent eddy viscosity in DES models. In this case the shielding is a bit premature (around $y/\delta = 0.8$) and the eddy viscosity is slightly reduced at the end of the boundary layer, even if the profile is still acceptable. In Fig. 5.4 where the grid spacing is equal to $r = 0.1$, the switch is inside the boundary layer and the $\nu_t/\nu$ profile is completely wrong. The shielding early occurs at $y/\delta = 0.5$ and the predicted peak of turbulent eddy viscosity is about three quarters of the RANS peak. The same phenomenon is shown for $r = 0.05$ (see Fig. 5.5).

The effect of different values of the constants $C_{d1}$ and $C_{d2}$ is assessed on the grid with $r = 0.5$. Figure 5.6 shows the effect of $C_{d1}$ equal to 8, 15 and 20 for $C_{d2} = 3$, while Figure 5.7 shows the result for $C_{d2} = 2$, 3 and 4 for $C_{d1} = 20$. $C_{d1} = 8$ results in a early shielding inside the boundary layer.

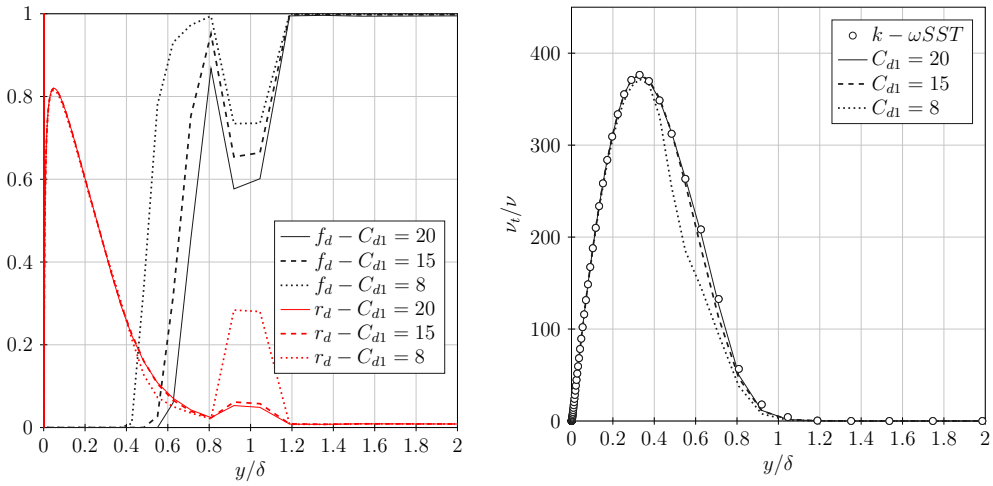


Figure 5.6: Turbulent flat plane. $f_d$ and $r_d$ functions (left) and and turbulent eddy viscosity $\nu_t/\nu$ (right) with $C_{d2} = 3$ and different values of $C_{d1}$ in the DX-LES model and $r$= 0.5

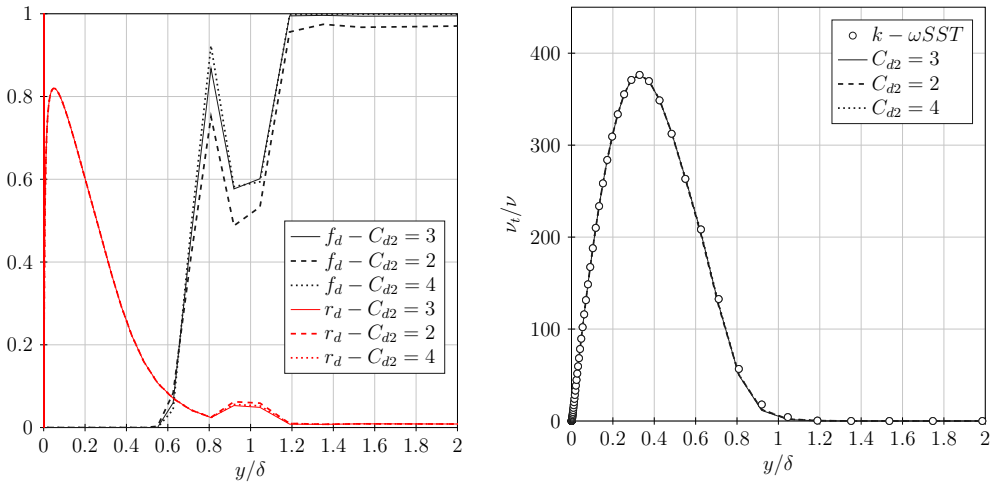


Figure 5.7: Turbulent flat plane. $f_d$ and $r_d$ functions (left) and and turbulent eddy viscosity $\nu_t/\nu$ (right) with $C_{d1} = 20$ and different values of $C_{d2}$ in the DX-LES model and $r$= 0.5

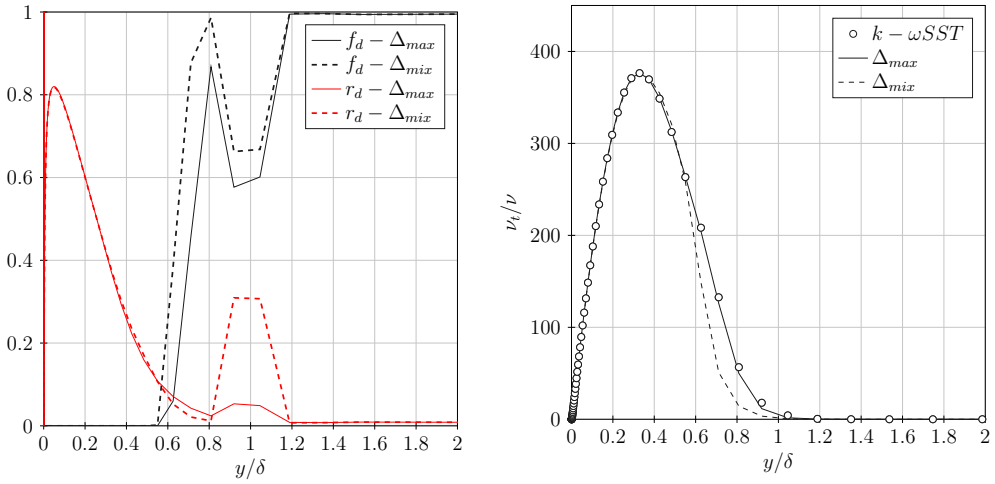


Figure 5.8: Turbulent flat plane. $f_d$ and $r_d$ functions (left) and and turbulent eddy viscosity $\nu_t/\nu$ (right) with different filer $\Delta$ and $r$= 0.5

Instead, the effect of $C_{d2}$ is negligible in the turbulent eddy viscosity profile. In the following $C_{d1} = 20$ and $C_{d2} = 3$ are set as constants of the model.

Finally, two different filter $\Delta$ are compared. The filter $\Delta_{max}$ (see Eq. 4.10) is compared with a mixed filter, which combines $\Delta_{max}$ with $\Delta_{cubeRoot}$ (Eq. 4.9) defined as follows [93]:

$$\Delta_{mix} = f_d \Delta_{max} + (1 - f_d)\Delta_{cubeRoot}. \tag{5.4}$$

This filter (used also in the previous computation) uses the $\Delta_{cubeRoot}$ filter in LES zone, while $\Delta_{max}$ is activated in the boundary layer. In fact, Breuer et al. [94] show as $\Delta_{cubeRoot}$ gives better results than $\Delta_{max}$ in eddy zone. On the other hand, $\Delta_{cubeRoot}$ returns too low values in anisotropic grids, like near the wall, and hence too low values of turbulent eddy viscosity. The blending filter allows to address both issues. In Fig. 5.8 the comparison is shown. The filter $\Delta_{mix}$ results in a early shielding and slightly affects the turbulent eddy viscosity profile in the final part of the boundary layer. The two filter are tested also in the turbulent channel flow and backward facing step test cases, to fully assess their performance.

In summary, from the turbulent flat plate case analysis the following findings are deduced: *i*) the DX-LES model performs well and avoids the MSD phenomenon up to a wall grid spacing equal to 0.2 $\delta$, *ii*) the best values of $C_{d1}$ and $C_{d2}$ are equals to 3 and 20 respectively, *iii*) both the $\Delta_{max}$ and $\Delta_{mix}$ filters give acceptable eddy viscosity profile and further comparison are shown in the following Chapter.

## 5.3 Implementation in OpenFOAM

The proposed hybrid model has been implemented in the open-source CFD software OpenFOAM (v1812) [95]. The SST-DES and SST-DDES models are taken as starting point for the implementation of the X-LES and DX-LES, respectively. The $k-\omega$ SST turbulence model in OpenFOAM is the model decribed in [84] with the updated coefficient in [85] [1], as described in Section 4.5.1. The optional $F_3$ term for the rough walls and decay control are disabled. The X-LES model is obtained by modifying the following function in the `kOmegaSSTDES.C` file: i) the definition of the turbulent eddy viscosity in the `correctNut` adding the switch operator,

```
template<class BasicTurbulenceModel>
void XLES<BasicTurbulenceModel>::correctNut(const
    volScalarField& S2)
{
    const volScalarField& k = this->k_;
    const volScalarField& omega = this->omega_;
    const volVectorField& U = this->U_;

    const volScalarField nutRAS(this->a1_*k/max(this->a1_*
    omega, this->b1_*this->F23()*sqrt(S2)));
    const volScalarField nutLES(sqrt(this->k_)*CXLES_*this->
    delta());

    // Correct the turbulence viscosity
    this->nut_ = min(nutRAS, nutLES);
    this->nut_.correctBoundaryConditions();
    fv::options::New(this->mesh_).correct(this->nut_);

    // Correct the turbulence thermal diffusivity
    BasicTurbulenceModel::correctNut();
}
```

ii) the composite function for the turbulent length scale `dTilda`

```
template<class BasicTurbulenceModel>
tmp<volScalarField> XLES<BasicTurbulenceModel>::dTilda
(
    const volScalarField& magGradU,
    const dimensionedScalar& CXLES
) const
{
    const volScalarField& k = this->k_;
    const volScalarField& omega = this->omega_;

```

[1] Note that the formulation of the production term in [85] is a typo; the correct form is reported in [86]

```
    return min(CXLES*this->delta(), sqrt(k)/(omega));
}
```

and iii) the production term in `epsilonByk` since the constant $C_\mu$ (`betaStar_` in the code) is included in `dTilda` in the SST-DES model, but not in the X-LES.

```
template<class BasicTurbulenceModel>
tmp<volScalarField::Internal> XLES<BasicTurbulenceModel>::
    epsilonByk
(
    const volScalarField& F1,
    const volTensorField& gradU
) const
{
    return sqrt(this->k_())*this->betaStar_/dTilda(mag(gradU)
    , this->CXLES_)()();
}
```

Then starting from the `kOmegaSSTDDES.C` file, the new `DXLES.C` file is obtained by modifying the composite function with the shielding i) in the turbulence eddy viscosity

```
template<class BasicTurbulenceModel>
void DXLES<BasicTurbulenceModel>::correctNut(const
    volScalarField& S2)
{
    const volScalarField& k = this->k_;
    const volScalarField& omega = this->omega_;
    const volVectorField& U = this->U_;

    const volScalarField nutRAS(this->a1_*k/max(this->a1_*
    omega, this->b1_*this->F23()*sqrt(S2)));
    const volScalarField nutLES(sqrt(k)*this->CXLES_*((1- fd(
    mag(fvc::grad(U))))*this->delta()+( fd(mag(fvc::grad(U))))
    *this->delta1()));

    // Correct the turbulence viscosity
    this->nut_ = nutRAS - fd(mag(fvc::grad(U))) * max(nutRAS-
    nutLES, dimensionedScalar(dimViscosity, Zero));
    this->nut_.correctBoundaryConditions();
    fv::options::New(this->mesh_).correct(this->nut_);

    // Correct the turbulence thermal diffusivity
    BasicTurbulenceModel::correctNut();
}
```

and ii) in the turbulent length scale.

```
template<class BasicTurbulenceModel>
tmp<volScalarField> DXLES<BasicTurbulenceModel>::dTilda
```

```
(
    const volScalarField& magGradU,
    const dimensionedScalar& CXLES
) const
{
    const volScalarField& k = this->k_;
    const volScalarField& omega = this->omega_;
    //const volScalarField& fd = this->fd(magGradU);

    const volScalarField lRAS(sqrt(k)/(omega));
    const volScalarField lLES(CXLES*((1-fd(magGradU))*this->
   delta()+(fd(magGradU))*this->delta1()));

    return max
    (
        lRAS
      - fd(magGradU)
       *max
        (
            lRAS - lLES,
            dimensionedScalar(dimLength, Zero)
        ),
        dimensionedScalar("small", dimLength, SMALL)
    );
}
```

Moreover, the magnitude of the vorticity tensor $\Omega$ is added in the $r_d$ function.

# Chapter 6

# Validation of the DX-LES model

In this Chapter, the proposed hybrid model has been validated on three test cases: *i*) the turbulent channel flow at Reynolds number $\mathrm{Re}_\tau = 2\,000$, based on the skin friction velocity $u_\tau$ and the channel height; *ii*) the turbulent flow over a backward facing step; *iii*) the flow around a circular cylinder for different Reynolds numbers, *i.e.* $\mathrm{Re} = 3\,900$ and $\mathrm{Re} = 140\,000$, based on the cylinder diameter and free-stream conditions. The predicted results are compared with available experimental data and reference numerical results. All the simulations have been run with the open-source CFD software OpenFOAM (v1812).

## 6.1 Turbulent channel flow

The accuracy of the proposed DX-LES model is first verified on a fully developed turbulent plane channel flow at Reynolds number $\mathrm{Re}_\tau = 2000$. The calculation of $Re$ is based on the half channel height $h$ and the skin friction velocity $u_\tau$. The turbulent channel flow is a challenging test case because in the boundary layer LES requires a mesh resolution scaling with $Re^{1.8}$ [75], which can be prohibitive for high Reynolds numbers; hybrid methods can represent a possible solution to alleviate LES computational cost. However, hybrid RANS-LES simulations of the channel flow can show the MSD. In fact, depending in the position of the RANS-LES interface, the model can fail the prediction of the log-law region. In this context, the proposed delayed version allows to improve the velocity profile estimation.

The simulation involves a channel section of dimensions $2\pi h \times 2h \times \pi h$ in streamwise, wall normal and spanwise directions, where $h$ is equal to 1. A

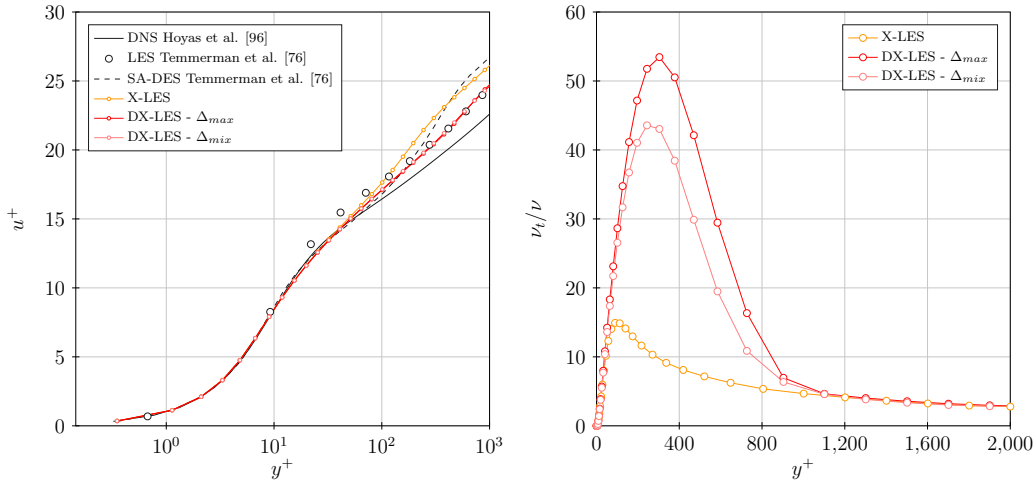


Figure 6.1: Turbulent channel flow at $Re = 2000$. Time- and spanwise-averaged velocity profiles $u^+$ (left) and time- and spanwise-averaged modelled viscosity profiles $\nu_t/\nu$ (right)

periodic condition is imposed in streamwise and spanwise direction, while at the wall a no-slip boundary condition is set and the mean wall shear stress is enforced to keep the flux constant. The computational grid is generated according to the Temmerman grid [76]. It consists of $N_x \times N_y \times N_z = 64 \times 64 \times 32$ elements, where $N$ is the number of cells in streamwise ($x$), wall normal ($y$) and spanwise ($z$) directions. The $\Delta y^+$ goes from 0.7 at the wall to 199 at the centre of the channel. The aspect ratio $\Delta x^+/\Delta z^+$ is equal to 1. The time step is set to guarantee a Courant number less than one. The results are compared to the DNS of Hoyas and Jiménez [96, 97] and the LES and the Spalart-Almaras DES results of Temmerman [76]. Both the $\Delta_{max}$ and $\Delta_{mix}$ filter are evaluated.

The DX-LES velocity profile in Fig. 6.1 is in good agreement with the LES of Temmerman [76], while the X-LES model overpredicts the mean velocity in the core region. This behaviour is caused by the MSD. The DX-LES modelled eddy viscosity (see Fig. 6.1) is higher than the X-LES viscosity near the wall, because of the deeper RANS layer, and it decreases smoothly after transition to LES region. The values of viscosity for the X-LES calculation in the RANS region are more than three times lower, so that at the switching to LES the resolved turbulence is too low. This leads to a lack of the shear stress at the interface in the X-LES field. This poorly prediction is visible in Fig. 6.2 (left) in the convex shape at around $y/h = 0.05$ of the total stress. As a consequence, the velocity gradient is overestimated in this zone. This is confirmed by the X-LES total turbulence kinetic energy (right), which is

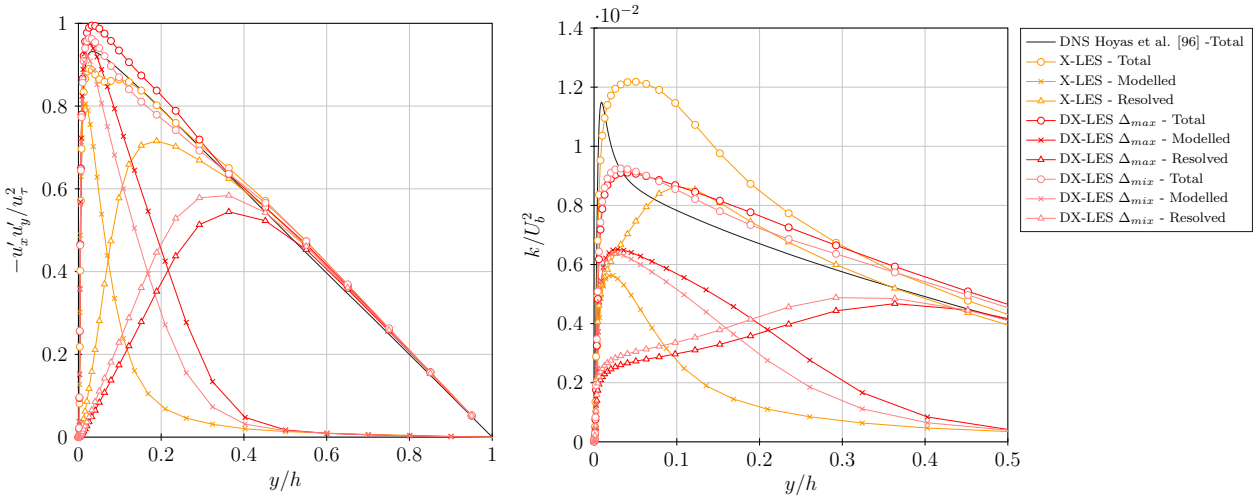


Figure 6.2: Turbulent channel flow at $Re = 2000$. Time- and spanwise-averaged shear-stress profile profiles $-u'_x u'_y/u_\tau^2$ (left) and time- and spanwise-averaged turbulent kinetic energy profiles $k/U_b^2$ (right)

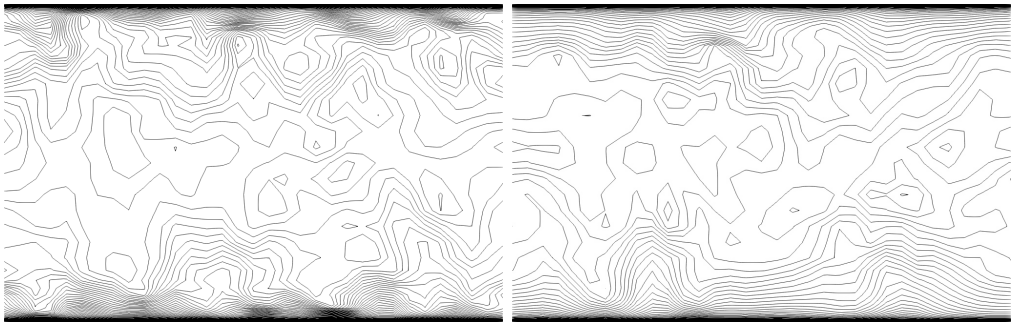

Figure 6.3: Turbulent channel flow at $Re = 2000$. Contours of streamwise velocity in planes normal to the flow with X-LES (left) and DX-LES (right)

overrated near the wall and then decreases in the LES core region. Also the DX-LES overrates the $k$ profile with respect to the experimental values and can't predict the peak near the wall, but the overestimation is significantly reduced.

It is obvious that the amount of the modelled quantities for the DX-LES are higher than for the X-LES model, and vice-versa for the resolved quantities, because the delayed model shifts the RANS-LES interface more inside the channel. In Fig. 6.3 the different size of the RANS layer is evident: in the X-LES velocity field the stretched contour area is shallower than for the DX-LES computation (with $\Delta_{max}$ filter). The greater amount of modelled quantities in DX-LES solution does not represent a loss of information but it is typical of a hybrid RANS-LES model, which ideally should model all the boundary layer. The presence in the boundary layer of LES deteriorates the prediction accuracy, because the mesh density is not sufficient.

Comparing the results of DX-LES with the two different filters, $\Delta_{mix}$ provides a earlier shielding, evident for a lower profile of $\nu_t$, but it has no effect on the velocity profile. However, the total shear stress is better predicted, in accordance with the DNS profile.

## 6.2 Backward facing step

The second test case is the backward facing step (BFS) at Re = 28 000, based on the inlet bulk velocity and the step height $h$. It is commonly used to test the capability of the model to avoid the MSD and it has been used to validate the delayed version of Spalart [89] and of the $k-\omega$ SST DDES from Gritskevich [91]. The computational grid (see Fig. 6.4) used in [89, 91] has been reproduced in order to compare the results. The domain extends from $-4h$ to $20h$ in streawise direction, the step is located at $x = 0$ and the inlet channel height is $4h$. In the spanwise direction the channel width is $4h$ and it is discretized with 80 cells. The height of the first cell near the wall is about 0.0001 that corresponds to $y^+ < 1$. The grid consists of about 2.2 million hexahedral cells. The maximum Courant number is 0.1, equivalent to a non-dimensional timestep of about 0.002, and the data are averaged in time over 160 000 timesteps. A periodic condition is imposed in spanwise direction and a no-slip boundary condition at the walls. At the outlet a fixed pressure is set. At the inlet the velocity and the turbulent quantities profiles are imposed. These profiles have been obtained by the simulation of the channel flow at the same Re, averaging the profile in the spanwise direction.

Fig. 6.5 highlights the RANS and the LES regions in the DX-LES computation, obtained with $\Delta_{max}$ and $\Delta_{mix}$ filters. As expected the RANS ap-

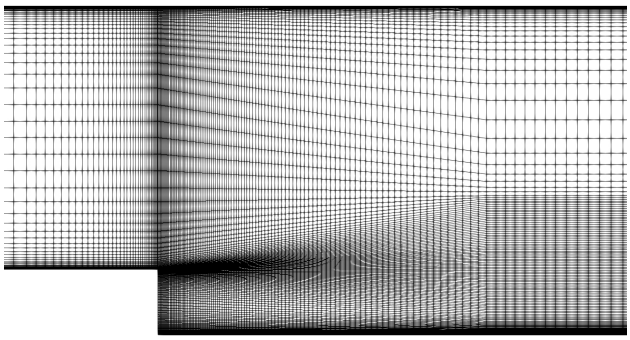

Figure 6.4: Backward facing step at $Re = 28\,000$. Detail of the computational grid

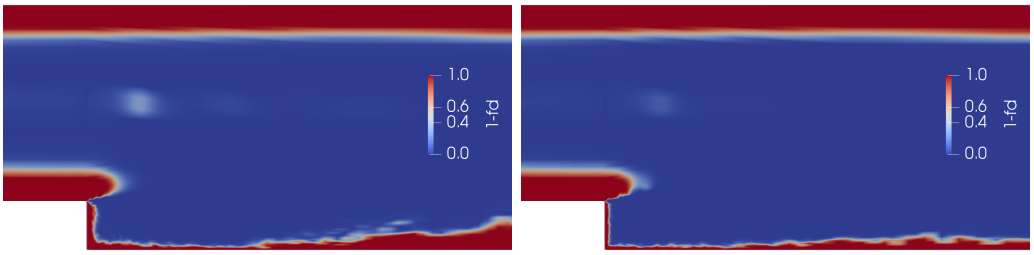


Figure 6.5: Backward facing step at $Re = 28\,000$. $1 - f_d$ function, DX-LES with $\Delta_{max}$(left) and DX-LES with $\Delta_{mix}$ (right)

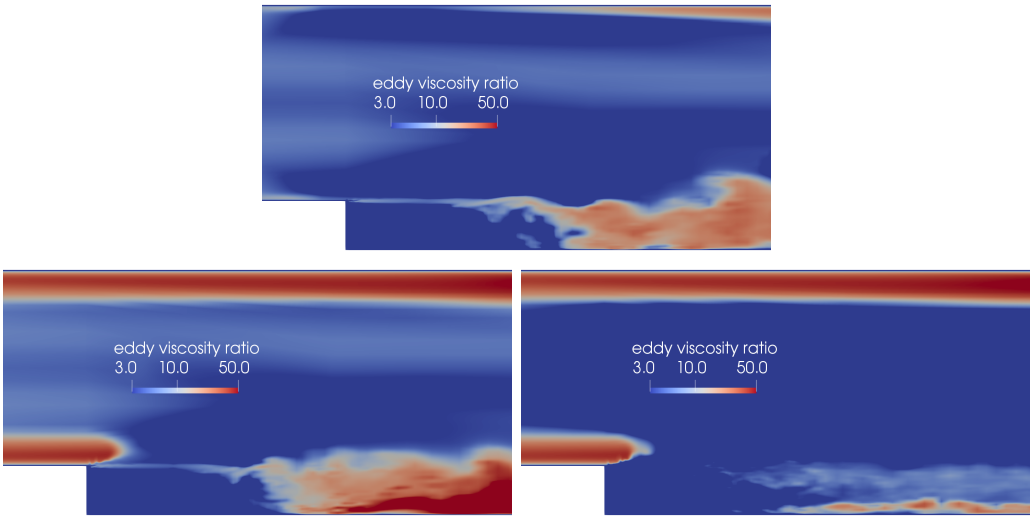


Figure 6.6: Backward facing step at $Re = 28\,000$. Eddy viscosity ratio with X-LES (top), DX-LES with $\Delta_{max}$(bottom-left) and DX-LES with $\Delta_{mix}$ (bottom-right)

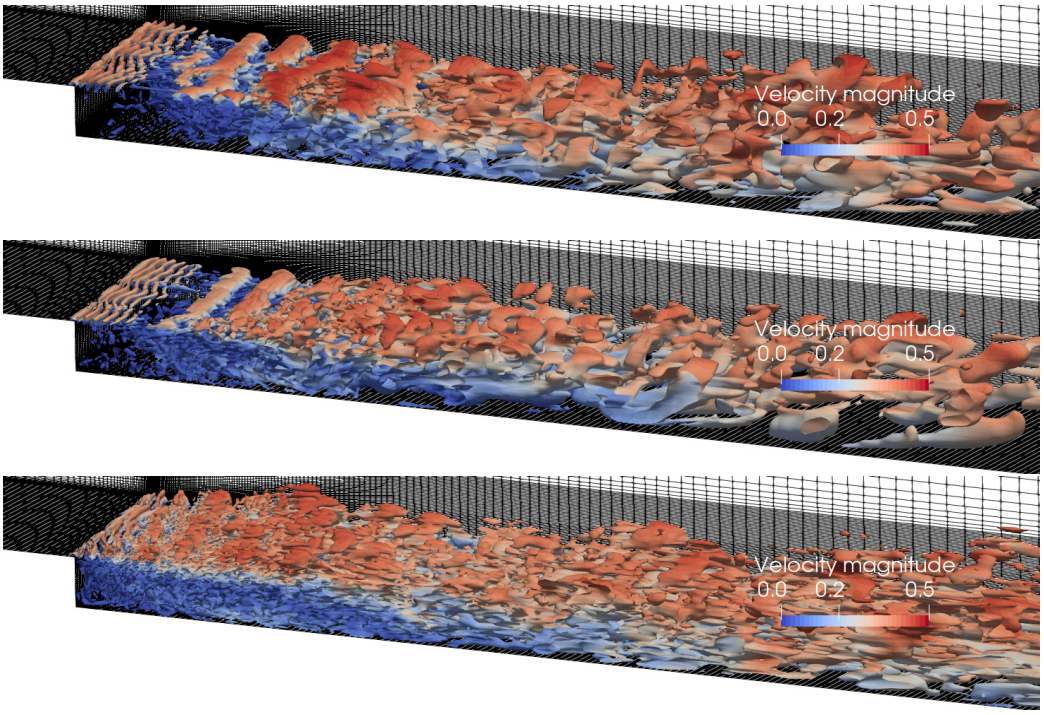


Figure 6.7: Backward facing step at $Re = 28\,000$. Isosurfaces of Q-criterion coloured with the velocity magnitude contours with X-LES (top), DX-LES with $\Delta_{max}$(middle) and DX-LES with $\Delta_{mix}$ (bottom)

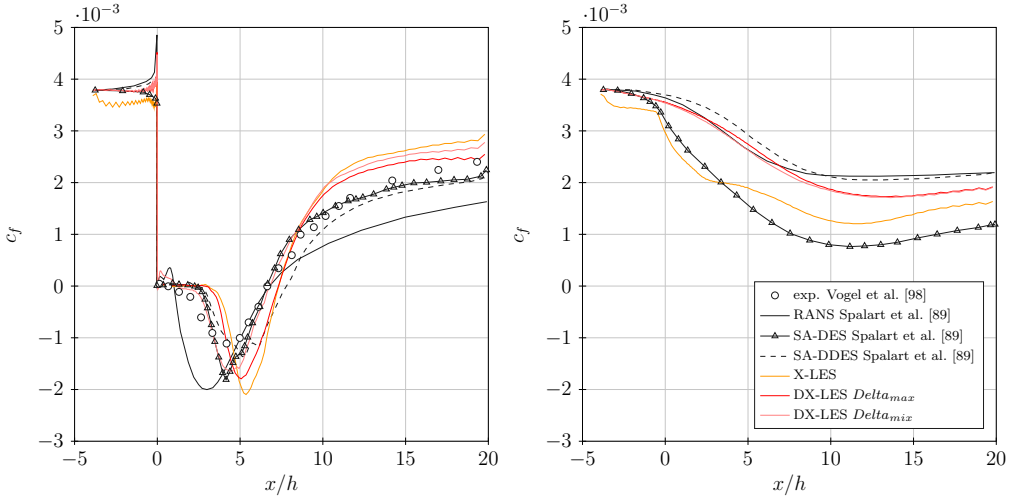


Figure 6.8: Backward facing step at Re = 28 000. Time- and spanwise-averaged skin friction coefficient $c_f$, step side (above), opposite side (below)

proach (red zone) is enabled in the attached boundary layers upstream the step and at the upper wall, while near the wall just downstream the step, where the separation occurs, the model switches to LES (blue zone). Differences, caused by the filter, are visible downstream of the recirculation zone, where the use of the filter $\Delta_{mix}$ provides a thinner RANS layer. The same difference is evident in Fig. 6.6, where a higher value of eddy viscosity $\nu_t$ means a higher level of modelled turbulence that corresponds mainly to the RANS region. The level of turbulent eddy viscosity with $\Delta_{max}$ downstream of the recirculation zone is higher than in the boundary layer because the resolved component is drastically suppressed. This is confirmed in Fig. 6.7, where isosurfaces of the Q-criterion are displayed: smaller turbulent structures develop near the step and especially towards the outlet with $\Delta_{mix}$.

It is noteworthy also the behaviour of the X-LES model. The RANS layer is extremely narrow along the walls with attached flow. In Fig. 6.6 the level of $\nu_t$ shows as the LES approach for the X-LES model gets into the boundary layer and the MSD phenomenon appears. The MSD is evident for X-LES in Fig. 6.8 (right), where the skin friction on the upper wall is shown. The DX-LES model instead, delaying the switch to LES, avoids the MSD and ensures a better estimation of the friction coefficient $c_f$. At the upper wall RANS solution is taken as reference, because the flow is completely attached.

In the zone downstream the step, where the separation is induced by the step itself, both the models perform well, especially with respect to the RANS. The effect of different filters is also analysed and a better behaviour can be observed with the $\Delta_{mix}$. In particular, this filter allows to better

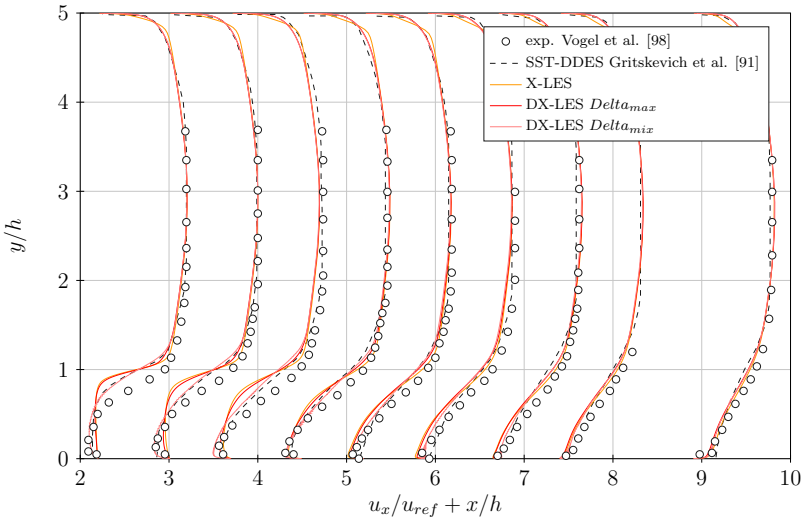


Figure 6.9: Backward facing step at Re = 28 000. Time- and spanwise-averaged streamwise velocity profiles at $x/h = 2.2, 3.0, 3.7, 4.5, 5.2, 5.9, 6.7, 7.4, 8.9$. $u_{ref}$ is the freestream velocity at $x = 3.0$

predict the position of the adverse peak in the friction coefficient along the streamwise coordinate and better fit the experimental profile.

A comparison between the SA-DDES of Spalart [89] is also performed in Fig. 6.8. At the bottom wall downstream of the step, the SA-DDES model better predicts the magnitude of adverse peak in the friction coefficient, while the DX-LES (with $\Delta_{mix}$) correctly estimates the streamwise position of the peak. At the outflow, bottom wall, the SA-DDES underpredicts the $c_f$ value, while the DX-LES overpredicts it. At the opposite side the DX-LES model better matches the coefficient untill $x/h = 7$, but underestimates the profile after that point, while the SA-DDES $c_f$ has all over the wall higher values than the DX-LES and correctly overlaps the curve at the outlet.

In Fig. 6.9 and 6.10 the streamwise velocity and the velocity fluctuations profiles downstream of the step are plotted and compared with the SST-DDES results of Gritskevich [91]. Both the models well predict the velocity profiles with minor differences. Again, the advantage in using the $\Delta_{mix}$ is evident: it results in a better prediction of the velocity profile, at $x/h = 2.2, 3.0$ and 3.7 around $y/h = 0.8$, and a better estimation of the peak of the velocity fluctuations at the same streamwise position.

In summary, the advantages of the DX-LES with respect to the X-LES model lies in the capability to accurately predict the skin friction coefficient. Moreover, the benefit in using the blend filter $\Delta_{mix}$ is evident in the near

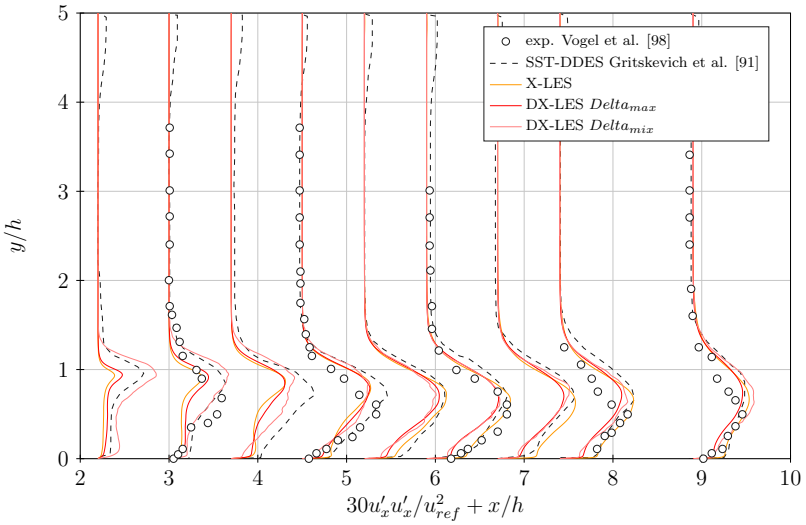


Figure 6.10: Backward facing step at Re = 28 000. Time- and spanwise-averaged streamwise velocity fluctuations profiles at $x/h = 2.2, 3.0, 3.7, 4.5, 5.2, 5.9, 6.7, 7.4, 8.9$. $u_{ref}$ is the freestream velocity at $x = 3.0$

wall region after the step. The blend filter avoids the growth of the RANS zone after the flow reattachment. For this reason, only the filter $\Delta_{mix}$ will be used in the following computations.

## 6.3 Turbulent flow around a circular cylinder at Re = 3 900

Finally, a common case study for external flows is chosen to validate the DXLES model. In particular, the turbulent flow around a circular cylinder is investigated at two different Reynolds number. In this paragraph the sub-critical Reynolds number Re = 3 900, based on the cylinder diameter and free-stream conditions, is selected. In sub-critical flow regime, the boundary layer is laminar until the separation where the transition takes place in the separated shear layer. The phenomenology of the flow field in the wake of the cylinder is largely driven by the laminar-turbulent transition of the shear layer with the creation of Kelvin-Helmholtz instabilities, the break-up of the shear layer and an asymmetric Von Kármán vortex shedding. Hybrid models can be expected to provide results comparable to LES.

Literature reports a considerable amount of information on this testcase, which can be considered as a benchmark for turbulent flows. Reference data provide values for the most important integral quantities, such as the forces

on the wall (pressure coefficient and vorticity) and the wake dynamics behind the cylinder (velocity profiles, first- and second-order statistics profiles). For the integrals on the wall, Norberg [99] described pressure measurements on the cylinder for Re = 3 000 while Son and Hanratty [100] the wall vorticity for Re = 5 000. For the first-order statistics, Ong and Wallace [101] managed to accurately measure velocity and vorticity vectors in the near wake outside the recirculation bubble and proposed turbulence profiles and power spectra of the components of the velocity at several locations between $4 \leq x/D \leq 10$. Lourenco and Shih [102] described measurements also in the recirculation region of the flow ($1.06 \leq x/D \leq 10$) where statistical quantities were assessed even though this particle image velocimetry (PIV) experiment was not designed for this purpose. Nevertheless, these results were used as reference of several numerical simulations, e.g. Mittal and Moin [103] and Wissink and Rodi [104]. Recently, the flow around a circular cylinder at Re = 3 900 was studied both numerically, with LES, and experimentally, with PIV and hot-wire anemometry (HWA) methods, by Parnaudeau et al. [105]. The PIV data of Parnaudeau et al. [105] differs from Lourenco and Shih [102], while they are at the same time similar with the HWA data of Ong and Wallace [101].

Several high-fidelity LES, or implicit LES, and DNS were carried out during the last two decades. The first to perform a numerical analysis with a LES for this test case was Beaudan and Moin [103]. In recent years the work by Lysenko et al. [106] is of particular interest in the OpenFOAM community. Simulations were carried out to understand the accuracy of two different sub-grid scale models for LES, a conventional Smagorinsky and a dynamic $k$-equation eddy viscosity. Wissink and Rodi [104] performed a DNS at Re = 3 300 in order to study the influence of the spanwise length of the computational domain with results perfectly consistent with the experiments of Parnaudeau et al. [105].

Three different computational meshes have been used with the same rectangular domain (H-type) but different number of elements in each direction, in order to prove a convergence of the results with DX-LES. The meshes have 395 920 (coarse), 1 088 958 (medium) and 3 110 200 (fine) elements. Figure 6.11 shows a detail near the cylinder of the meshes. The cylinder is discretized with 160, 240 and 320 elements along circumferential direction, while the spanwise direction has 28, 42 and 56 elements. The mesh has a spanwise extension $L_z = 2D$, and a streamwise extension $L_x = 40D$, $10D$ upstream and $30D$ downtream, and a crosswise extension $L_y = 20D$ with a periodic condition. It can be seen that the elements of the meshes near the cylinder, in the O-type part of the mesh, have been only stretched in the radial direction to avoid the occurrence of numerical inaccuracies due to unfavorable mesh aspect ratios. In fact, the elements have a quasi-cubic as-

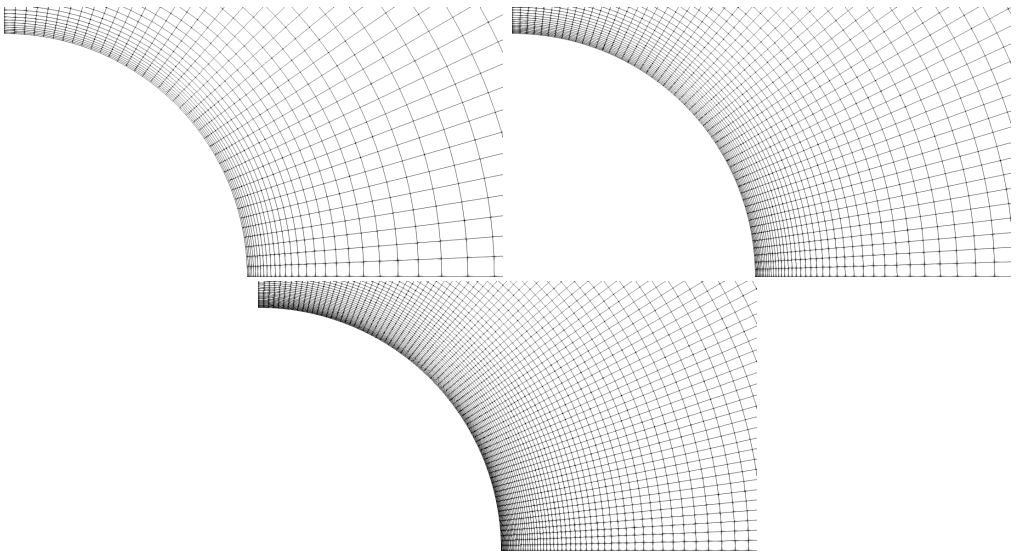

Figure 6.11: Circular cylinder at Re = 3900. Detail near the cylinder of the different mesh, coarse (top,left), medium (top,right) and fine (bottom) with 395 920, 1 088 958 and 3 110 200 elements, respectively

pect ratio in the whole region. In literature the most popular mesh types are C- and O-type, e.g. Lysenko et al. [106] with a resolution of $300 \times 300 \times 64$ ($5.7 \times 10^6$) elements. Only a few simulations were carried out using structured and unstructured H-type meshes, e.g. Parnaudeau et al. [105] with a maximum resolution of $961 \times 960 \times 48$ ($45 \times 10^6$). Several researchers [105] pointed out that the aspect ratio in the crosswise $L_y$ and spanwise $L_z$ direction may be considered as the most important parameters in the construction of the mesh, because they have significant impact on the main flow parameters, e.g. the recirculation bubble length. In the most cases the following values are used: $L_y = 15D - 70D$ and $L_z = \pi D$. Wissink and Rodi [104] used O-type meshes with a maximum resolution of $1206 \times 406 \times 1024$ ($501 \times 10^6$) and varied the spanwise dimension from $2D$ to $8D$ describing that only marginally this dimension affects the time-averaged statistics in the cylinder wake.

The characteristic integration time for sampling average data has been performed over about 200 shedding periods, with a time-step $\Delta t = 10^{-3} D/u_\infty$ in order to guarantee a Courant number of 0.1. The initial and boundary conditions of all the simulations are the free-stream pressure and velocity $u_\infty$, based on the cylinder diameter and the Reynolds number, and

$$k_{=} \frac{3}{2}(u_\infty I)^2, \qquad \omega = \frac{k}{\nu}\left(\frac{\mu_t}{\mu}\right)^{-1}, \tag{6.1}$$

where $I = 0\%$ (laminar flow) is the free-stream turbulent intensity and $\mu_t/\mu$

is the ratio between the turbulent viscosity and the dynamic viscosity. Here $\nu_t = 3.15 \times 10^{-6}$, $k = 0\frac{m^2}{s^2}$ and $\omega = 0\frac{1}{s}$.

Figure 6.12 shows the comparison between the different meshes, in terms of the distribution of the time- and spanwise-averaged pressure coefficient $c_p$ and normalized wall vorticity magnitude $\Omega/2Re^{0.5}$ on the cylinder, while Figs. 6.13 and 6.14 compare the time- and spanwise-averaged streamwise $u_x/u_\infty$ and crosswise $u_y/u_\infty$ velocity profiles and streamwise $u'_x u'_x/u^2_\infty$ and cross-wise $u'_y u'_y/u^2_\infty$ velocity fluctuations profiles at different locations $x/D = \{1.06, 1.54, 2.02\}$ in the wake of the cylinder. Figure 6.15 compares the time- and spanwise-averaged streamwise velocity $u_x/u_\infty$ and the streamwise velocity fluctuations $u'_x u'_x/u^2_\infty$ profiles along the centreline in the wake of the cylinder. The results by Parnaudeau et al. [105] are characterized by the presence of a U-shaped $x$-component velocity profile while Lourenco and Shih [102] show a V-shaped profile. High-fidelity simulations confirm that a U-shaped $x$-component velocity profile seems to be correct. In fact, it reflects the presence of two-virtually two-dimensional-free shear layers at $y/D \sim \pm 0.5$ [106], corresponding to the two detached non-turbulent boundary layers from the top and bottom of the cylinder. The V-shaped profiles can be considered an ill-resolved shear layers due to an earlier transition, loss of coherence and more fluctuations penetrating the region behind the cylinder. In fact, in Fig. 6.13, solution predicted with X-LES and the coarse mesh describes a V-shaped $x$-component velocity profile, while the medium and fine meshes guarantee enough accuracy to switch to the U-shaped solution. Figure 6.16 shows the isosurfaces of the Q-criterion coloured with the vorticity magnitude contours with coarse and fine mesh, where the Kelvin-Helmhotz instabilities with the breaks-up of the shear layer occurs more upstream with the coarse mesh. Figure 6.13 shows also the influence of the SGS model of LES on the results. As pointed by Lysenko et al. [106] the conventional Smagorinsky model leads to a V-shape, while the dynamic $k$-equation model leads to a U-shape; the different accuracy can be ascribed to the different viscosity introduced by the SGS model. In the streamwise velocity fluctuations the magnitude of the peaks is systematically overestimated for the coarser meshes. In fact, for the coarse mesh higher values of $u'_x u'_x/u^2_\infty$ in each location respect to the reference data are observed. This is probably a consequence of the under-prediction of the recirculation zone length. All the simulations are able to predict the two peaks of the streamwise velocity fluctuations but only the fine mesh is also able to predict the peaks magnitude. In general an underestimation of the Reynolds stresses $u'_x u'_x/u^2_\infty$ and $u'_y u'_y/u^2_\infty$ means that the shear layer break-up and the laminar-turbulent transition occur more downstream of the cylinder, which leads to a longer recirculation bubble, and viceversa.

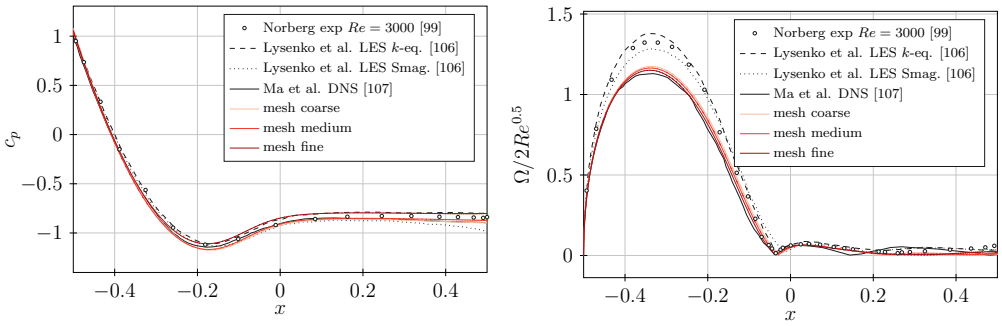


Figure 6.12: Circular cylinder at Re = 3900. Time- and spanwise-averaged pressure coefficient $c_p$ (left) and normalized vorticity magnitude $\Omega/2Re^{0.5}$ (right) distribution on the cylinder with different meshes, DX-LES. $x = -0.5$ is the stagnation point

Table 6.1 compares the results of all the simulations, with the the reference data expressed in terms of the root-mean-square lift coefficient $c_{L\,rms}$, the time-averaged drag coefficient $c_D$, the Strouhal number $St$, the time-averaged separation angles $\theta_{sep}$, the time-averaged base suction coefficient $-c_{pb}$, the time-averaged peak of the streamwise velocity in the wake $-u_{min}/u_{\inf}$ and the time-averaged recirculation zone length $L_r/D$. The time-averaged separation angle $\theta_{sep}$ is calculated from the condition of vanishing wall-shear stress in the time-averaged field around the cylinder, while the time-averaged base suction coefficient $-c_{pb}$ as the time-averaged pressure coefficient on the cylinder's surface at $\theta = 180°$. The time-averaged suction coefficient is strongly related to the drag coefficient. The time-averaged recirculation length $L_r/D$ corresponds to the distance between the surface of the cylinder and the sign change of the time-averaged streamwise velocity profile along the centreline in the wake of the cylinder (Figs. 6.15 and 6.21). The Strouhal number is defined as $St = f_{shedding}D/u_\infty$, where $f_{shedding}$ is the frequency of the vortex shedding instability. About $c_{L\,rms}$ Norberg [99] describes a comprehensive analysis, from the experimental point of view, of the dispersion of the values. In particular for Re $= \{3000 - 5000\}$ the $c_{L\,rms}$ varies from 0.03 to 0.1. As pointed out by Lysenko [106], higher viscosity, due to a coarser mesh, causes an early laminar-turbulent transition and, as a consequence, a shorter recirculation bubble, and a higher amplitude of the lift and the drag coefficients. In fact, $c_{L\,rms} = \{0.18,\ 0.12,\ 0.13\}$ and $L_r/D = \{1.34,\ 1.58,\ 1.66\}$ with coarse, medium and fine mesh. This behaviour on coarser meshes can be found also in the results of Lysenko et al. [106] with Smagorinsky SGS model. The time-averaged length of the recirculation bubble $L_r/D$ prediction can be considered as the most important parameter for the agreement

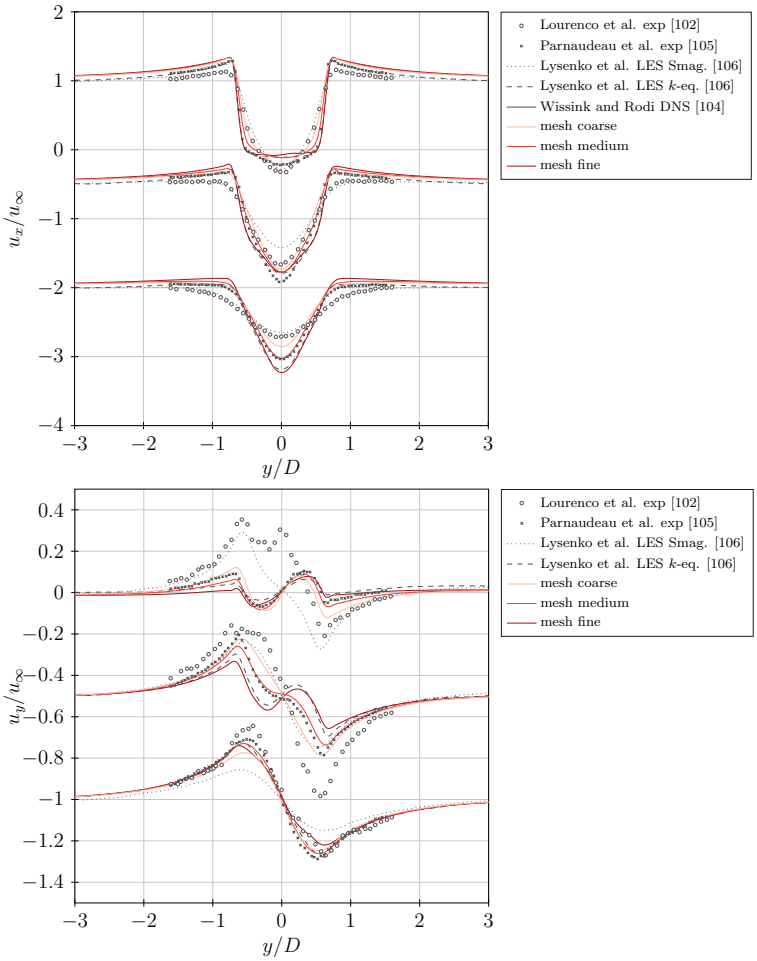


Figure 6.13: Circular cylinder at Re = 3900. Time- and spanwise-averaged streamwise $u_x/u_\infty$ (top) and crosswise $u_y/u_\infty$ (bottom) velocity profiles at different locations $x/D = \{1.06, 1.54, 2.02\}$ in the wake of the cylinder with different meshes, DX-LES

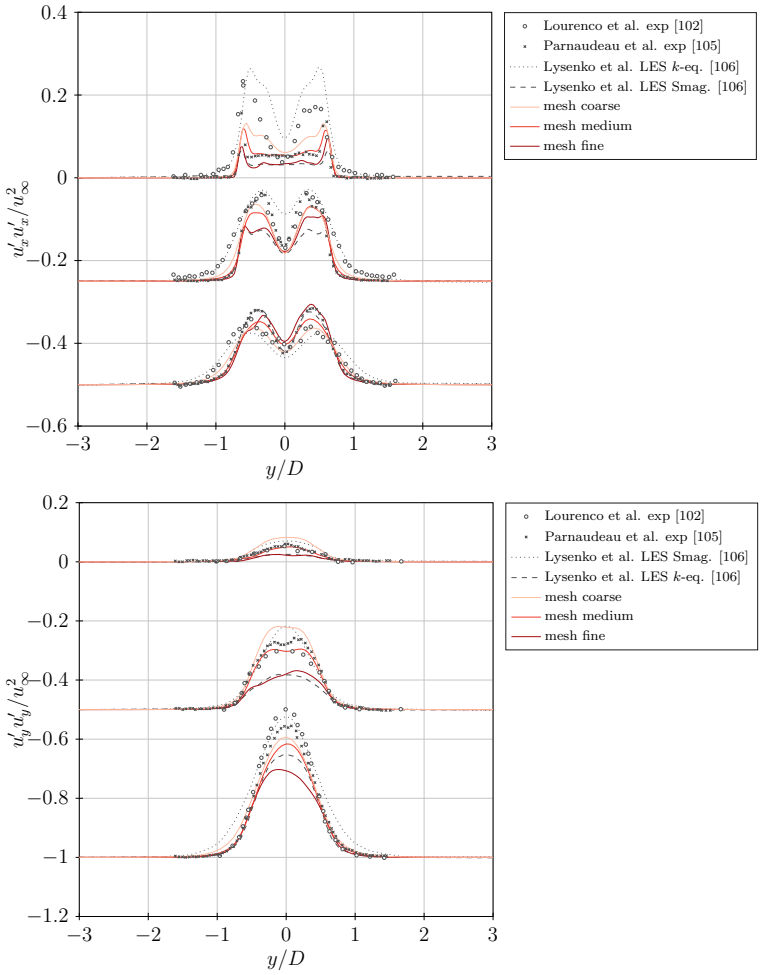


Figure 6.14: Circular cylinder at $Re = 3900$. Time- and spanwise-averaged streamwise $u'_x u'_x / u^2_\infty$ (top) and crosswise $u'_y u'_y / u^2_\infty$ (bottom) velocity fluctuations profiles at different locations $x/D = \{1.06, 1.54, 2.02\}$ in the wake of the cylinder with different meshes, DX-LES

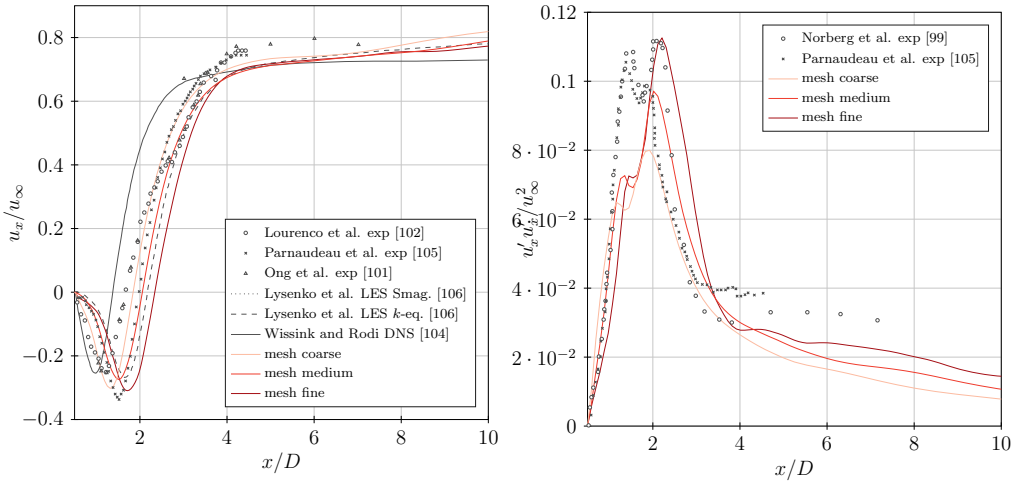


Figure 6.15: Circular cylinder at $Re = 3900$. Time- and spanwise-averaged streamwise velocity $u_x/u_\infty$ (left) and streamwise velocity fluctuations $u'_x u'_x/u^2_\infty$ (right) profiles along the centreline in the wake of the cylinder with different meshes, DX-LES

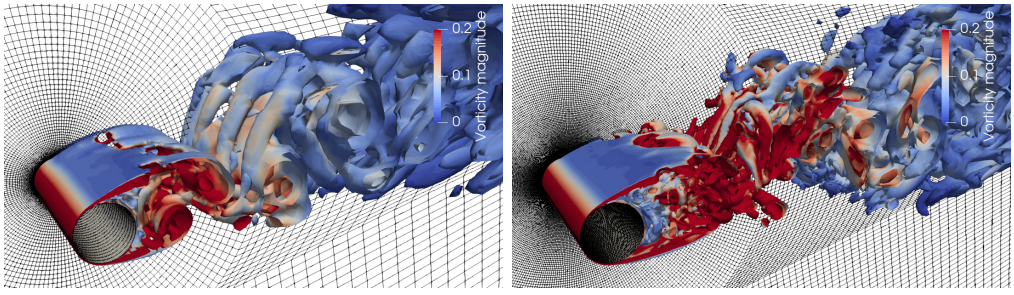


Figure 6.16: Circular cylinder at Re = 3 900. Isosurfaces of Q-criterion coloured with the vorticity magnitude contours with coarse (left) and fine (right) mesh, X-LES

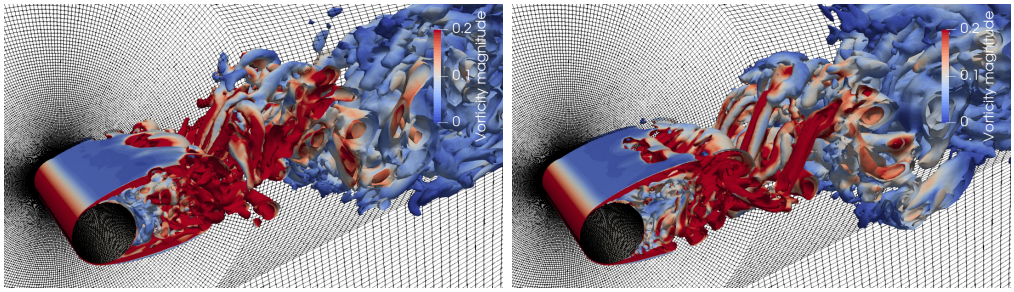


Figure 6.17: Circular cylinder at Re = 3 900. Isosurfaces of Q-criterion coloured with the vorticity magnitude contours with X-LES (left) and DX-LES (right), fine mesh

between numerical and experimental results. In fact, it is due to the position of the shear-layer break-up and the transition. DX-LES with $L_r/D = 1.66$ shows a good agreement with reference results, in particular DX-LES is in very good agreement with the LES $k$-eq by Lysenko et al. [106] while X-LES slightly overestimates the result. In fact, X-LES introduces a lower eddy viscosity due to MSD in comparison with DX-LES and overestimates of recirculation bubble and the amplitude of the lift and the drag coefficients. Figure 6.17 shows the isosurfaces of the Q-criterion coloured with the vorticity magnitude contours obtained with X-LES and DX-LES and using the fine mesh, where the Kelvin-Helmhotz instabilities with the break-up of the shear layer occur more downstream with X-LES.

Figure 6.18 shows the distribution of the time- and spanwise-averaged pressure coefficient $c_p$ and normalized wall vorticity magnitude $\Omega/2Re^{0.5}$ on the cylinder with X-LES and DX-LES. Figures 6.19 and 6.20 shows the time- and spanwise-averaged streamwise $u_x/u_\infty$ and crosswise $u_y/u_\infty$ velocity profiles and streamwise $u'_x u'_x/u^2_\infty$ and crosswise $u'_y u'_y/u^2_\infty$ velocity fluctuations profiles at different locations $x/D = \{1.06, 1.54, 2.02\}$ in the wake of the cylinder with X-LES and DX-LES. Finally, Figure 6.21 shows the time- and spanwise-averaged streamwise velocity $u_x/u_\infty$ and the streamwise velocity fluctuations $u'_x u'_x/u^2_\infty$ profiles along the centreline in the wake of the cylinder with X-LES and DX-LES. Both the models shows similar velocity profiles, in agreement with the reference, while X-LES slightly underestimates the peaks magnitude of the $u'_x u'_x/u^2_\infty$ profile. Figure 6.22 shows the time-averaged velocity and velocity fluctuation contours near the cylinder with both the models, where the extent of the recirculation bubble is slightly shorter with DX-LES.

Table 6.1: Circular cylinder at $Re = 3900$. Comparison of the root-mean-square lift coefficient $c_{L\,rms}$, the time-averaged drag coefficient $c_D$, the Strouhal number $St$, the time-averaged separation angles $\theta_{sep}$, the time-averaged base suction coefficient $-c_{p\,b}$, the time-averaged peak of the streamwise velocity in the wake $-u_{min}/u_{\inf}$ and the time-averaged recirculation zone length $L_r/D$, between literature and results for the different spatial accuracy and models

| | $c_D$ | $c_{L\,rms}$ | St | $-c_{p\,b}$ | $L_r/D$ | $-u_{min}/u_\infty$ | $\theta_{sep}$ |
|---|---|---|---|---|---|---|---|
| Lourenco and Shih exp. [102] | 0.99 | - | 0.22 | - | 1.19 | 0.24 | 86° |
| Norberg exp. [99] | 0.98 | 0.04-0.15 | - | 0.9 | - | - | - |
| Ong and Wallace exp. [101] | - | - | 0.21 | - | - | - | - |
| Ma et al DNS [107] | 0.84 | - | 0.22 | - | 1.59 | - | - |
| Parnaudeau et al. exp. [105] | - | - | 0.21 | - | 1.51 | 0.34 | - |
| Parnaudeau et al. LES [105] | - | - | 0.21 | - | 1.56 | 0.28 | - |
| Wissink and Rodi DNS [104] | - | - | 0.22 | - | 1.588 | 0.33 | 87° |
| Breuer LES [108] | 1.04 | - | 0.2 | 0.94 | 1.35 | 0.37 | 88° |
| Lysenko LES Smag. [106] | 1.18 | 0.44 | 0.19 | 0.8 | 0.9 | 0.26 | 89° |
| Lysenko LES $k$-eq. [106] | 0.97 | 0.09 | 0.209 | 0.91 | 1.67 | 0.27 | 88° |
| coarse mesh | 1.05 | 0.18 | 0.21 | 0.90 | 1.34 | 0.30 | 88.51 |
| medium mesh | 1.00 | 0.12 | 0.22 | 0.87 | 1.58 | 0.27 | 88.45 |
| fine mesh | 1.00 | 0.13 | 0.21 | 0.84 | 1.66 | 0.28 | 86.45 |

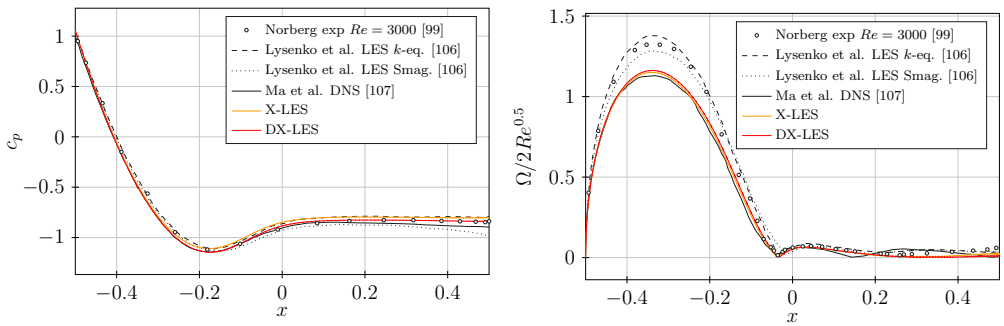


Figure 6.18: Circular cylinder at Re = 3900. Time- and spanwise-averaged pressure coefficient $c_p$ (left) and normalized vorticity magnitude $\Omega/2Re^{0.5}$ (right) distribution on the cylinder, fine mesh. $x = -0.5$ is the stagnation point

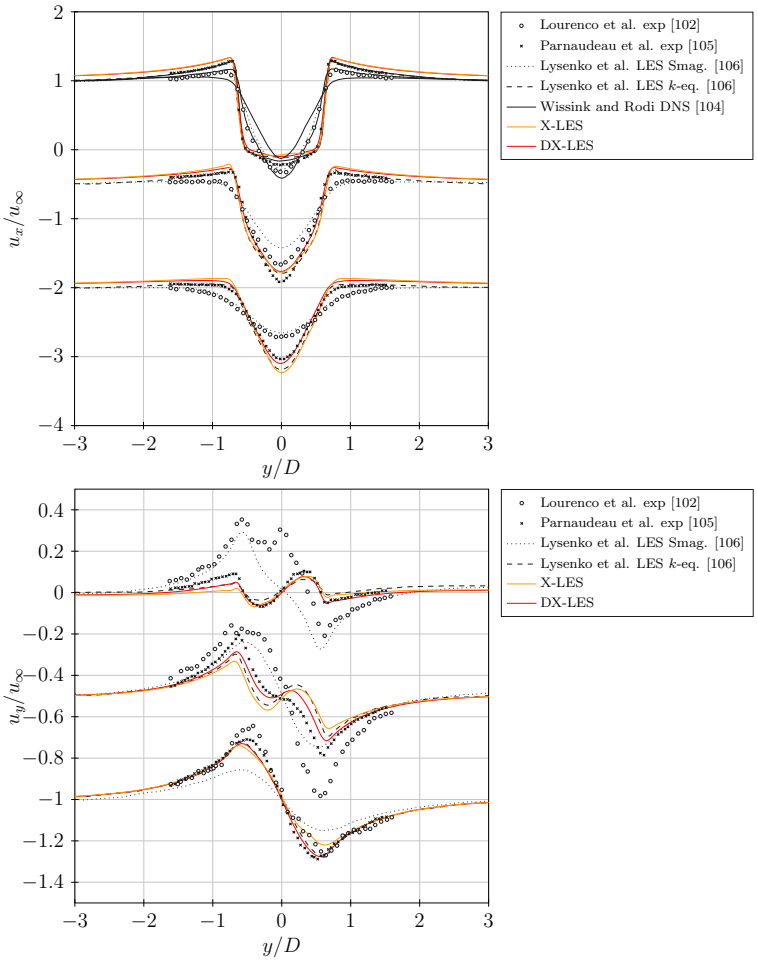


Figure 6.19: Circular cylinder at Re = 3900. Time- and spanwise-averaged streamwise $u_x/u_\infty$ (top) and crosswise $u_y/u_\infty$ (bottom) velocity profiles at different locations $x/D = \{1.06, 1.54, 2.02\}$ in the wake of the cylinder, fine mesh

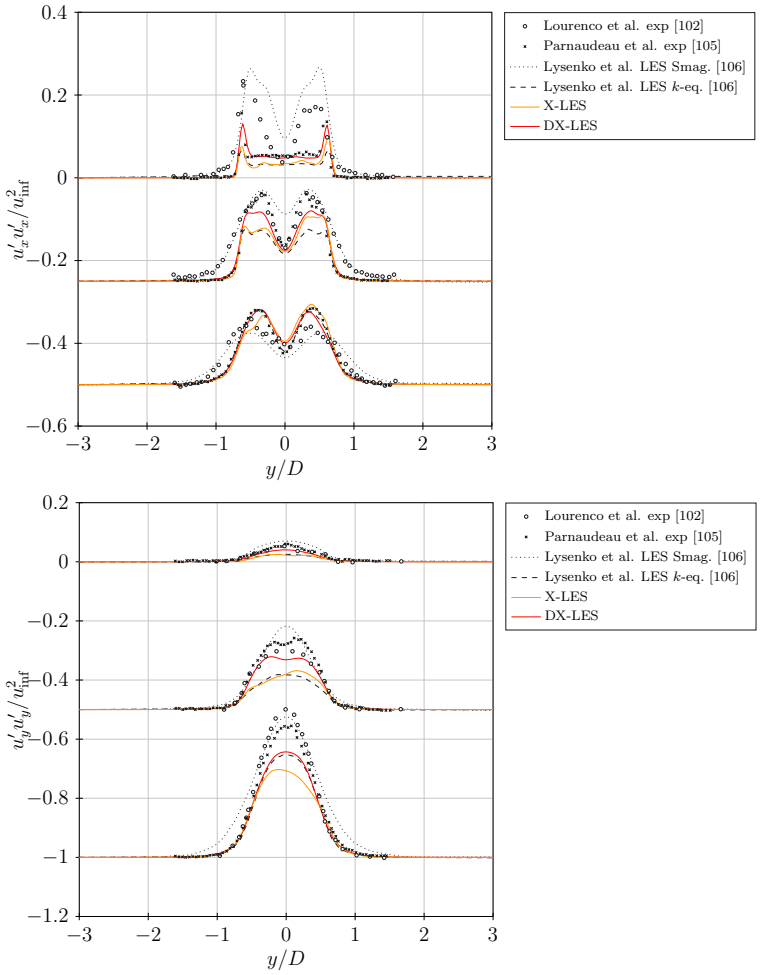


Figure 6.20: Circular cylinder at Re = 3900. Time- and spanwise-averaged streamwise $u'_x u'_x / u^2_\infty$ (top) and crosswise $u'_y u'_y / u^2_\infty$ (bottom) velocity fluctuations profiles at different locations $x/D = \{1.06, 1.54, 2.02\}$ in the wake of the cylinder, fine mesh

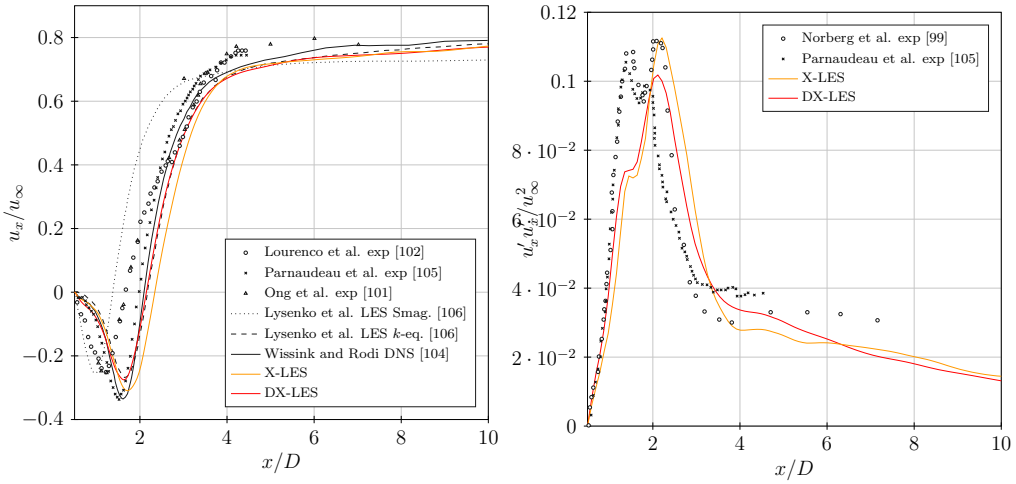


Figure 6.21: Circular cylinder at Re = 3900. Time- and spanwise-averaged streamwise velocity $u_x/u_\infty$ (left) and streamwise velocity fluctuations $u'_x u'_x/u^2_\infty$ (right) profiles along the centreline in the wake of the cylinder, fine mesh

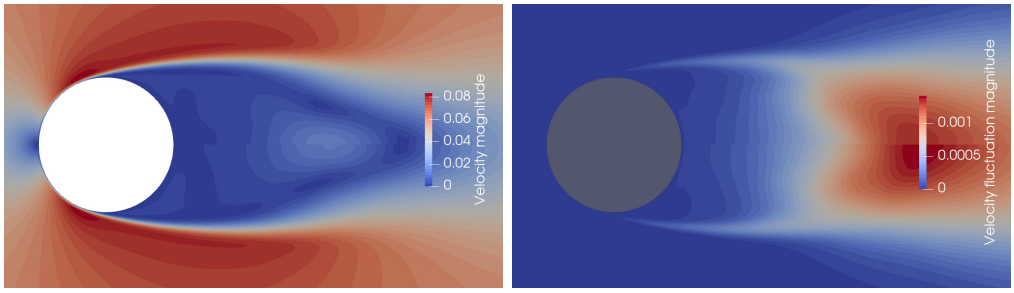


Figure 6.22: Circular cylinder at Re = 3 900. Time-averaged velocity (left) and velocity fluctuation (right) contours near the cylinder with X-LES (up) and DX-LES (bottom), fine mesh

## 6.4 Turbulent flow around a circular cylinder at $\mathrm{Re} = 140\,000$

The turbulent flow around a circular cylinder at high sub-critical Reynolds number $\mathrm{Re} = 140\,000$, based on the cylinder diameter and free-stream conditions, has been investigated. The flow is near the critical Reynolds number and for this reason is a challenging problem of fluid mechanics, both from an experimental and a numerical point of view. As in the previous case of the turbulent flow around a circular cylinder at Reynolds number $\mathrm{Re} = 3\,900$, the boundary layer is still laminar until the separation, but the laminar-turbulent transition of the shear layer takes place very shortly after separation, with the creation of Kelvin-Helmholtz instabilities, the break-up of the shear layer and an asymmetric Von Kármán vortex shedding. For slightly higher values of the Reynolds number, i.e. $\mathrm{Re} = 200\,000 - 300\,000$, the (attached) boundary layer becomes turbulent, the Strouhal number increases and the well-known drag crisis is observed.

The accuracy of any numerical model is dependent on the ability to predict the location of the separation and the laminar-turbulent transition. In fact, the location of these phenomena is determined by the magnitude of the Reynolds number and near the critical values separation and transition happen very close one each other. In this case, the well recognized limitations of standard turbulence models that are used in hybrid RANS-LES models to deal with transition onset cause the premature laminar-turbulent transition, which happens in the (attached) boundary layer [109]. Shur et al. in [110] introduced the trip-less turbulent separation (TS) case, which is compared with the laminar separation (LS) case. In this case reference data are those obtained at higher Reynolds number, i.e. $\mathrm{Re} > 200\,000$ [111, 112], in order to have a comparison with acceptable error margins.

Hybrid models can suffer the limitations of turbulence models, with the premature occurrence the laminar-turbulent transition due to RANS in the near-wall region, in contrast to a LES-like behaviour, characterized by a sub-critical flow regime and laminar separation. All the hybrid turbulence models experienced similar challenges, but MSD can lead to an underestimation of the eddy viscosity and turbulence intensity with a laminar separation.

As shown in literature, at these high-Reynolds numbers measurements are very sensitive to free-stream turbulent fluctuations, surface roughness and in general boundary conditions and, as a consequence, the scattering of the measurements is very high. Experiments of Cantwell and Coles [113], Norberg [113], Achenbach ($\mathrm{Re} = 100\,000$) [112] are taken as reference for LS, while Roshko [111] and Achenbach ($\mathrm{Re} = 210\,000$) [112] are taken as

reference for TS.

A limited number of high-fidelity LES, implicit LES, and hybrid RANS-LES simulations was carried out during the last two decades. Frohlich et al. [114, 115], Karabelas [116] and Breuer [108] performed LES with different subgrid scale models and investigated on the influence of the parameter of the subgrid scale model on the results. Hybrid RANS-LES simulations have been performed by Travin et al. [117] (SA-DES), Islam and Thornber [118] (RANS-ILES), and Zheng et al. [119] (SST-DES). Travin et al. [117] spotlight the different behaviour of the turbulence model in the near-wall region with the distinction between LS and TS. The Spalart-Allmaras turbulence model allows to predict both laminar, by imposing a zero eddy viscosity inflow until separation, and turbulent separation. The results used for comparison are LS8 and TS5.

Three different computational meshes have been used with the same rectangular domain (H-type), but different number of elements in each direction, in order to assess a convergence of the results with DX-LES. The meshes have 624 624 (coarse), 1 827 840 (medium) and 4 996 992 (fine) elements. Figure 6.23 shows a detail near the cylinder of the meshes. The cylinder is discretized with 170, 255 and 340 elements along circumferential direction, and the spanwise direction with 33, 48 and 66 elements. The mesh has a spanwise extension $L_z = 2D$, and a streamwise extension $L_x = 40D$, $10D$ upstream and $30D$ downstream, and a crosswise extension $L_y = 20D$ with a periodic condition. It can be seen that the elements of the meshes near the cylinder, in the O-type part of the mesh, have been only stretched in the radial direction to avoid the occurrence of numerical inaccuracies due to unfavorable mesh aspect ratios. In fact, in the whole region the elements have a quasi-cubic aspect ratio. The resolution of the mesh used by Travin et al. [117] is $150 \times 109 \times 52$ (850 000 elements), by Islam and Thornber [118] is $136 \times 160 \times 30$, $171 \times 160 \times 30$ and $211 \times 160 \times 30$ (653 000, 821 000 and $1.01 \times 10^6$ elements), and by Zheng et al. [119] is $171 \times 136 \times 30$ and $211 \times 136 \times 30$ (697 680 and 860 880 elements). Numerical results from literature suggest that the influence of the spanwise length on the wake structure is much greater at lower Reynolds numbers and based on the investigation of Kravchenko and Moin [103] at $\mathrm{Re} = 3\,900$ the differences in the statistics in the near wake were insignificant for $\pi D$ and $\pi/2D$.

The characteristic integration time for sampling average data has been performed over about 100 shedding periods, with a time-step $\Delta t = 10^{-3} D/u_\infty$ in order to guarantee a Courant number of 0.1. The boundary conditions for all the simulations are the free-stream pressure and velocity $u_\infty$, the turbulent

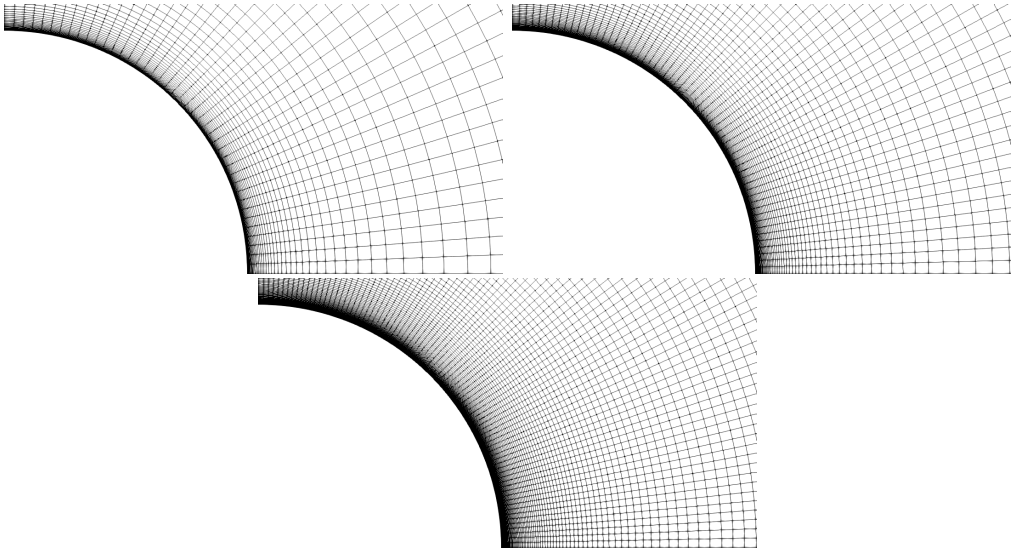

Figure 6.23: Circular cylinder Re = 140 000. Detail near the cylinder of the different mesh, coarse (top,left), medium (top,right) and fine (bottom) with 624 624, 1 827 840 and 4 996 992 elements

kinetic energy and specific dissipation rate

$$k_{=}\frac{3}{2}(u_\infty I)^2, \qquad \omega = \frac{k}{\nu}\left(\frac{\mu_t}{\mu}\right)^{-1}, \tag{6.2}$$

where $I = 0\%$ (laminar flow) is the free-stream turbulent intensity and $\mu_t/\mu$ is the ratio between the turbulent viscosity and the dynamic viscosity ($\nu_t = 3.15 \times 10^{-6}$, $k = 0\frac{m^2}{s^2}$ and $\omega = 0\frac{1}{s}$). Low Reynolds version of turbulence model has been used.

Table 6.2 compares the results for X-LES and DX-LES, with the references in terms of the root-mean-square lift coefficient $c_{L\,rms}$, the time-averaged drag coefficient $c_D$, the Strouhal number $St$, the time-averaged separation angles $\theta_{sep}$, the time-averaged base suction coefficient $-c_{p\,b}$, the time-averaged peak of the streamwise velocity in the wake $-u_{min}/u_{\inf}$ and the time-averaged recirculation zone length $L_r/D$. Both experimental and numerical studies in literature demonstrated that there was a non-linear relationship between the separation angle, the recirculation zone length, and the Reynolds number. Experimental results confirm the presence of a laminar boundary layer and turbulent flow in the shear layers, while most of the computational approaches based on turbulence models over-predicted the angle of separation, with a separations point more downstream. In fact, if the laminar to turbulent transition occurs in the (attached) boundary layer, the

Table 6.2: Circular cylinder at Re = 140 000. Comparison of the root-mean-square lift coefficient $c_{L\,rms}$, the time-averaged drag coefficient $c_D$, the Strouhal number $St$, the time-averaged separation angles $\theta_{sep}$, the time-averaged base suction coefficient $-c_{p\,b}$, the time-averaged peak of the streamwise velocity in the wake $-u_{min}/u_{\inf}$ and the time-averaged recirculation zone length $L_r/D$, between literature and results for the different spatial accuracy and models

| | $c_D$ | $c_{L\,rms}$ | St | $-c_{p\,b}$ | $L_r/D$ | $-u_{min}/u_\infty$ | $\theta_{sep}$ |
|---|---|---|---|---|---|---|---|
| Cantwell and Coles exp. [113] | 1.237 | - | 0.179 | 1.21 | 0.44 | - | - |
| Roshko exp. [111] | 0.7 | - | 0.27 | 0.8 | - | - | - |
| Islam and Thornber RANS-ILES [118] | 0.869 | - | 0.271 | 0.767 | 1.26 | 0.367 | 96.38° |
| Zheng et al. SST-DES [119] | 0.84 | - | 0.247 | 0.93 | 0.81 | 0.311 | 93.9 ° |
| Frohlich et al.LES [115] | 1.147 | - | 0.217 | 1.33 | 0.42 | 0.145 | 79° |
| Travin et al. SA-DES LS8 [117] | 1.08 | 0.29 | 0.21 | 1.04 | 1.1 | 0.261 | 77° |
| Travin et al. SA-DES TS5 [117] | 0.65 | 0.06 | 0.28 | 0.70 | 1.4 | - | 93° |
| X-LES | 0.95 | 0.14 | 0.21 | 0.60 | 1.61 | 0.28 | 83.11° |
| DX-LES | 0.66 | 0.042 | 0.28 | 0.69 | 1.43 | 0.33 | 88.93° |

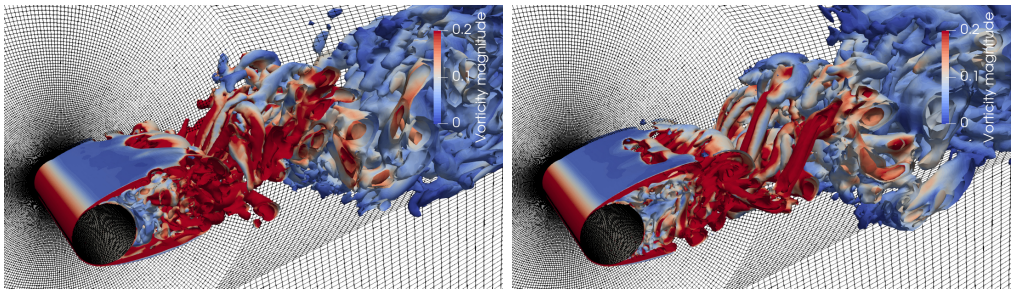


Figure 6.24: Circular cylinder at Re = 140 000. Isosurfaces of Q-criterion coloured with the vorticity magnitude contours with X-LES (left) and DX-LES (right), fine mesh

higher diffusivity of the turbulent regime delays the separation. Figure 6.24 shows the isosurfaces of the Q-criterion coloured with the vorticity magnitude contours with X-LES and DX-LES and fine mesh, where the separation of the boundary layer occur more upstream with X-LES. The time-averaged separation angles $\theta_{sep}$ is 83.11° for X-LES and 88.93° for DX-LES: a separation point more upstream means a longer recirculation bubble, and a higher amplitude of the lift and the drag coefficients.

Figure 6.25 shows the distribution of the time- and spanwise-averaged pressure $c_p$ and skin friction $c_f$ coefficient on the cylinder with X-LES and DX-LES. Figure 6.26 shows the time- and spanwise-averaged streamwise velocity $u_x/u_\infty$ and the streamwise velocity fluctuations $u'_x u'_x/u^2_\infty$ profiles at $x/D = 1$ in the wake of the cylinder with X-LES and DX-LES. Finally Figure 6.27 shows the time- and spanwise-averaged streamwise velocity $u_x/u_\infty$

and the streamwise velocity fluctuations $u'_x u'_x / u^2_\infty$ profiles along the centre-line in the wake of the cylinder with X-LES and DX-LES.DX-LES is in good agreement with the results presented by Islam and Thornber [118], Zheng et al. [119] and Travin et al. (SA-DES TS5 [117]). The results predicted by X-LES seems closer to the experiments. However, this behaviour is motivated by MSD phenomenon due to the presence of the LES in the boundary layer.

In fact, X-LES introduces a lower turbulent intensity, in comparison with DX-LES, that means the break-down to high intensity turbulence with the laminar to turbulent transition more downstream in the separated shear layer, while in DX-LES occurs in the attached boundary layer.

The free-stream turbulence and the boundary layer turbulence upstream of the point of separation are important factors to understand the flow dynamics around the cylinder. Therefore, a closer analysis of the near-wall turbulent kinetic energy reveals a potential source of the discrepancies between X-LES and the DX-LES. Figure 6.28 shows the instantaneous turbulent kinetic energy $k$ and the turbulence intensity $Tu = \sqrt{2/3k}/u$ contours near the cylinder with both the methods, where X-LES underestimates the turbulence intensity in the boundary. Figure 6.29 shows the time-averaged velocity and velocity fluctuation contours near the cylinder: both the models show similar velocity profiles, in a better agreement with the reference respect to the hybrid results by Islam and Thornber [118] and Zheng et al. [119], while underestimate the peaks magnitude of the $u'_x u'_x / u^2_\infty$ profile. Similar to the streamwise velocity variation, the Reynolds stresses in the experiment had a wider profile due to more diffused shear layers around the sides of the cylinder.

## 6.5 Remarks

The new DX-LES hybrid model has been validated on three test cases. In general, each test case proves that the proposed delayed version allows to avoid the MSD phenomenon and improve the near wall behaviour with respect to the X-LES model:

1. in the first two test cases, the turbulent channel flow at Re = 2000 and the backward facing step, the improvement of the near-wall behaviour with the proposed delayed model, in comparison with X-LES, is evident. In particular, on the backward facing step the skin friction coefficient distribution and the eddy viscosity contours demonstrate the better behaviour of DX-LES. In the X-LES model the switch to LES happens in the boundary layer and the MSD phenomenon appears. Moreover, benefits in using the blend filter $\Delta_{mix}$ are shown.

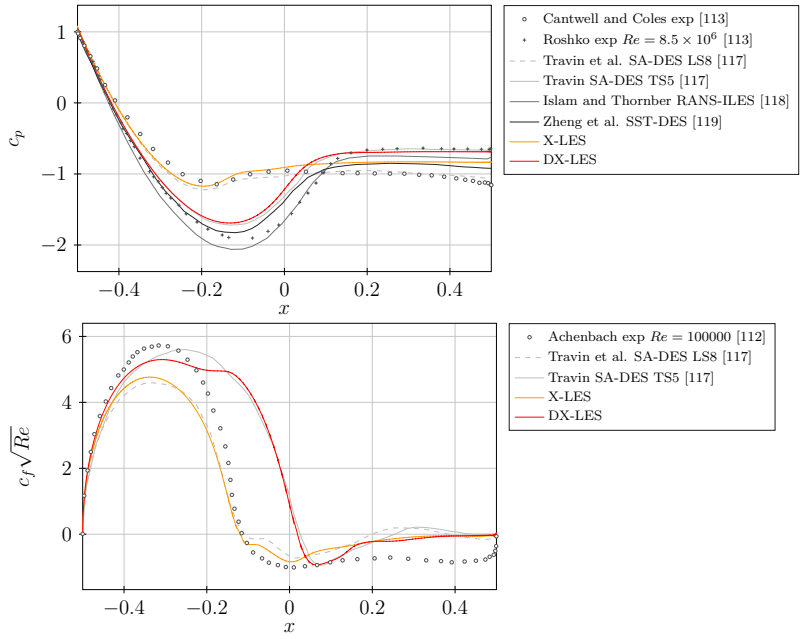


Figure 6.25: Circular cylinder at Re = 140 000. Time- and spanwise-averaged pressure $c_p$ (top) and skin friction $c_f$ (bottom) coefficient distribution on the cylinder, fine mesh. $x = -0.5$ is the stagnation point

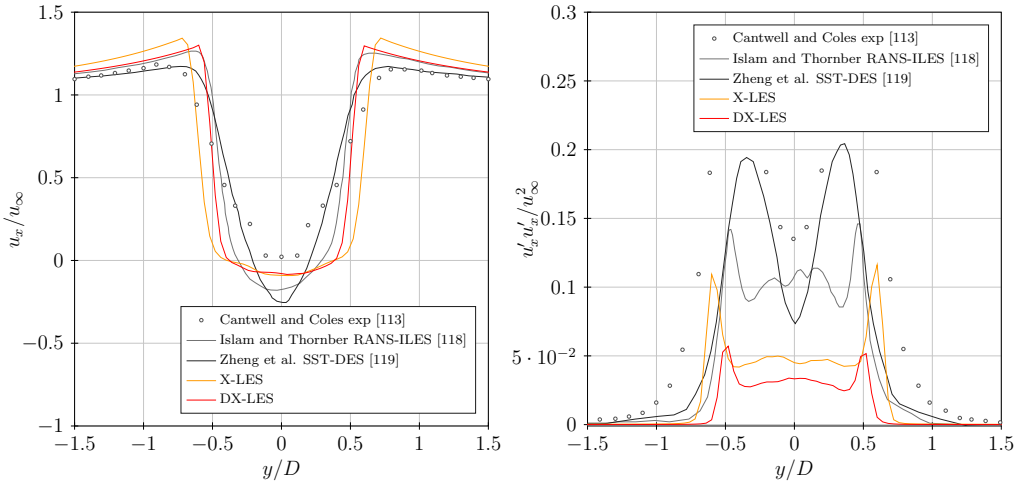


Figure 6.26: Circular cylinder at Re = 140 000. Time- and spanwise-averaged streamwise velocity $u_x/u_\infty$ (left) and velocity fluctuations $u'_x u'_x/u^2_\infty$ (right) at $x/D = 1$ in the wake of the cylinder, fine mesh

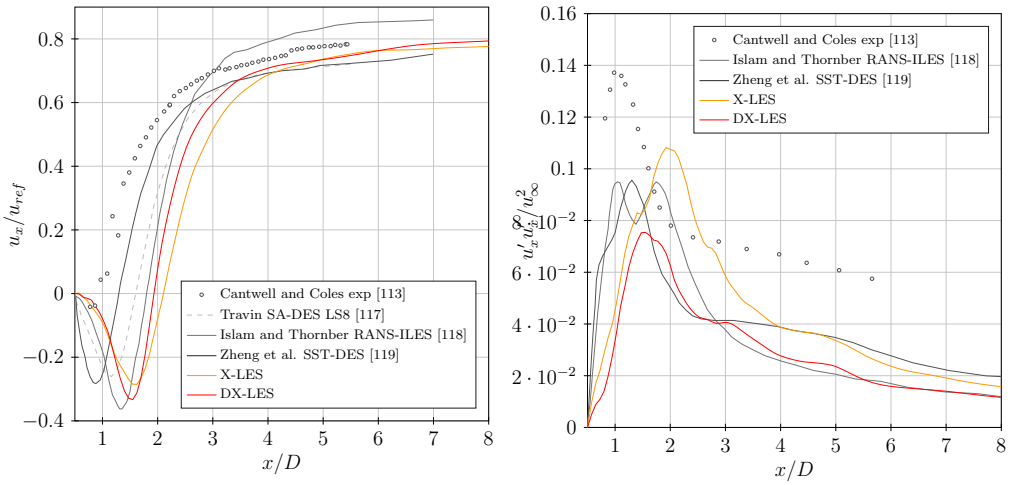


Figure 6.27: Circular cylinder at Re = 140 000. Time- and spanwise- averaged streamwise velocity $u_x/u_\infty$ (left) and streamwise velocity fluctuations $u'_x u'_x/u^2_\infty$ (right) along the centreline in the wake of the cylinder, fine mesh

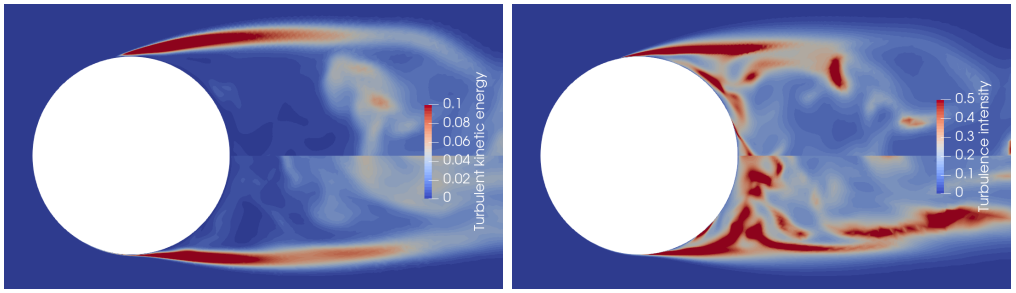


Figure 6.28: Circular cylinder at Re = 140 000. Instantaneous turbulent kinetic energy $k$ (left) and turbulence intensity $Tu = \sqrt{2/3k}/u$ (right) contours near the cylinder with X-LES (up) and DX-LES (bottom), fine mesh

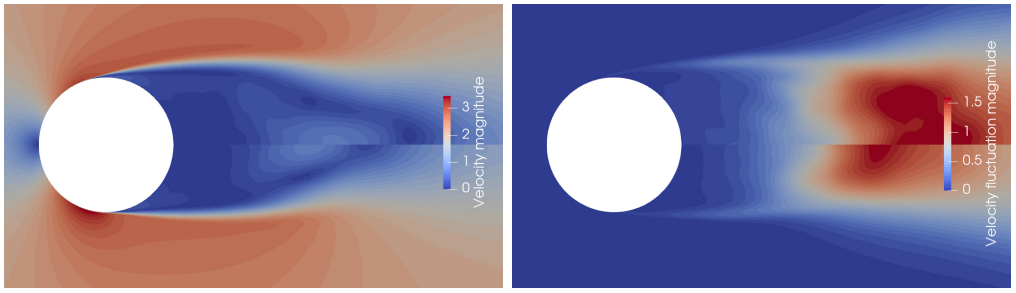


Figure 6.29: Circular cylinder at Re = 140 000. Time-averaged velocity (left) and velocity fluctuation (right) contours near the cylinder with X-LES (up) and DX-LES (bottom), fine mesh

2. In the circular cylinder at Re = 3900 the X-LES model slightly overestimates the recirculation bubble due to a lower eddy viscosity caused by the MSD, while the DX-LES model better predicts the velocity fluctuations, the time-averaged separation angle and the time-averaged length of the recirculation bubble.

3. In the circular cylinder at Re = 140 000 the laminar to turbulent transition of the shear layer takes place just after the separation and standard RANS model adopted in hybrid approach cannot predict correctly the transition onset. This behaviour is confirmed by the DX-LES model. The X-LES model seems to predict better only because the presence of the LES in the boundary layer decreases the eddy viscosity, preventing the onset of the transition.

# Chapter 7

# DX-LES simulation of the flow-field of a centrifugal pump

The aim of this Chapter is to present the results of the computation of the flow through a centrifugal pump impeller with the DX-LES model. Results are compared with experimental results, LES and RANS simulations from the literature.

## 7.1 Centrifugal pump

The flow field in a centrifugal pump is characterized by boundary layer separation, interaction between fixed and rotating components, vortex dynamics and, in general, by unsteady phenomena. In particular, at strongly off design conditions large separations lead to efficiency loss, vibrations and even to fatigue failure. Moreover, centrifugal pumps are often required to work in a wide range of conditions, not only in the best efficient point or design conditions.

Simulations with a steady-state approach are obviously not suitable to these problems, but also unsteady RANS are not able to capture the typical complex structures. LES models have been tested in industrial applications, like pumps, turbines or propellers [120, 121, 122, 15, 123, 13] and a good agreement with experimental results has always been reported. However, as seen in the introduction (see Chapter 4), LES for the simulation of complex flow in turbomachinary is not always affordable, due to the high Reynolds Number.

Hybrid models show a good accuracy in case of large separation and are less computational demanding than LES. In this chapter the capability of the implemented DX-LES hybrid model (see Chapter 5) is assessed for the

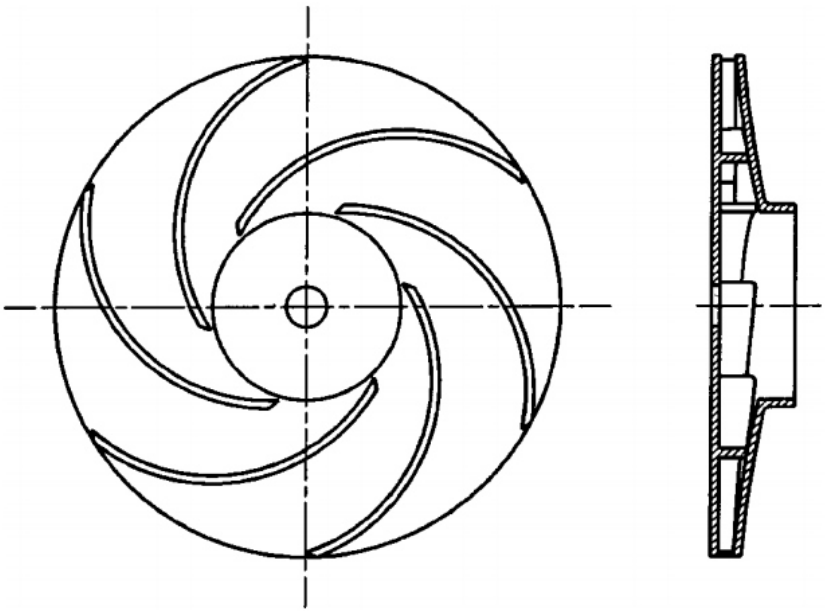

Figure 7.1: Impeller geometry [21]

simulation of the flow field through a centrifugal pump working at design and off design conditions.

The test case used for this analysis is the impeller of Pedersen et al. [21]. It is a shrouded, low specific-speed centrifugal impeller working with demineralized water at atmospheric conditions. The complete pump consists of a multi-stage pump for water distribution and pressure boosting used in industry and agriculture. The impeller is shown in Fig. 7.1, while the details of the geometry and the operative conditions are summarized in Tab. 7.1. PIV and LDV measurements of the velocity field are available. Byskov et al. [13] presented a related study, where RANS and LES results are shown and compared to the experimental data. Other studies have been conducted in the last years at design [124, 125] and off design conditions [126, 125] with LS approaches.

In the following the results of the DX-LES model are presented and compared to the RANS and LES simulations and to the experiments available in the literature.

## 7.2 CFD set-up

The set-up adopted for the simulation both in terms of mesh and CFD solver is presented in this section.

Table 7.1: Main geometric parameters and operative condition of the impeller pump [21]

| | | | |
|---|---|---|---|
| **Geometry** | | | |
| inlet diameter | $D_1$ | = 71.0 mm | |
| outlet diameter | $D_2$ | = 190.0 mm | |
| inlet height | $b_1$ | = 13.8 mm | |
| outlet height | $b_2$ | = 5.8 mm | |
| number of blades | $Z$ | = 6 | |
| blade thickness | $t$ | = 3.0 mm | |
| inlet angle | $\beta_1$ | = 19.7° | |
| outlet angle | $\beta_2$ | = 18.4° | |
| blade curvature radius | $R_b$ | = 70.0 mm | |
| | | | |
| **Operative conditions** | | Design | Off design |
| flow rate | $Q$ | 3.06 l/s | 0.76 l/s |
| flow rate ratio | | 1 | 0.25 |
| rotational speed | $n$ | 725 rpm | 725 rpm |
| specific speed | $N_s$ | 26.3 | 26.3 |
| Head | $H$ | 1.75 m | 2.4 m |
| Reynolds number | $Re$ | $1.4 \times 10^6$ | $1.4 \times 10^6$ |

Table 7.2: Characteristic of coarse, medium and fine grid

| | Mesh coarse | Mesh medium | Mesh fine |
|---|---|---|---|
| Number of cells [$\times 10^6$] | 5.5 | 8.6 | 11.3 |
| Max cell size [mm] | 1.5 | 0.8 | 0.4 |

The whole impeller is simulated and an extension of the inlet pipe is added to reduce possible disturbance due to the inflow at the blade leading edge. A diffuser is also added to avoid recirculation at the outflow. Three unstructured meshes with a structured boundary layer are generated for a grid independence study. The height of the first cell near the wall is of 0.015 mm, for all meshes, which guarantees an average $y^+$ less than 1 with a maximum of 5, and the expansion ratio at the wall is 1.2. Starting from a coarse grid of 5.5 millions of cells, the grid is refined up to 11.3 millions cells for the fine grid (see Table 7.2). The aim is to assess the resolution of mesh in the LES zone. In Figs. 7.2 and 7.3 details of the grids are shown.

The flow is assumed incompressible and isothermal. The DX-LES hybrid model implemented in the open-source CFD software OpenFOAM [55] is used to compute the flow field through the pump.

At the domain inlet the flow rate $Q$ is prescribed, while at the outflow a static pressure is fixed. The no-slip condition is applied to the blade walls, hub and shroud. The rotational speed $n$ (counterclockwise sense) is imposed at the impeller, while the diffuser is a stationary domain. The impeller outflow and the diffuser inflow are coupled with a sliding mesh approach (`arbitrary mesh interface`, AMI, in OpenFOAM). The values of the turbulent quantities at the inflow and at the walls are set as follows [83]:

$$\omega_{inflow} = 5\frac{U_{inflow}}{D_2}, \qquad k_{inflow} = 10^{-3}\frac{U_{inflow}}{\mathrm{Re}},$$
$$\omega_{wall} = 10\frac{6\nu}{0.075(\Delta d_1)^2}, \qquad k_{wall} = 0,$$

where $\Delta d_1$ is the height of the first cell at the wall. A steady-state solution with the Multiple Reference Frame (MRF) approach is used to initialize the unsteady simulation. The real movement of the mesh is taken into account considering the Navier-Stokes equations in the relative reference frame and adding a source term in the momentum equation. The interface between the stationary and rotating region is treated with a frozen rotor approach.

The solver `pimpleFoam` is used. The physical time-step is set to $1.5\times10^{-5}$ for the design condition and to $2.3\times10^{-5}$ for the off design condition, ensuring a maximum CFL of 5 and an average value less than 0.1. The time-average

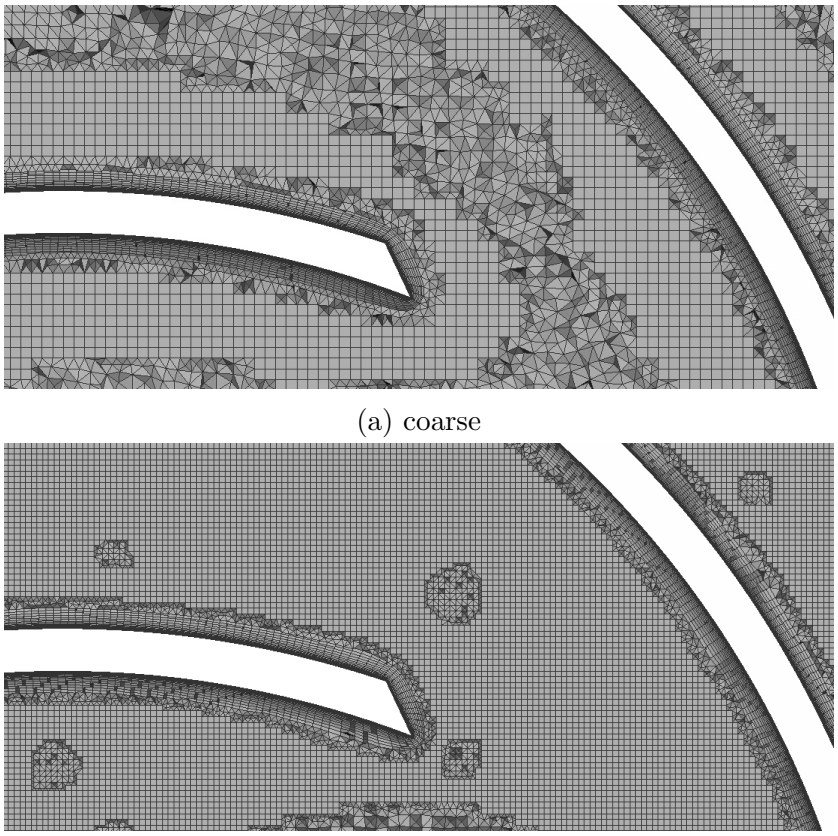

(a) coarse

(b) fine

Figure 7.2: Particular of the coarse and fine grids at the leading edge

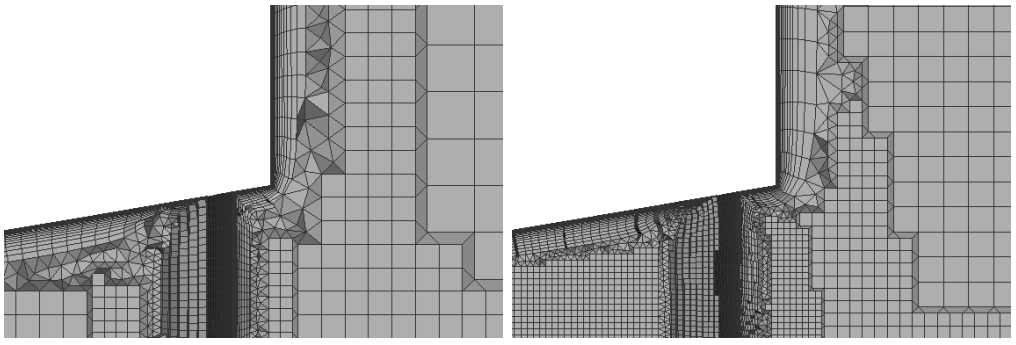

(a) coarse (b) fine

Figure 7.3: Particular of the coarse and fine grids in the meridional channel

Table 7.3: Static pressure head predicted by means of the DX-LES model and fine grid

| | Design | Off design |
|---|---|---|
| Pump performance | 1.75 m | 2.40 m |
| CFD prediction | 1.87 m | 2.29 m |

Table 7.4: Computational cost of simulations at off design condition with the three grids. Each compute node contains two 18-cores Intel Xeon E5-2697 v4 (Broadwell) at 2.30 GHz

| Grid | Number of cores | Computational time [days] |
|---|---|---|
| Coarse | 72 | 14 |
| Medium | 72 | 18 |
| Fine | 108 | 23 |

is computed for 3 and 6 revolutions for the design and off design condition respectively, after an initial period of 4 and 6 revolutions that allows to have a statistically stable flow.

The second order `backward` scheme is used for the time-integration. The second-order `Gauss linearUpwind` discretization scheme is applied to the divergence of the velocity, while a mixed second-order unbounded is applied to the turbulent quantities. The Laplacian terms are evaluated using a linear second-order bounded central scheme, while the central differencing `Gauss linear` method approximates the gradient term.

## 7.3 Results

In the following, the results of the DX-LES model are discussed in detail and compared with the literature. First the time-averaged velocity field is analysed, the grid independence study is presented and the flow physical behavior is examined. Then turbulent statistics are shown. In Tab. 7.3 the predicted static pressure head (fine grid) is displayed for both the working conditions. In Tab. 7.4 informations about the computational cost of the simulations are summarized. All the simulations have been run on 36-core compute nodes, each with two 18-cores Intel Xeon E5-2697 v4 (Broadwell) at 2.30 GHz.

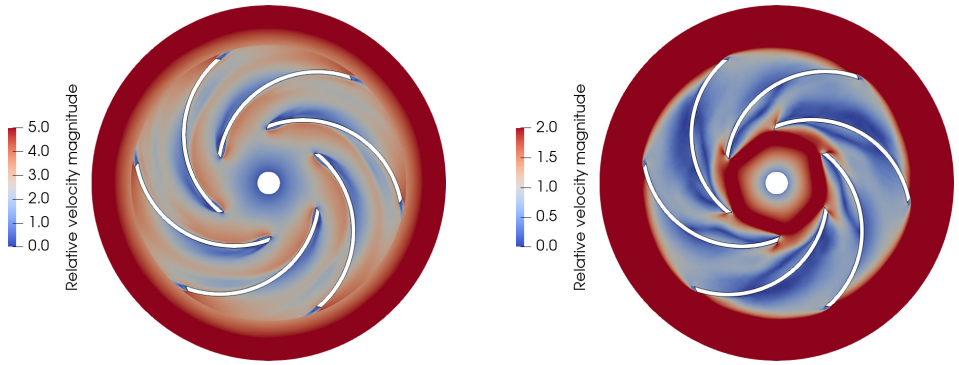


Figure 7.4: Time-averaged relative velocity field at design (left) and off design (right) conditions, grid coarse

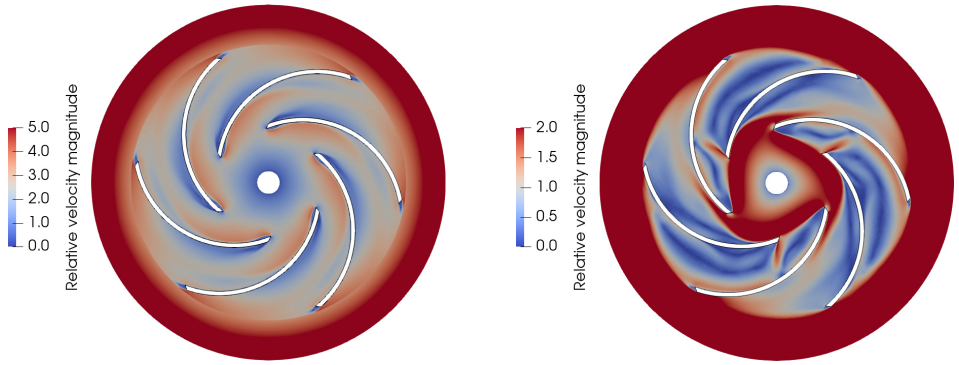


Figure 7.5: Time-averaged relative velocity field at design (left) and off design (right) conditions, grid medium

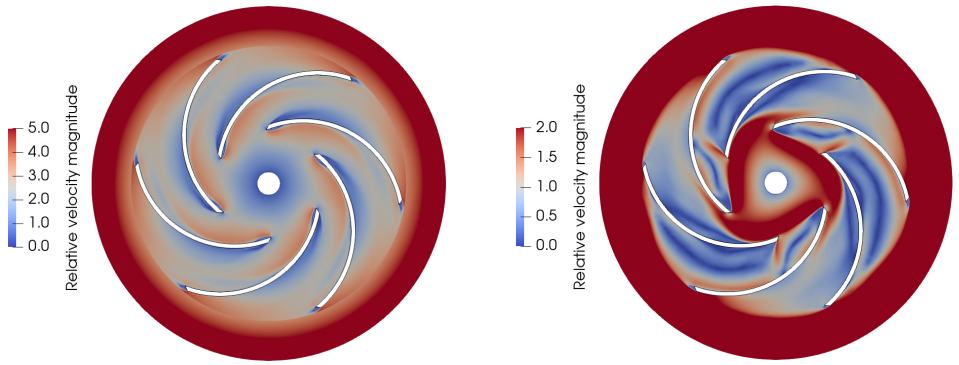


Figure 7.6: Time-averaged relative velocity field at design (left) and off design (right) conditions, grid fine

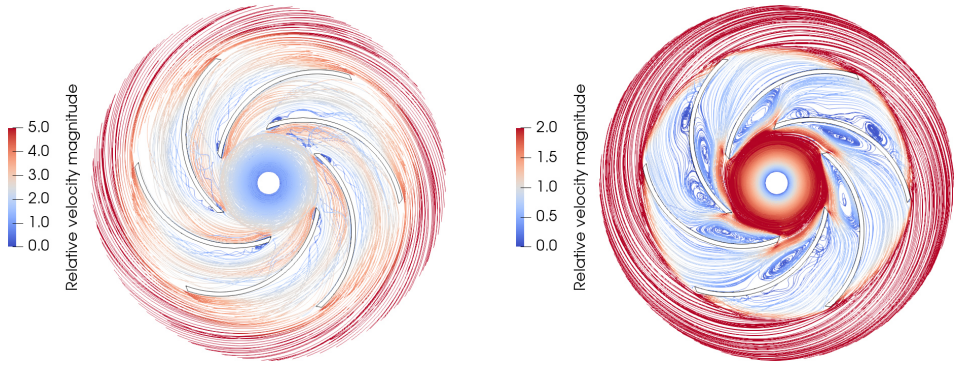


Figure 7.7: Streamlines of the time-averaged relative velocity at design (left) and off design (right) conditions, grid coarse

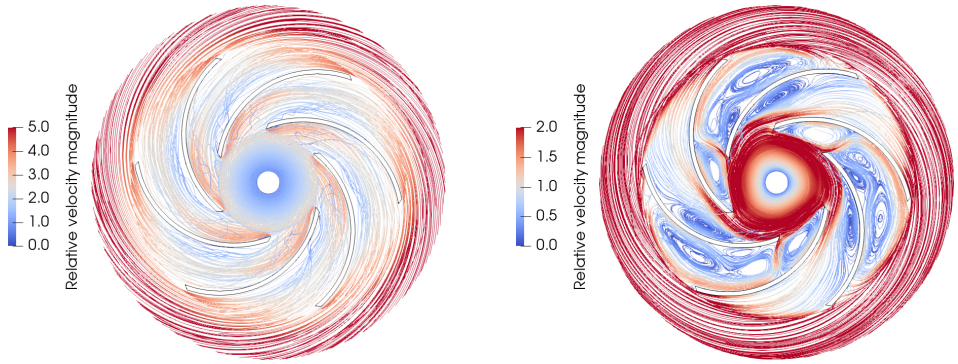


Figure 7.8: Streamlines of the time-averaged relative velocity at design (left) and off design (right) conditions, grid medium

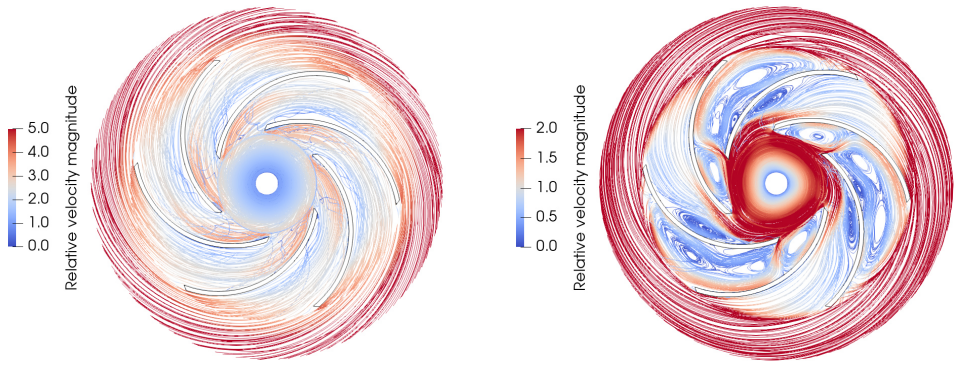


Figure 7.9: Streamlines of the time-averaged relative velocity at design (left) and off design (right) conditions, grid fine

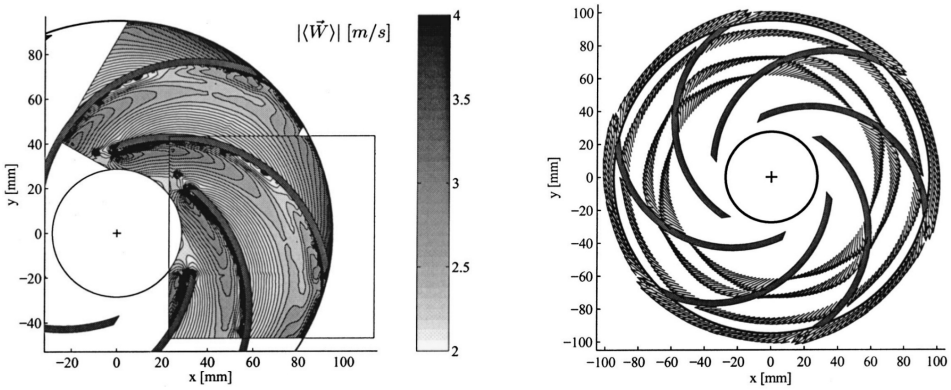


Figure 7.10: Time-averaged relative velocity at $z/z_2 = 0.5$ and design condition: contour from PIV (left) and vector plot at $R/R_2 = \{0.65, 0.75, 0.90, 1.01\}$ from LDV measurements [21] (right)

### 7.3.1 Design condition

No relevant separations take place at design load and the flow field is the same in all the blade passages. Figure 7.6 shows the time-averaged velocity field for the fine grid in the rotational reference frame. At the entrance the flow is skewed towards the suction side due to the dominant effect of the blade curvature. Along the suction side of the blade a low velocity zone is evident. It corresponds to the development phase of a jet-wake structure. At the impeller outlet the unloading of the blade occurs and the flow is more uniform. The flow field on the coarse and the medium grid (see Figs. 7.4 and 7.5 respectively) is similar, but with a coarser grid the low velocity zone is wider and the outflow is less uniform due to the higher dissipation induced by the grid. In Fig. 7.10 the PIV measurements of Pedersen et al. [21] of the time-averaged velocity field is reported. The DX-LES model with fine grid shows a good agreement with the PIV, even if in this case the low velocity zone is less pronounced.

In Figs. 7.11 and 7.12 the time-averaged velocity profiles (the radial and tangential component respectively) at $R/R_2 = 0.5$ and 0.9 are plotted for the DX-LES model, the PIV measuraments [21] and the LES and RANS from Byskov et al. [13]. The good agreement of the DX-LES model with the PIV profiles is confirmed and the phenomena discussed above are evident: at $R/R_2 = 0.5$ (see Fig. 7.11) the velocity profile is displaced toward the suction side, while at $R/R_2 = 0.9$ the velocity rise along the pressure side due to the unloading of the blade. Moreover, the final part of the low velocity zone is visible by looking the radial velocity near the suction side. The graph shows that this phenomenon is more pronounced with the coarse gird. Comparing

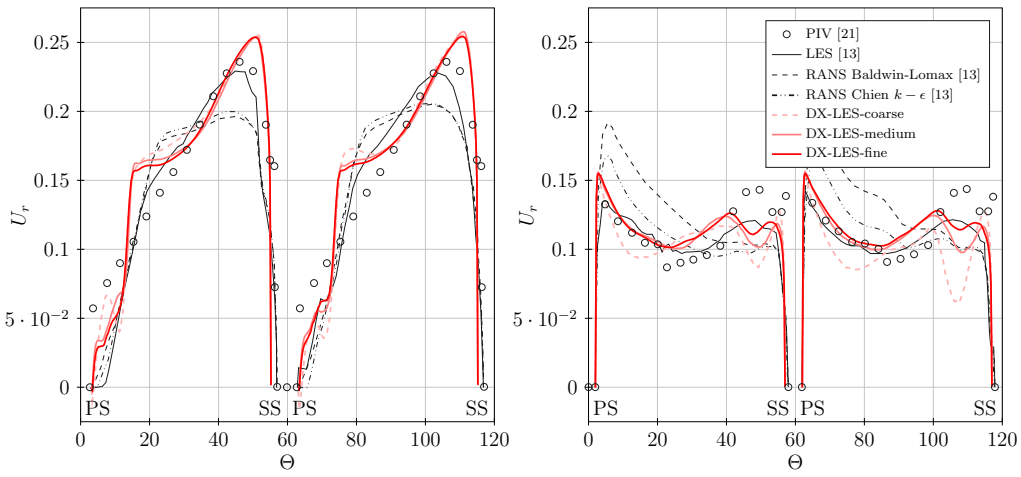


Figure 7.11: Time averaged radial velocity at $z/z_2 = 0.5$ and $R/R_2 = 0.5$ (left), $R/R_2 = 0.9$ (right) at design condition

the profiles predicted with the three grids, the convergence is assumed to be reached, observing negligible the differences between the computation with the medium and the fine grid. However, the finer mesh seems necessary to better predict the low-velocity zone.

The trend is accurately predicted also by the LES simulation of reference. Both the RANS models correctly predict the flow field, even if a flatter radial velocity profile is evident at the entrance and an overestimation of the velocity magnitude on the pressure side at the outflow is predicted.

### 7.3.2 Off design condition

Figure 7.9 shows the time-averaged velocity streamlines for the fine grid. The so called *two channel* phenomenon is well predicted by the DX-LES model. In the following, letter A refers to the unstalled passage, while letter B to the stalled one. The velocity streamlines shows that in channel A the zone of low velocity at the design condition becomes a zone of recircuilation at a quarter load condition. At the entrance the flow follows the blade curvature and the vortex starts at $R/R_2 = 0.55$, where the rotational effects are dominant with respect to the centrifugal force. At the impeller outflow the flow becomes uniform in the blade-to-blade section. The coarse and medium grids (see Figs. 7.7 and 7.8) are fine enough to be able to capture the alternation of a stalled and an unstalled passage, but the vortex in the channel A with the coarse grid is wider and starts at the leading edge.

At the entrance of the channel B (fine grid), instead, a vortex develops

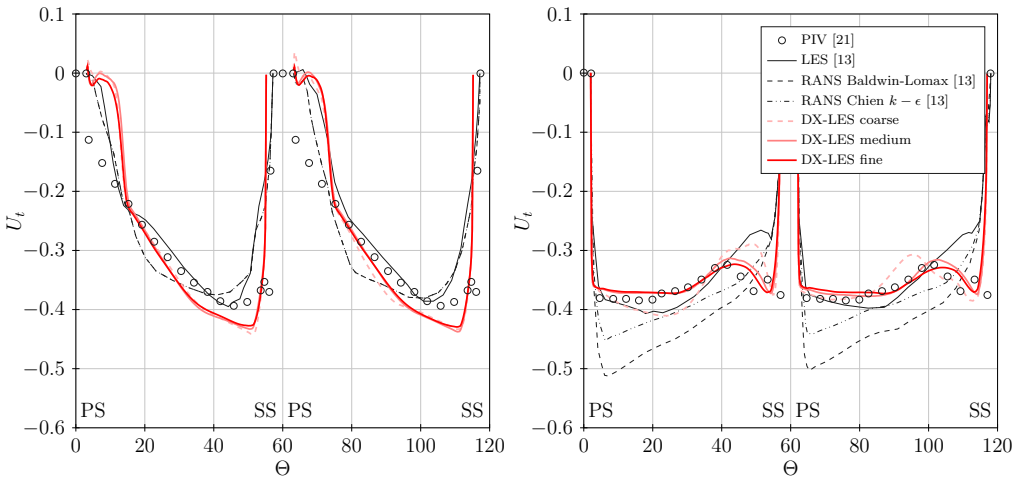


Figure 7.12: Time averaged tangential velocity at $z/z_2 = 0.5$ and $R/R_2 = 0.5$ (left), $R/R_2 = 0.9$ (right) at design condition

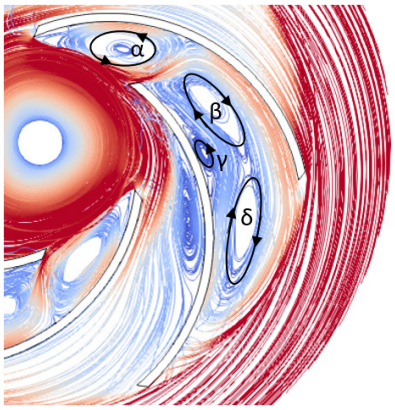


Figure 7.13: Scheme of the recirculation zones in channel B, fine grid

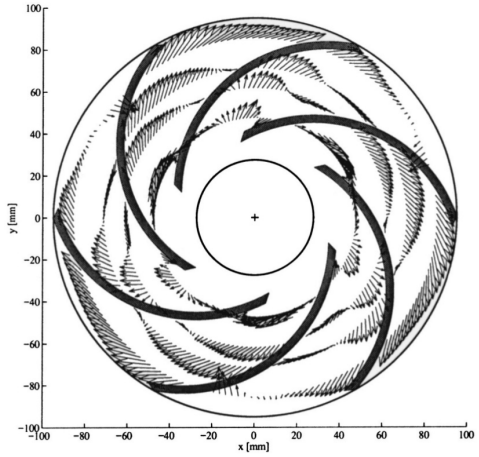


Figure 7.14: Vector plot of at Time-averaged relative velocity at $z/z_2 = 0.5$, off design condition and $R/R_2 = \{0.5, 0.65, 0.75, 0.90\}$, from LDV measurements [21]

along the suction side until $R/R_2 = 0.7$ and blocks the flow, consequently unblocking the channel A. The stall is stationary. Along the pressure side and across the major part of the channel there is a wide zone of recirculation, with three eddies. Figure 7.13 shows the flow-pattern of the complex turbulent phenomenon in the channel B. The rotational sense of the vortex $\beta$ is opposite compared to the vortex $\alpha$. Therefore, the flow that passes through the channel enters from the pressure side, but it flows along the suction side. The sense of rotation of $\delta$ is in accordance with $\beta$ and induces reverse flow at the impeller outflow. On the coarse grid the block in channel B is less evident: the recirculation zone in the channel A is wider, due to the higher dissipation of the grid; as a consequence, a bigger flow rate passes through the channel B and the vortex at the entrance is smaller and the eddies along the pressure side are limited.

Figure 7.14 shows the flow field measured with LDV [21]. In channel B only two vortexes are present: the stall at the entrance of the passages and one vortex in the central and outer part of the channel along the pressure side. Huang et al. presented an analysis in [125] of the flow field with two different LES models: the dynamic Smagorinsky model (DSM) and the dynamic cubic non-linear model (DCNM). Only the latter was able to reproduce the two vortex structure found in the experiment. The DSM predicted an additional recirculation zone, which occupy the whole passages, similarly to the DX-LES model. This can be caused by a better capability of the DCNM in predicting the rotation effect. DX-LES model gives satisfactory results, showing a behaviour comparable to the DSM and predicting the stall

phenomenon and the reverse flow at the outflow.

In Figs. 7.15 and 7.16 the time-averaged velocity profiles (the radial and tangential component respectively) at $R/R_2 = 0.5$ and 0.9 are plotted for the DX-LES model, the PIV measuraments [21] and the LES and RANS from Byskov et al. [13]. The graphs confirm that the DX-LES model is able to predict the main turbulent phenomena in the impeller. Moreover, the velocity profiles are comparable with LES results. However, some differences appear with the PIV profiles. First, at $R/R_2 = 0.5$ in channel A the DX-LES and the LES of Byskov predict a velocity profile skewed towards the pressure side, while the PIV profile is skewed toward the suction side. This discrepancy can be ascribed to the different prerotation at the inflow which causes a different swirl between the experiment and simulations. On the coarse grid a wider and anticipate recirculation zone is predicted with respect to the fine grid and the LES, along the suction side. As seen before, at the outlet the radial velocity becomes more uniform and the DX-LES model is very accurate. In channel B, it is evident from radial and tangential velocity as the DX-LES, according with the LES, predicts a greater vortex at $R/R_2 = 0.5$ along the pressure side. Notice that the sign of the tangential velocity is opposite between DX-LES and LES. At the suction side instead, both the value and the position of the peak of negative radial velocity are accurately predicted. Similarly the reverse flow at $R/R_2 = 0.9$ is well reproduced by the DX-LES model.

Also in this case the grid independence always shows an asymptotic convergence of the results for the fine mesh. In the following, only the results with the fine grid are reported.

It is noteworthy as the RANS models cannot predict the complex *two channel* phenomenon. Both the model employed by Byskov reveal identical and not-separated velocity profiles at the entrance of the two channels and a single zone of recirculation is reported at the outflow.

In Figs. 7.17 and 7.18 the time-averaged velocity profiles are plotted for the DX-LES model, the PIV measuraments and two different LES models: the localized dynamic Smagorinsky model used by Byskov et al. [13] seen above and the dynamic mixed non-linear model tested by Zhou et al. [126]. The DX-LES model shows comparable behaviour with the LES and a high accuracy.

### 7.3.3 Turbulence statistics

An analysis of the turbulent quantities is finally presented. In Fig. 7.19 the time-averaged turbulent kinetic energy $k$ at $z/z_2 = 0.5$ is shown. High values of $k$ suggest a propensity of the flow to become unstable. At design

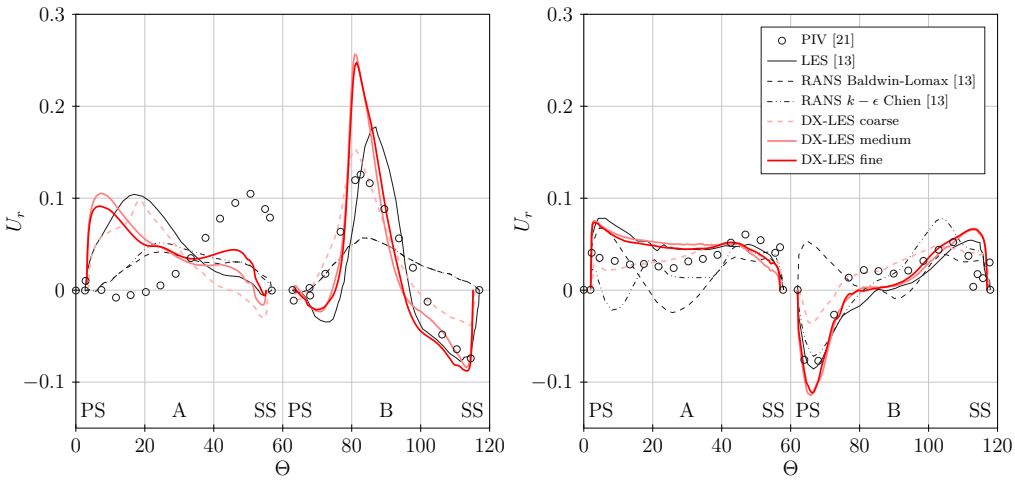


Figure 7.15: Time averaged radial velocity at $z/z_2 = 0.5$ and $R/R_2 = 0.5$ (left), $R/R_2 = 0.9$ (right) at off design condition

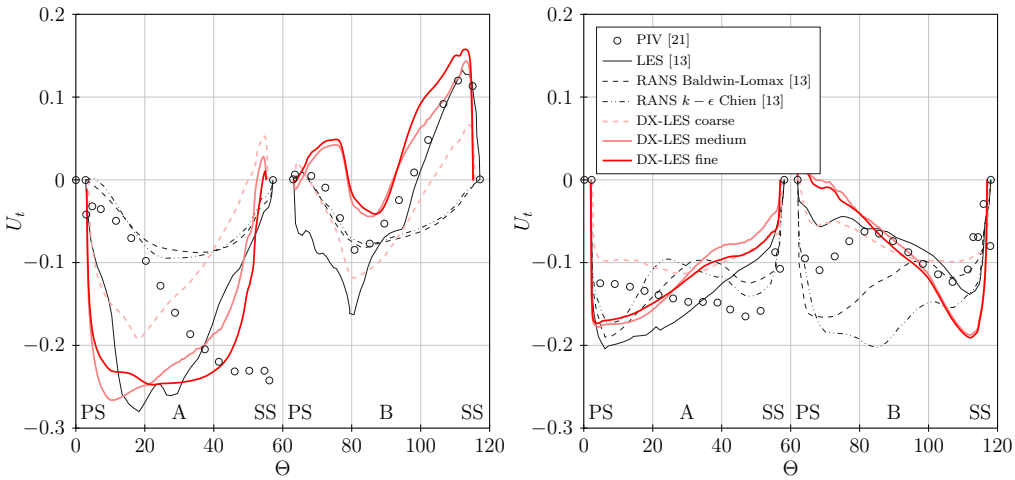


Figure 7.16: Time averaged tangential velocity at $z/z_2 = 0.5$ and $R/R_2 = 0.5$ (left), $R/R_2 = 0.9$ (right) at off design condition

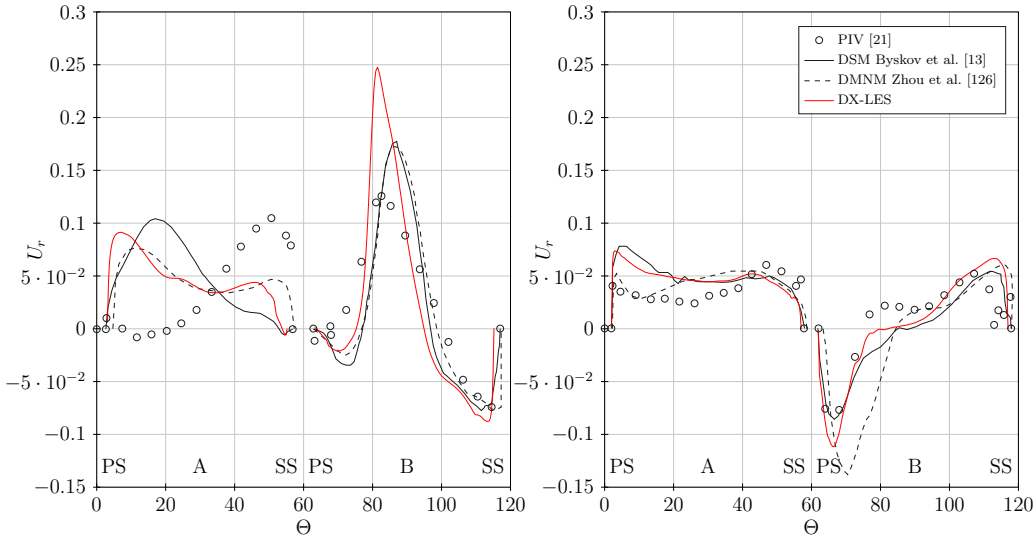


Figure 7.17: Time averaged radial velocity at $z/z_2 = 0.5$ and $R/R_2 = 0.5$ (left), $R/R_2 = 0.9$ (right) at off design condition

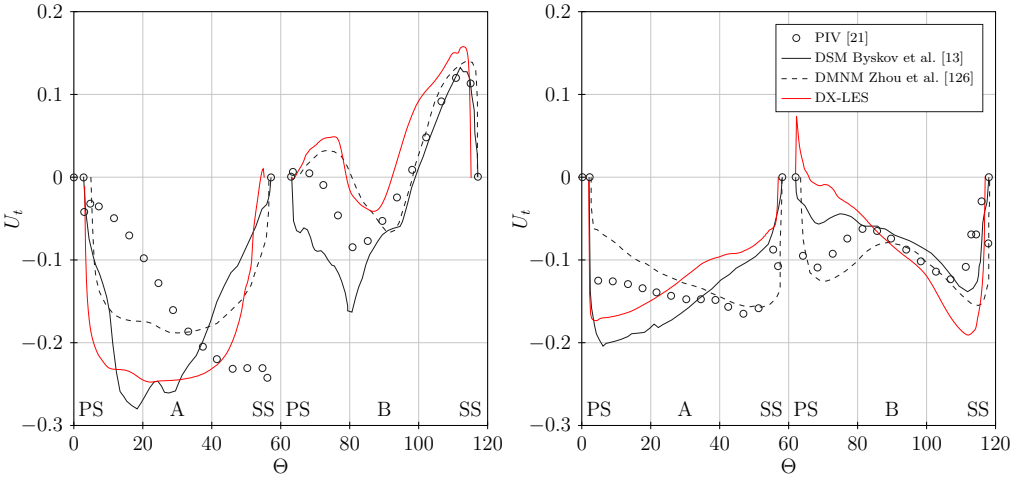


Figure 7.18: Time averaged tangential velocity at $z/z_2 = 0.5$ and $R/R_2 = 0.5$ (left), $R/R_2 = 0.9$ (right) at off design condition

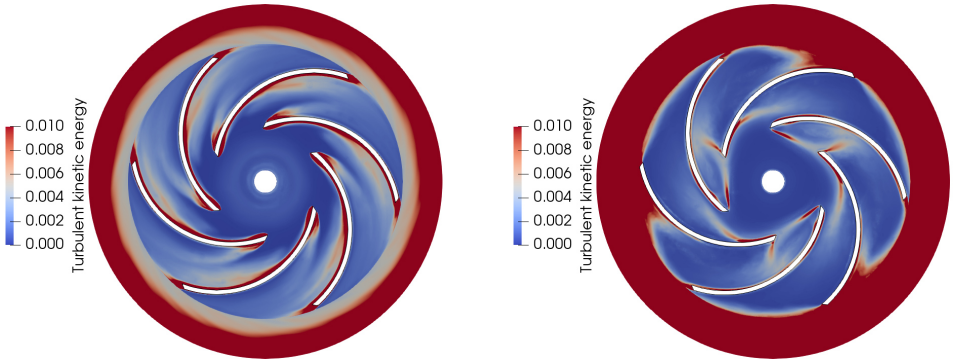


Figure 7.19: Time-averaged turbulent kinetic energy at design (left) and off design condition (right), grid fine

condition an enhance of the turbulent kinetic energy is visible at the leading edge pressure side, along the blade suction side and in correspondence of the low velocity zone. The middle part of the passage, the entrance and the outflow are characterized, instead, by low values of turbulence, which indicate a stable zone. At off design condition the stall is denoted by an increase of the turbulent kinetic energy. In particular, high values of $k$ across all the blade-to-blade section reflect the block at the entrance of the channel B. Also the flow deviation in channel A due to the recuirculation zone is characterized by high turbulent kinetic energy, as well as the reverse flow at the outflow of channel B.

Figure 7.20 shows the time-averaged vorticity at $z/z_2 = 0.5$. It is clear as higher values characterize the off design condition with respect to the design condition. In particular the stall in channel B corresponds to an increase of the vorticity, while the rest of the passage, although the wide recirculation zone, has a lower vorticity, also with respect to the channel A. This is due to the low energy of the flow downstream the stall.

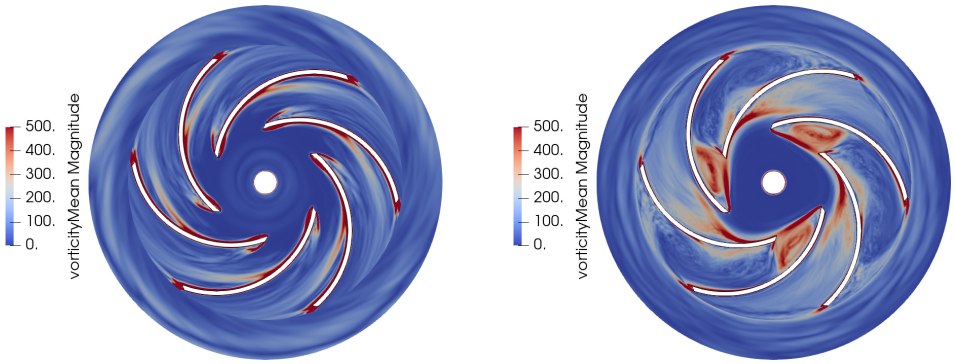


Figure 7.20: Time-averaged vorticity at design (left) and off design condition (right), grid fine

# Conclusions

In the first part of this thesis an advanced optimization technique to design impeller and diffuser blades and maximize the efficiency of the pump is presented. The study is complemented by an assessment of the robustness for the optimal design under uncertainty.

The deterministic optimization is carried out through two different surrogate-based optimization strategies in order to maximize the efficiency, while keeping constant, with a tolerance, the total pressure coefficient. The two strategies are a Surrogate-Based Optimization with Single Objective Genetic Algorithm (SOGA) and the Efficient Global Optimization (EGO). The former has given the best result, improving the efficiency of about 3% with respect to the baseline, while the EGO has provided an improvement of about 2.5%.

Then, an uncertainty quantification study is performed to compare the robustness of the optimal design with respect to the baseline. The focus is on the uncertainties of the boundary conditions associated with the experimental tests and inlet turbulent quantities for the CFD simulations. A polynomial chaos expansion is employed to assess the influence on the efficiency and the total pressure coefficient. The SOGA-based optimum has a higher efficiency but is less robust with respect to the EGO-based optimum. The latter allows enhancing the performances, while retaining the same level of variance of the baseline.

The findings of the optimization study can be summarized as follows:

- the presented strategy provides good results in the automated design of a centrifugal pump, improving the baseline design.
- the EGO scouts a larger space than the SOGA, but the SOGA performs better for this optimization problem, returning a design with a better performance in a lower number of CFD evaluations.
- the deterministic optimization enhances the performance by retaining a good level of robustness. In fact, the observed level of variability with respect to the considered uncertainties is quite low for both the

optimization strategies. In this case the robust optimization seems to be needed only if the level of variance is judged too high and a specific engineering constraint should be respected.

Future studies will include other potential sources of uncertainties, such as geometric tolerances, and if necessary, a subsequent robust optimization. Moreover, a sensitivity analysis to deepen the influence of each design variable on the performance would be helpful to understand if all the 18 variables are necessary in the parametrization.

After having provided an optimization tool for the design of a centrifugal pump, the second part of this thesis is dedicated to the implementation of a hybrid RANS-LES method for the accurate performance prediction of the pump in off design conditions. In facts, centrifugal pumps work in a wide range of conditions, not only in the design or best efficient point, and they are often characterized by vortex dynamics and, in general, unsteady phenomena. The X-LES approach is revisited by substituting its standard turbulence model with SST $k-\omega$ and shielding the RANS from the DES formulation, with the function proposed by Spalart [89], to avoid the Modelled Stress Depletion (MSD) typical of DES-like hybrid models.

This new model, delayed X-LES or DX-LES, is implemented in the open-source software OpenFOAM v.1812 and is tested first on three different test-cases, commonly used to assess turbulent models: the turbulent channel flow at $\mathrm{Re}_\tau = 2\,000$, the backward facing step at $\mathrm{Re} = 28\,000$ and the circular cylinder at $\mathrm{Re} = 3\,900$ and $\mathrm{Re} = 140\,000$.

The DX-LES model is then applied to the computation on the flow through the centrifugal pump impeller of Pedersen et al. [21] and the results are compared with experimental results and LES and RANS simulations from the literature. At design condition the flow is mainly attached. At a quarter load the flow is highly distorted with a *two channel* phenomenon, consisting in an alternation of a stalled and a unstalled channel. The flow in the channel A is dominated by rotational effects and resembles the well-behaved flow, while in passage B a stationary inlet stall cell blocks the inlet section and gives rise to a relative eddy dominating the remaining parts of the passage.

The novel hybrid model

- has demonstrated to overcome the well known problem of the MSD. In this context, the delayed version of the X-LES approach allows to improve the velocity profile estimation near wall, as shown in the turbulent plane channel. The improved wall shear stress is confirmed also in the turbulent flow over a backward facing step case. In general, each test case proves that the LES region for the X-LES model gets

into the boundary layer and results in the MSD phenomenon, while the proposed delayed version allows to improve the near wall behaviour.

- shows a good trade-off between the required computational effort compared to the LES approach and the accuracy with the respect to the RANS methods, in simulating the flow field in a centrifugal pump. In the off design conditions, DX-LES predicts the complex phenomena in good agreement with experiment, while RANS models do not reproduce the stall phenomenon observed at a quarter-load.

To conclude, the new DX-LES model is suitable to be used in industry to simulate the flow field in centrifugal pump at off design conditions. Future works will be devoted to define a new shielding function, exploiting a machine learning based approach, and to assess the DX-LES model in other industrial fields, e.g. automotive.

# Acknowledgement

I would first like to express my sincere gratitude to my supervisor, Professor Antonio Ghidoni, for providing me invaluable guidance in my PhD. His expertise, support and constructive feedback have driven me in my research.

I would like to thank my whole research team for accompanying me throughout this years and, in particular, Gianmaria Noventa, for his help and advise.

I would like to thank my tutor at INIRIA Saclay Île-de-France research centre, Professor Pietro Marco Congedo, for enabling me to visit in his office and for his valuable guidance throughout my research. I also wish to acknowledge my colleagues from my period in Paris.

Finally I would like to thank the Industrie Saleri Italo S.p.A. for funding this project. I wish thank my tutor in Saleri, Dr. Remo De Donno, for his relentless assistance and the opportunity to further my research being part of his team, and my colleagues for their collaboration.

# Bibliography


[1] W. Wang, S. Yuan, J. Pei, and J. Zhang. "Optimization of the diffuser in a centrifugal pump by combining response surface method with multi-island genetic algorithm". In: *Proceedings of the Institution of Mechanical Engineers, Part E: Journal of Process Mechanical Engineering* 231 (May 2015). DOI: 10.1177/0954408915586310.

[2] S. Derakhshan, M. Pourmahdavi, E. Abdolahnejad, A. Reihani, and A. Ojaghi. "Numerical shape optimization of a centrifugal pump impeller using artificial bee colony algorithm". In: *Computers & Fluids* 81 (July 2013), pp. 145–151. DOI: 10.1016/j.compfluid.2013.04.018.

[3] Y. Xu, L. Tan, S. Cao, and W. Qu. "Multiparameter and multiobjective optimization design of centrifugal pump based on orthogonal method". In: *Proceedings of the Institution of Mechanical Engineers, Part C: Journal of Mechanical Engineering Science* 231 (July 2017), pp. 2569–2579. DOI: 10.1177/0954406216640303.

[4] S. Derakhshan and M. Bashiri. "Investigation of an efficient shape optimization procedure for centrifugal pump impeller using eagle strategy algorithm and ANN (case study: slurry flow)". In: *Structural and Multidisciplinary Optimization* 58 (Jan. 2018), pp. 1–15. DOI: 10.1007/s00158-018-1897-3.

[5] B. Ghadimi, A. Nejat, S. Nourbakhsh, and N. Naderi. "Multi Objective Genetic Algorithm Assisted by ANN Metamodel for Shape Optimization of a Centrifugal Blood Pump". In: *Artificial organs* 43 (Oct. 2018). DOI: 10.1111/aor.13366.

[6] X. Han, Y. Kang, J. Sheng, Y. Hu, and W. Zhao. "Centrifugal pump impeller and volute shape optimization via combined NUMECA, genetic algorithm, and back propagation neural network". In: *Structural and Multidisciplinary Optimization* 61 (Sept. 2019). DOI: 10.1007/s00158-019-02367-8.

[7] H.-S. Shim, K.-Y. Kim, and Y.-S. Choi. "Three-Objective Optimization of a Centrifugal Pump to Reduce Flow Recirculation and Cavitation". In: *Journal of Fluids Engineering* 140 (Sept. 2018), 091202 (14 pages). DOI: 10.1115/1.4039511.

[8] J. Pei, W. Wang, M. Osman, and X. Gan. "Multiparameter optimization for the nonlinear performance improvement of centrifugal pumps using a multilayer neural network". In: *Journal of Mechanical Science and Technology* 33 (June 2019). DOI: 10.1007/s12206-019-0516-6.

[9] A. Nourbakhsh, H. Safikhani, and S. Derakhshan. "The comparison of multi-objective particle swarm optimization and NSGA II algorithm: Applications in centrifugal pumps". In: *Engineering Optimization* 43 (Oct. 2011), pp. 1095–1113. DOI: 10.1080/0305215X.2010.542811.

[10] R. Barrio, E. Blanco, J. Parrondo, J. González, and J. Fernandez. "The Effect of Impeller Cutback on the Fluid-Dynamic Pulsations and Load at the Blade-Passing Frequency in a Centrifugal Pump". In: *Journal of Fluids Engineering-transactions of The Asme - J FLUID ENG* 130 (Nov. 2008). DOI: 10.1115/1.2969273.

[11] R. Barrio, J. Parrondo, and E. Blanco. "Numerical analysis of the unsteady flow in the near-tongue region in a volute-type centrifugal pump for different operating points". In: *Computers & Fluids* 39.5 (2010), pp. 859–870. ISSN: 0045-7930. DOI: https://doi.org/10.1016/j.compfluid.2010.01.001.

[12] O. Braun. "Part load flow in radial centrifugal pumps". In: (Jan. 2009). DOI: 10.5075/epfl-thesis-4422.

[13] R. K. Byskov, C. B. Jacobsen, and N. Pedersen. "Flow in a Centrifugal Pump Impeller at Design and Off-Design Conditions—Part II: Large Eddy Simulations ". In: *Journal of Fluids Engineering* 125.1 (Jan. 2003), pp. 73–83. DOI: 10.1115/1.1524586. URL: https://doi.org/10.1115/1.1524586.

[14] W. Wang and Y. Wang. "Analysis of inner flow in low specific speed centrifugal pump based on LES". In: *Journal of Mechanical Science and Technology* 27 (June 2013). DOI: 10.1007/s12206-013-0408-0.

[15] C. Kato, H. Mukai, and A. Manabe. "Large-Eddy Simulation of Unsteady Flow in a Mixed-Flow Pump". In: *International Journal of Rotating Machinery* 9 (Sept. 2003). DOI: 10.1155/S1023621X03000320.

[16] A. Posa, A. Lippolis, and E. Balaras. "Large-Eddy Simulation of a Mixed-Flow Pump at Off-Design Conditions". In: *Journal of Fluids Engineering* 137 (Oct. 2015). DOI: 10.1115/1.4030489.

[17] A. Posa, A. Lippolis, and E. Balaras. "Investigation of Separation Phenomena in a Radial Pump at Reduced Flow Rate by Large-Eddy Simulation". In: *Journal of Fluids Engineering* 138 (June 2016). DOI: 10.1115/1.4033843.

[18] J. Feng, F.-K. Benra, and H. Dohmen. "Unsteady Flow Visualization at Part-Load Conditions of a Radial Diffuser Pump: by PIV and CFD". In: *Journal of Visualization* 12 (Mar. 2009), pp. 65–72. DOI: 10.1007/BF03181944.

[19] A. Lucius and G. Brenner. "Unsteady CFD simulations of a pump in part load conditions using scale-adaptive simulation". In: *International Journal of Heat and Fluid Flow* 31 (Dec. 2010), pp. 1113–1118. DOI: 10.1016/j.ijheatfluidflow.2010.06.005.

[20] A. Lucius and G. Brenner. "Numerical Simulation and Evaluation of Velocity Fluctuations During Rotating Stall of a Centrifugal Pump". In: *Journal of Fluids Engineering* 133 (Aug. 2011), p. 081102. DOI: 10.1115/1.4004636.

[21] N. Pedersen, P. S. Larsen, and C. B. Jacobsen. "Flow in a Centrifugal Pump Impeller at Design and Off-Design Conditions—Part I: Particle Image Velocimetry (PIV) and Laser Doppler Velocimetry (LDV) Measurements ". In: *Journal of Fluids Engineering* 125.1 (Jan. 2003), pp. 61–72. ISSN: 0098-2202. DOI: 10.1115/1.1524585. URL: https://doi.org/10.1115/1.1524585.

[22] A. Zhao, P. Wu, D. Z. Wu, and L. Q. Wang. "The optimization of a low specific speed pipeline pump". In: *IOP Conference Series: Materials Science and Engineering* 52.3 (Dec. 2013), p. 032002. DOI: 10.1088/1757-899x/52/3/032002.

[23] S. Li, P. Wu, and D. Wu. "Hydraulic Optimization and Loss Analyses of a Low Specific-Speed Centrifugal Pump With Variable-Thickness Blades". In: July 2016. DOI: 10.1115/FEDSM2016-7814.

[24] W. Li. "NPSHr optimization of axial-flow pumps". In: *Journal of Fluids Engineering-transactions of The Asme - J FLUID ENG* 130 (July 2008). DOI: 10.1115/1.2948368.

[25] J.-H. Kim, H.-C. Lee, J.-H. KIM, S. Kim, J.-Y. Yoon, and Y.-S. Choi. "Design Techniques to Improve the Performance of a Centrifugal Pump using CFD". In: *Journal of Mechanical Science and Technology* 29 (Jan. 2015), pp. 215–225. DOI: 10.1007/s12206-014-1228-6.

[26] S. Burguburu, C. Toussaint, C. Bonhomme, and G. Leroy. "Numerical Optimization of Turbomachinery Bladings". In: *Journal of Turbomachinery-transactions of The Asme - J TURBOMACH-T ASME* 126 (Jan. 2004). DOI: 10.1115/1.1645869.

[27] A. Oyama, M. Liou, and S. Obayashi. "Transonic Axial-Flow Blade Optimization: Evolutionary Algorithms/Three-Dimensional Navier-Stokes Solver". In: *Journal of Propulsion and Power - J PROPUL POWER* 20 (July 2004), pp. 612–619. DOI: 10.2514/1.2290.

[28] J. Pei, W. Wang, and S. Yuan. "Multi-point optimization on meridional shape of a centrifugal pump impeller for performance improvement". In: *Journal of Mechanical Science and Technology* 30 (Nov. 2016), pp. 4949–4960. DOI: 10.1007/s12206-016-1015-7.

[29] W. Wang, J. Pei, S. Yuan, J. Zhang, J. Yuan, and C. Xu. "Application of different surrogate models on the optimization of centrifugal pump". In: *Journal of Mechanical Science and Technology* 30 (Feb. 2016), pp. 567–574. DOI: 10.1007/s12206-016-0110-0.

[30] M. H. Siddique, M. K R, and A. Samad. "Optimization of a Centrifugal Pump Impeller by Controlling Blade Profile Parameters". In: June 2016. DOI: 10.1115/GT2016-56604.

[31] R. De Donno, A. Ghidoni, G. Noventa, and S. Rebay. "Shape optimization of the ERCOFTAC centrifugal pump impeller using open-source software". In: *Optimization and Engineering* 20 (Mar. 2019). DOI: 10.1007/s11081-019-09428-3.

[32] A. Zhao, Z. Lai, P. Wu, C. Linlin, and D. Wu. "Multi-objective optimization of a low specific speed centrifugal pump using an evolutionary algorithm". In: *Engineering Optimization* 48 (Nov. 2015), pp. 1–24. DOI: 10.1080/0305215X.2015.1104987.

[33] D. Wang and L. He. "Adjoint Aerodynamic Design Optimization for Blades in Multi-Stage Turbomachines: Part I—Methodology and Verification". In: *Journal of Turbomachinery-transactions of The Asme - J TURBOMACH-T ASME* 132 (Apr. 2010). DOI: 10.1115/1.3072498.

[34] M. Pini, G. Persico, D. Pasquale, and S. Rebay. "Adjoint Method for Shape Optimization in Real-Gas Flow Applications". In: *Journal of Engineering for Gas Turbines and Power* 137 (Oct. 2014), p. 032604. DOI: 10.1115/1.4028495.

[35] R. Van den Braembussche. *Optimization of Radial Impeller Geometry.* AD-a476 514. Von Karman Inst for Fluid Dynamics Rhode-Saint-Genese (Belgium), 2006.

[36] D. Pasquale, A. Ghidoni, and S. Rebay. "Shape Optimization of an Organic Rankine Cycle Radial Turbine Nozzle". In: *Journal of Engineering for Gas Turbines and Power* 135 (Apr. 2013), p. 042308. DOI: 10.1115/1.4023118.

[37] Z. Guo, L. Song, Z. Zhou, J. Li, and Z. Feng. "Multi-Objective Aerodynamic Optimization Design and Data Mining of a High Pressure Ratio Centrifugal Impeller". In: *Journal of Engineering for Gas Turbines and Power* 137 (Sept. 2015), p. 092602. DOI: 10.1115/1.4029882.

[38] T. Verstraete, Z. Alsalihi, and R. Braembussche. "Multidisciplinary Optimization of a Radial Compressor for Micro Gas Turbine Applications". In: *Journal of Turbomachinery-transactions of The Asme - J TURBOMACH-T ASME* 132 (July 2010). DOI: 10.1115/1.3144162.

[39] M. Olivero, D. Pasquale, A. Ghidoni, and S. Rebay. "Three-dimensional turbulent optimization of vaned diffusers for centrifugal compressors based on metamodel-assisted genetic algorithms". In: *Optimization and Engineering* 15 (Dec. 2013), pp. 973–992. DOI: 10.1007/s11081-013-9242-6.

[40] U. Schroeders, O. Wilhelm, and G. Olaru. "Meta-Heuristics in Short Scale Construction: Ant Colony Optimization and Genetic Algorithm". In: *PLOS ONE* 11 (Nov. 2016), e0167110. DOI: 10.1371/journal.pone.0167110.

[41] F. Bre, J. Gimenez, and V. Fachinotti. "Prediction of wind pressure coefficients on building surfaces using Artificial Neural Networks". In: *Energy and Buildings* 158 (Nov. 2017). DOI: 10.1016/j.enbuild.2017.11.045.

[42] R. Jin and T. Simpson. "Comparative Studies Of Metamodeling Techniques Under Multiple Modeling Criteria". In: *8th Symposium on Multidisciplinary Analysis and Optimization* (Aug. 2000). DOI: 10.2514/6.2000-4801.

[43] S. A. I. Bellary, R. Adhav, M. H. Siddique, B. H. Chon, F. Kenyery, and A. Samad. "Application of computational fluid dynamics and surrogate-coupled evolutionary computing to enhance centrifugal-pump performance". In: *Engineering Applications of Computational Fluid Mechanics* 10 (Jan. 2016), pp. 172–182. DOI: 10.1080/19942060.2015.1128359.

[44] A. Samad, K.-Y. Kim, T. Goel, R. Haftka, and W. Shyy. "Multiple Surrogate Modeling for Axial Compressor Blade Shape Optimization". In: *Journal of Propulsion and Power* 24 (Mar. 2008), pp. 302–310. DOI: 10.2514/1.28999.

[45] M. Mckay, R. Beckman, and W. Conover. "A Comparison of Three Methods for Selecting Vales of Input Variables in the Analysis of Output From a Computer Code". In: *Technometrics* 21 (May 1979), pp. 239–245. DOI: 10.1080/00401706.1979.10489755.

[46] M. Kaufman, V. Balabanov, A. Giunta, B. Grossman, W. Mason, S. Burgee, R. Haftka, and L. Watson. "Variable-complexity response surface approximations for wing structural weight in HSCT design". In: *Computational Mechanics* 18 (Mar. 1996), pp. 112–126. DOI: 10.1007/BF00350530.

[47] J. Combès. "Test case U3: Centrifugal pump with a vaned diffuser". In: *ERCOFTAC Seminar and Workshop on Turbomachinery Flow Prediction VII* (1999).

[48] M. Ubaldi, P. Zunino, G. Barigozzi, and A. Cattanei. "An Experimental Investigation of Stator Induced Unsteadiness on Centrifugal Impeller Outflow". In: *Journal of Turbomachinery* 118 (Jan. 1996). DOI: 10.1115/94-GT-005.

[49] O. Petit and H. Nilsson. "Numerical Investigations of Unsteady Flow in a Centrifugal Pump with a Vaned Diffuser". In: *International Journal of Rotating Machinery* 2013 (July 2013). DOI: 10.1155/2013/961580.

[50] L. Piegl and W. Tiller. *The NURBS Book*. Berlin, Heidelberg: Springer-Verlag, 1995. ISBN: 3540550690.

[51] *Scilab*. 5.5.2. http://www.scilab.org.

[52] N. P. Salunke, J. A. R. A., and S. Channiwala. "Airfoil Parameterization Techniques: A Review". In: *American Journal of Mechanical Engineering* 2.4 (2014), pp. 99–102. DOI: 10.12691/ajme-2-4-1.

[53] A. Stepanoff. *Centrifugal and Axial Flow Pumps: Theory, Design, and Application*. Krieger Publishing Company, 1993. ISBN: 9780894647239.

[54] A. Ghidoni, E. Pelizzari, S. Rebay, and V. Selmin. "3D anisotropic unstructured grid generation". In: *International Journal for Numerical Methods in Fluids* 51 (July 2006), pp. 1097–1115. DOI: 10.1002/fld.1151.

[55] *foam-extend*. 4.1. https://sourceforge.net/projects/foam-extend/.

[56] F. Menter. "Zonal Two Equation k-w Turbulence Models For Aerodynamic Flows". In: *AIAA Paper* 1993 (Feb. 1993). DOI: 10.2514/6.1993-2906.

[57] O. Petit, M. PAGE, M. Beaudoin, and H. Nilsson. "The ERCOFTAC centrifugal pump OpenFOAM case-study". In: *3rd IAHR International Meeting of the Workgroup on Cavitation and Dynamic Problems in Hydraulic Machinery and Systems* (Jan. 2009).

[58] R. De Donno, S. Rebay, and A. Ghidoni. "Surrogate-Based Shape Optimization of the ERCOFTAC Centrifugal Pump Impeller". In: Sept. 2019, pp. 227–246. DOI: 10.1007/978-3-319-89890-2_15.

[59] M. Eldred and D. Dunlavy. "Formulations for Surrogate-Based Optimization with Data Fit Multifidelity and Reduced-Order Models". In: (Sept. 2006). In: 11th AIAA/ISSMO Multidisciplinary Analysis and Optimization Conference. DOI: 10.2514/6.2006-7117.

[60] D. Jones, M. Schonlau, and W. Welch. "Efficient Global Optimization of Expensive Black-Box Functions". In: *Journal of Global Optimization* 13 (Dec. 1998), pp. 455–492. DOI: 10.1023/A:1008306431147.

[61] *Dakota*. 6.8. https://dakota.sandia.gov/.

[62] S. Brown, L. Swiler, M. Eldred, E. Cyr, A. Giunta, and M. Richards. "The Surfpack Software Library for Surrogate Modeling of Sparse Irregularly Spaced Multidimensional Data". In: 3 (Sept. 2006). In: 11th AIAA/ISSMO Multidisciplinary Analysis and Optimization Conference. DOI: 10.2514/6.2006-7049.

[63] Z. Li and X. Zheng. "Review of design optimization methods for turbomachinery aerodynamics". In: *Progress in Aerospace Sciences* 93 (July 2017). DOI: 10.1016/j.paerosci.2017.05.003.

[64] Y. Nomaguchi, K. Kawakami, K. Fujita, Y. Kishita, K. Hara, and M. Uwasu. "Robust Design of System of Systems Using Uncertainty Assessment Based on Lattice Point Approach: Case Study of Distributed Generation System Design in a Japanese Dormitory Town". In: *International Journal of Automation Technology* 10 (Sept. 2016), pp. 678–689. DOI: 10.20965/ijat.2016.p0678.

[65] H.-G. Beyer and B. Sendhoff. "Robust optimization – A comprehensive survey". In: *Computer Methods in Applied Mechanics and Engineering* 196.33 (2007), pp. 3190–3218. ISSN: 0045-7825. DOI: https://doi.org/10.1016/j.cma.2007.03.003.

[66] B. L. Gorissen, İ. Yanıkoğlu, and D. den Hertog. "A practical guide to robust optimization". In: *Omega* 53 (2015), pp. 124–137. ISSN: 0305-0483. DOI: https://doi.org/10.1016/j.omega.2014.12.006.

[67] S. Salehi, M. Raisee Dehkordi, M. Cervantes, and A. Nourbakhsh. "On the flow field and performance of a centrifugal pump under operational and geometrical uncertainties". In: *Applied Mathematical Modelling* 61 (May 2018). DOI: 10.1016/j.apm.2018.05.008.

[68] S. Wiener. "The Homogeneous Chaos". In: *J. Comput. Phys.* 224 (Jan. 1938), pp. 560–586. DOI: 10.2307/2371268.

[69] R. Askey and J. Wilson. "Some Basic Hypergeometric Orthogonal Polynomials that Generalize Jacobi Polynomials". In: *Memoirs of the American Mathematical Society* 319 (Jan. 1985). DOI: 10.1090/memo/0319.

[70] D. S.-K. Ting. "Chapter 4 - Turbulence Scales". In: *Basics of Engineering Turbulence*. Ed. by D. S.-K. Ting. Academic Press, 2016, pp. 69–98. ISBN: 978-0-12-803970-0. DOI: https://doi.org/10.1016/B978-0-12-803970-0.00004-0. URL: http://www.sciencedirect.com/science/article/pii/B9780128039700000040.

[71] B. Geurts. *Elements of Direct and Large-eddy Simulation*. R.T. Edwards, 2004. ISBN: 9781930217072.

[72] B. Chaouat. "The State of the Art of Hybrid RANS/LES Modeling for the Simulation of Turbulent Flows". In: *Flow, Turbulence and Combustion* 99.2 (Sept. 2017), pp. 279–327. URL: https://doi.org/10.1007/s10494-017-9828-8.

[73] L. Tay-Wo-Chong. "Numerical Simulation of the Dynamics of Turbulent Swirling Flames". PhD thesis. Jan. 2012.

[74] S. B. Pope. *Turbulent Flows*. Cambridge University Press, 2000. DOI: 10.1017/CBO9780511840531.

[75] D. Chapman. "Computational Aerodynamics Development and Outlook". In: vol. 17. 12. Dec. 1979.

[76] L. Temmerman, M. Hadžiabdić, M. Leschziner, and K. Hanjalić. "A hybrid two-layer URANS–LES approach for large eddy simulation at high Reynolds numbers". In: *International Journal of Heat and Fluid Flow* 26.2 (2005), pp. 173–190. ISSN: 0142-727X. DOI: https://doi.org/10.1016/j.ijheatfluidflow.2004.07.006.

[77] "Hybrid LES/RANS methods for the simulation of turbulent flows". In: *Progress in Aerospace Sciences* 44.5 (2008), pp. 349–377. ISSN: 0376-0421. DOI: https://doi.org/10.1016/j.paerosci.2008.05.001.

[78] K. Hanjalić, M. Hadžiabdić, L. Temmerman, and M. Leschziner. *Merging LES and RANS Strategies: Zonal or Seamless Coupling?* Ed. by R. Friedrich, B. J. Geurts, and O. Métais. Dordrecht: Springer Netherlands, 2004, pp. 451–464. ISBN: 978-1-4020-2313-2.

[79] P. Spalart, W.-H. Jou, M. Strelets, and S. Allmaras. "Comments on the feasibility of LES for wings, and on a hybrid RANS/LES approach". In: *Advances in DNS/LES. Proceeding of First AFOSR International Conference on DNS/LES, 4-8 August*. Ed. by C. Liu and Z. Liu. Greyden Press, 1997, pp. 137–147.

[80] S. Spalart Allmaras. "A one-equation turbulence model for aerodynamic flows". In: *AIAA Journal* (Jan. 1992). 30th Aerospace Sciences Meeting and Exhibit.

[81] P. Spalart Allmaras. "A one-equation turbulence model for aerodynamic flows". In: *La Recherche Aérospatiale* 1 (1994).

[82] M. Strelets. "Detached eddy simulation of massively separated flows". In: *39th Aerospace Sciences Meeting and Exhibit*. 2001. DOI: 10.2514/6.2001-879. URL: https://arc.aiaa.org/doi/abs/10.2514/6.2001-879.

[83] F. Menter. "Two-equation eddy-viscosity turbulence models for engineering application". In: *AIAA Paper* 32.8 (Aug. 1994).

[84] F. Menter and T. Esch. "Elements of industrial heat transfer predictions $16^{th}$ Brazilian Congress of Mechanical Engineering". In: (2001). 16th Brazilian Congress of Mechanical Engineering.

[85] F. Menter, M. Kuntz, and R. Langtry. "Ten years of industrial experience with the SST turbulence model". In: *Heat and Mass Transfer* 4 (Jan. 2003).

[86] *The Menter Shear Stress Transport Turbulence Model*. https://turbmodels.larc.nasa.gov/sst.html.

[87] J. Kok, H. Dol, B. Oskam, and H. van der Ven. "Extra-Large Eddy Simulation of Massively Separated Flows". In: *42nd AIAA Aerospace Sciences Meeting and Exhibit*. 2004. DOI: 10.2514/6.2004-264. URL: https://arc.aiaa.org/doi/abs/10.2514/6.2004-264.

[88] J. C. Kok. "Resolving the Dependence on Freestream Values for the k- Turbulence Model". In: *AIAA Journal* 38.7 (2000), pp. 1292–1295. DOI: 10.2514/2.1101.

[89] P. R. Spalart, S. Deck, M. L. Shur, K. D. Squires, M. K. Strelets, and A. Travin. "A New Version of Detached-eddy Simulation, Resistant to Ambiguous Grid Densities". In: *Theoret. Comput. Fluid Dynamics* 20.181 (2006), pp. 181–195. DOI: https://doi.org/10.1007/s00162-006-0015-0.

[90] J. Kok. "A Stochastic Backscatter Model for Grey-Area Mitigation in Detached Eddy Simulations". In: *Flow, Turbulence and Combustion* 99 (July 2017), pp. 119–150. DOI: 10.1007/s10494-017-9809-y.

[91] M. Gritskevich, A. Garbaruk, J. Schütze, and F. Menter. "Development of DDES and IDDES Formulations for the $k-\omega$ Shear Stress Transport Model". In: *Flow, Turbulence and Combustion* 88 (Apr. 2012). DOI: 10.1007/s10494-011-9378-4.

[92] L. Zhou, R. Zhao, and W. Yuan. "An investigation of interface conditions inherent in detached-eddy simulation methods". In: *Aerospace Science and Technology* 74 (Mar. 2018), pp. 46–55. DOI: 10.1016/j.ast.2018.01.005.

[93] K. Reddy, J. Ryon, and P. Durbin. "A DDES model with a Smagorinsky-type eddy viscosity formulation and log-layer mismatch correction". In: *International Journal of Heat and Fluid Flow* 50 (June 2014). DOI: 10.1016/j.ijheatfluidflow.2014.06.002.

[94] M. Breuer, N. Jovičić, and K. Mazaev. "Comparison of DES, RANS and LES for the separated flow around a flat plate at high incidence". In: *International Journal for Numerical Methods in Fluids* 41 (Jan. 2003), pp. 357–388. DOI: 10.1002/fld.445.

[95] *OpenFOAM*. v1812. https://www.openfoam.com/.

[96] S. Hoyas and J. Jiménez. "Scaling of the velocity fluctuations in turbulent channels up to Re = 2003". In: *Physics of Fluids - PHYS FLUIDS* 18 (Jan. 2006). DOI: 10.1063/1.2162185.

[97] S. Hoyas and J. Sendín. "Reynolds number effects on the Reynolds-stress budgets in turbulent channels". In: *Physics of Fluids* 20 (Oct. 2008). DOI: 10.1063/1.3005862.

[98] J. C. Vogel and J. K. Eaton. "Combined Heat Transfer and Fluid Dynamic Measurements Downstream of a Backward-Facing Step". In: *Journal of Heat Transfer* 107.4 (Nov. 1985), pp. 922–929. ISSN: 0022-1481. DOI: 10.1115/1.3247522. URL: https://doi.org/10.1115/1.3247522.

[99] C. Norberg. "FLOW AROUND A CIRCULAR CYLINDER: ASPECTS OF FLUCTUATING LIFT". In: *Journal of Fluids and Structures* 15.3 (2001), pp. 459–469.

[100] J. S. Son and T. J. Hanratty. "Velocity gradients at the wall for flow around a cylinder at Reynolds numbers from 5 × 103 to 105". In: *Journal of Fluid Mechanics* 35.2 (1969), pp. 353–368. DOI: 10.1017/S0022112069001157.

[101] L. Ong and J. Wallace. "The velocity field of the turbulent very near wake of a circular cylinder". In: *Experiments in Fluids* 20.6 (Apr. 1996), pp. 441–453. DOI: 10.1007/BF00189383. URL: https://doi.org/10.1007/BF00189383.

[102] L. Lourenco and C. Shih. "Characteristics of the plane turbulent near wake of a circular cylinder". In: *A particle image velocimetry study* (1993).

[103] A. G. Kravchenko and P. Moin. "Numerical studies of flow over a circular cylinder at ReD=3900". In: *Physics of Fluids* 12.2 (2000), pp. 403–417. DOI: 10.1063/1.870318. URL: https://doi.org/10.1063/1.870318.

[104] J. Wissink and W. Rodi. "Numerical study of the near wake of a circular cylinder". In: *International Journal of Heat and Fluid Flow* 29 (Aug. 2008), pp. 1060–1070. DOI: 10.1016/j.ijheatfluidflow.2008.04.001.

[105] P. Parnaudeau, J. Carlier, D. Heitz, and E. Lamballais. "Experimental and numerical studies of the flow over a circular cylinder at Reynolds number 3900". In: *Physics of Fluids* 20.8 (2008), p. 085101. DOI: 10.1063/1.2957018. eprint: https://doi.org/10.1063/1.2957018. URL: https://doi.org/10.1063/1.2957018.

[106] D. A. Lysenko, I. S. Ertesvåg, and K. E. Rian. "Large-Eddy Simulation of the Flow Over a Circular Cylinder at Reynolds Number 3900 Using the OpenFOAM Toolbox". In: *Flow, Turbulence and Combustion* 89.4 (Dec. 2012), pp. 491–518. ISSN: 1573-1987. DOI: 10.1007/s10494-012-9405-0. URL: https://doi.org/10.1007/s10494-012-9405-0.

[107] X. Ma, G.-S. Karamanos, and G. Karniadakis. "Dynamics and Low-Dimensionality of a Turbulent Near Wake". In: *Journal of Fluid Mechanics* 410 (May 2000), pp. 29–65. DOI: 10.1017/S0022112099007934.

[108] M. Breuer. "Large eddy simulation of the subcritical flow past a circular cylinder: numerical and modeling aspects". In: *International Journal for Numerical Methods in Fluids* 28.9 (1998), pp. 1281–1302.

[109] D. C. Wilcox. *Turbulence modelling for CFD*. DCW Industries, La Cañada, 2006.

[110] M. Shur, P. R. Spalart, M. K. Strelets, and A. Travin. "Navier-Stokes simulation of shedding turbulent flow past a circular cylinder and a cylinder with backward splitter plate". In: Third EC-COMAS CFD Conference, Paris. Sept. 1996.

[111] W. Shih, C. Wang, D. Coles, and A. Roshko. "Experiments on flow past rough circular cylinders at large Reynolds numbers". In: *Journal of Wind Engineering and Industrial Aerodynamics* 49.1 (1993), pp. 351–368. ISSN: 0167-6105. DOI: https://doi.org/10.1016/0167-6105(93)90030-R.

[112] E. Achenbach. "Achenbach, E.: Distribution of Local Pressure and Skin Friction around a Circular Cylinder in Cross-Flow up to Re = 5×106. Journal of Fluid Mechanics 34(4), 625-639". In: *Journal of Fluid Mechanics* 34 (Dec. 1968), pp. 625–639. DOI: 10.1017/S0022112068002120.

[113] B. Cantwell and D. Coles. "An Experimental Study on Entrainment and Transport in the Turbulent Near Wake of a Circular Cylinder". In: *Journal of Fluid Mechanics* 136 (Dec. 1983). DOI: 10.1017/S0022112083002189.

[114] J. Fröhlich, W. Rodi, P. Kessler, S. Parpais, J. P. Bertoglio, and D. Laurence. "Large Eddy Simulation of Flow around Circular Cylinders on Structured and Unstructured Grids". In: *Numerical Flow Simulation I: CNRS-DFG Collaborative Research Programme, Results 1996–1998*. Ed. by E. H. Hirschel. Berlin, Heidelberg: Springer Berlin Heidelberg, 1998, pp. 319–338. DOI: 10.1007/978-3-540-44437-4_16. URL: https://doi.org/10.1007/978-3-540-44437-4_16.

[115] J. Fröhlich, W. Rodi, J.-P. Bertoglio, U. Bieder, and H. Touil. "Large Eddy Simulation of Flow around Circular Cylinders on Structured and Unstructured Grids, II". In: *Notes on Numerical Fluid Mechanics* (Jan. 2001). DOI: 10.1007/978-3-663-10916-7_16.

[116] S. Karabelas. "Large Eddy Simulation of high-Reynolds number flow past a rotating cylinder". In: *International Journal of Heat and Fluid Flow* 31 (Aug. 2010), pp. 518–527. DOI: 10.1016/j.ijheatfluidflow.2010.02.010.

[117] M. Shur, P. Spalart, M. Strelets, and A. Travin. "Detached-eddy simulation of an airfoil at high angle of attack". In: *Engineering Turbulence Modelling and Experiments 4*. Ed. by W. Rodi and D. Laurence. Oxford: Elsevier Science Ltd, 1999, pp. 669–678. ISBN: 978-0-08-043328-8. DOI: https://doi.org/10.1016/B978-008043328-8/50064-3.

[118] A. Islam and B. Thornber. "A high-order hybrid turbulence model with implicit large-eddy simulation". In: *Computers & Fluids* 167 (2018), pp. 292–312. ISSN: 0045-7930. DOI: https://doi.org/10.1016/j.compfluid.2018.03.031.

[119] W. Zheng, C. Yan, H. Liu, and D. Luo. "Comparative assessment of SAS and DES turbulence modeling for massively separated flows". In: *Acta Mechanica Sinica* 32 (Sept. 2015). DOI: 10.1007/s10409-015-0505-7.

[120] J. G. Eggels. "Direct and large-eddy simulation of turbulent fluid flow using the lattice-Boltzmann scheme". In: *International Journal of Heat and Fluid Flow* 17.3 (1996), pp. 307–323. ISSN: 0142-727X. DOI: https://doi.org/10.1016/0142-727X(96)00044-6.

[121] J. Revstedt, L. Fuchs, and C. Trägårdh. "Large eddy simulations of turbulent flow in a stirred reactor". English. In: *Chemical Engineering Science* 53.24 (1998), pp. 4041–4053. ISSN: 0009-2509. DOI: 10.1016/S0009-2509(98)00203-6.

[122] C. C. S. Song, X. Chen, T. Ikohagi, J. Sato, K. Shinmei, and K. Tani. "Simulation of Flow Through Francis Turbine by Les Method". In: *Hydraulic Machinery and Cavitation*. Ed. by E. Cabrera, V. Espert, and F. Martínez. Dordrecht: Springer Netherlands, 1996, pp. 267–276. ISBN: 978-94-010-9385-9.

[123] C.-M. Jang, M. Furukawa, and M. Inoue. "Analysis of Vortical Flow Field in a Propeller Fan by LDV Measurements and LES—Part I: Three-Dimensional Vortical Flow Structures". In: *Journal of Fluids Engineering-transactions of The Asme - J FLUID ENG* 123 (Dec. 2001). DOI: 10.1115/1.1412565.

[124] Z. Yang, F. Wang, and P. Zhou. "Evaluation of Subgrid-scale Models in Large-eddy Simulations of Turbulent Flow in a Centrifugal Pump Impeller". In: *Chinese Journal of Mechanical Engineering* 25 (Sept. 2012). DOI: 10.3901/CJME.2012.05.911.

[125] H. Xianbei, Z.-q. Liu, Y.-j. Li, W. Yang, and Q. Guo. "Study on the internal characteristics of stall in a centrifugal pump by a cubic nonlinear SGS model". In: *Journal of Hydrodynamics* 31 (Dec. 2018). DOI: 10.1007/s42241-018-0170-y.

[126] P.-j. Zhou, F.-j. Wang, Z.-j. Yang, and J.-g. Mou. "Investigation of rotating stall for a centrifugal pump impeller using various SGS models". In: *Journal of Hydrodynamics, Ser. B* 29 (Apr. 2017), pp. 235–242. DOI: 10.1016/S1001-6058(16)60733-3.

*Grazie a mamma e papà, a Luca e Diego, a Gianmaria, a Nawal e Laura*